Experimental Investigation of Boiling Heat Transfer Under an Impinging Water Jet

Experimental Investigation of Boiling Heat Transfer Under an Impinging Water Jet

By

Mahmoud A. A. Abdelfattah, B.Sc., M.Sc.

A Thesis

Submitted to the School of Graduate Studies

in Partial Fulfillment of the Requirements for

the Degree Doctor of Philosophy

McMaster University

DOCTOR OF PHILOSOPHY (2022) McMaster University
(Mechanical Engineering) Hamilton, Ontario, Canada

TITLE: Experimental Investigation of Boiling Heat Transfer Under an Impinging Water Jet

AUTHOR: Mahmoud A. A. Abdelfattah
B.Sc., M.Sc. Mechanical Engineering (Cairo University)

SUPERVISOR: Dr. Mohamed S. Hamed

NUMBER OF PAGES: ix, 129

Abstract

Jet impingement cooling has been used widely in many practical applications due to its high heat flux capability. Jet impingement cooling can be operated in different heat transfer modes, according to the application, such as single-phase forced convection, nucleate boiling, and transition boiling. Developing effective and accurate mechanistic models for nucleate and transition boiling is very challenging, especially in jet impingement boiling (JIB). The knowledge of mechanisms associated with jet impingement boiling heat transfer, especially in the transition boiling regime is lacking due to the limited research work that has been carried out in this area.

The current study is an experimental and analytical investigation of JIB within the nucleate and transition boiling regimes. This study focuses on studying JIB within the stagnation zone of a free water jet. An experimental setup has been designed and built at the Thermal Processing Laboratory (TPL) with the capability of carrying out boiling experiments at heat fluxes up to 12 MW/m^2. The JIB curves have been obtained under steady-state conditions for a wide range of jet conditions, higher than those considered during previous JIB studies. The effect of jet velocity, up to 3.8 m/s, and degree of subcooling, up to 49 °C, on the JIB curve has been studied. The results showed that both jet velocity and degree of subcooling have a weak effect on the nucleate boiling regime and significantly affect the transition boiling regime. Bubble dynamics under the impinging jet within the nucleate boiling regime and the stability of the vapor layer within the transition boiling regime have been investigated.

The work carried out on the nucleate boiling regime considered the effect of wall superheat, liquid subcooling, and jet velocity on the bubble departure diameter (BDD). The BDD was captured using high-speed imaging. Experiments have been conducted on the isolated bubble boiling regime covering the range of liquid degree of subcooling from 11.7 °C to 37.6 °C, wall degree of superheat from 12.6 °C to 33.7 °C, and jet velocity from 0.2 m/s to 0.8 m/s. Results showed that the BDD increased proportionally with wall superheat and inversely with the degree of subcooling. The effect of jet velocity on BDD was found noticeable only at relatively high degrees of subcooling. An empirical correlation has been developed to predict the BDD with a relative deviation of about 12 %. An analytical mechanistic model, based on force balance and thermal balance equations, has been developed to predict the bubble growth rate and the BDD. The developed model was validated using current experimental data. The model gave a relative deviation of 17.8 %. Results of the mechanistic model within the stagnation zone showed that, amongst the three heat transfer mechanisms that affect bubble growth (i.e., the microlayer evaporation, the heat from the superheated layer, the convection heat loss to subcooled liquid), the microlayer evaporation is the most significant contributor to the rate of bubble growth.

The current work conducted within the transition boiling regime was focused on the determination of the total wall heat flux within the stagnation zone, both experimentally and analytically. Steady-state experiments have been carried out during which the vapor layer stability was examined. The vapor layer breakup frequency was measured using a fiber-optic probe. Experiments were conducted at a jet velocity of 1 m/s and degrees of subcooling between 11 and 49 ºC. High-speed imaging was also used to capture the Rayleigh-Taylor instability within the stagnation zone. Results revealed that the measured breakup frequency fluctuated significantly. However, the change in the average frequency was consistent with the change in the wall heat flux with surface superheat. The average breakup frequency increased with the degree of subcooling, which indicated that the vapor layer instability increased with the degree of subcooling. A mechanistic model of the wall heat flux within the transition regime was developed, which predicted the current experimental data with a relative deviation within ± 20 %. Results obtained from the developed mechanistic model were in a good agreement with experimental data reported in the literature with a relative deviation within ±30 %. The captured high-speed images confirmed the existence of the Rayleigh-Taylor (RT) instability within the transition boiling regime. Repetitive cycles of surface wetting and dryness with high frequency were observed. Each cycle began with the nucleation of small bubbles, then they grew and merged to form a large bubble that covered (isolated) the surface. The RT instability caused the large bubble to break up eventually, then the subcooled liquid rushed to the dried-out surface, and the cycle was repeated.

Dedication

To my beloved wife Aya and my Princesses Sara, Asma, Salma

Acknowledgment

First of all, I would like to praise the Almighty Allah without him I had no power or strength to finish this work.

I would like to express my gratitude to my supervisor Dr. Mohamed Hamed for supervising this work and for his support and encouragement during my study. Also, I would like to thank my supervisory committee members, Dr. Chan Ching and Dr. James Cotton for the valuable discussion and suggestions.

I gratefully thank the technicians at the mechanical engineering department at McMaster University: John Colenbrander, Mark MacKenzie, Michael Lee, and Justin Bernar for their help to build the experimental setup.

Last but not least, I would like to express my deepest gratitude to my family for their continuous support and prayers. Special thanks to my wife for her never-ending love and support during my study.

List of Symbols and Abbreviations

Nomenclature

ɑ	acceleration	(m/s^2)
A	Area	(m^2)
BO	Boiling number =ratio of heat transfer to latent heat	(-)
BDD	Bubble departure diameter	(m)
b	Correction factor	(-)
C	Empirical constant	(-)
C_p	Specific heat	(J/Kg.K)
D	Diameter	(m)
d_w	Contact diameter	(m)
F	Force	(N)
$F_{\sigma y}$	Surface tension force	(N)
F_b	Buoyancy force	(N)
F_{cp}	Contact pressure force	(N)
F_h	Hydrodynamic pressure force	(N)
F_{du}	Unsteady drag force	(N)
f	Bubble release frequency	(Hz)
g	Gravity	(m/s^2)
h	Heat transfer coefficient	($W/m^2.K$)
h_{fg}	Latent heat	(J/kg)
Ja	Jakob number	(-)
k	Thermal conductivity	(W/m.K)
N_a	Active nucleation site density	(m^{-2})
P	Pressure	(kpa)
Pr	Prandtl number	(-)
q''	Heat flux	(W/m^2)

R	Radius	(m)
Re	Reynolds number	(-)
t	Time	(s)
T	Temperature	(K)
V	Velocity	(m/s)

Greek symbol

α	Thermal diffusivity	(m^2/s)
γ	Contact angle	(Degree)
δ	Boundary layer thickness	(m)
η_o	Interface disturbance amplitude	(m)
λ	wavelength	(m)
μ	Dynamic viscosity	(Pa.s)
ν	Kinematic viscosity	(m^2/s)
ρ	Density	(Kg/m^3)
σ	Surface tension	(N/m)
χ	Subcooled factor	(-)
ω	Growth rate	(Hz)

Subscripts

c	Convection
d	Most dangerous
ev	Evaporative
h	Heater
i	Intrusion
l	Liquid
q	Quenching
s	Surface
sat	Saturation
sub	Subcooling
sup	Superheat
sys	System

v	Vapor
w	Wall/ waiting
x	X-direction
y	Y-direction
1p	One phase
2p	Two-phase

Table of Contents

List of Figures

List of Tables

1. Chapter 1: Introduction

1.1. Background

Two-phase heat transfer is considered the most efficient means of heat transfer that has been used widely in many practical applications. Its applications span from home appliances to space rockets. Figure 1.1 shows various types of boiling. Jet impingement boiling (JIB) is associated with significantly high rates of heat transfer as such, it has been implemented in various technological applications (e.g., cooling of electronic devices, heat treatment processes, and emergency cooling of nuclear reactors, etc.).

The boiling curve under an imping jet depends on the jet flow field (i.e., the stagnation and the parallel flow zones), as depicted in Figure 1.2. The boiling curve in both zones starts with a single-phase forced convection regime (FC) in which the heat flux changes with the surface temperature linearly. By increasing the surface temperature, the incipience of isolated bubbles occurs which represents the onset of the nucleate boiling regime (NB). As the surface temperature increases, more nucleation sites become active, and the isolated bubbles coalesce with the neighbors. The merged bubbles form large bubbles that isolate the surface and lead to burnout or the critical heat flux (CHF). The CHF marks the end of the NB regime and the beginning of the transition boiling regime (TB) in which unstable vapor blanket forms and collapses on the heated surface. At very high temperatures, the heat flux decreases to the Leidenfrost point, which demarcates the end

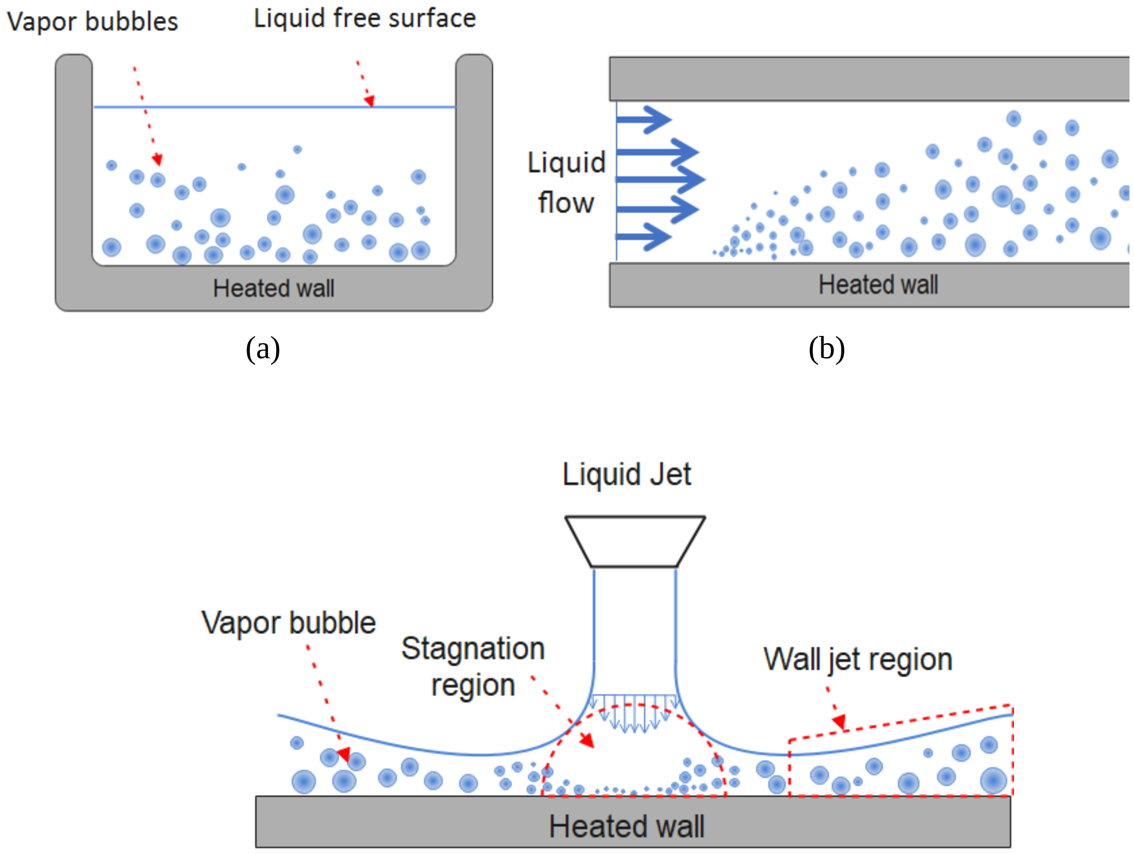

(a)

(b)

(c)

Figure 1.1: Types of boiling heat transfer: (a) Pool boiling; (b) Flow boiling; (c) Jet impingement boiling.

of the transition boiling and the beginning of the film boiling (FB) regime. In the latter, the vapor layer becomes stable and reduces the surface wettability, resulting in a decrease in heat transfer rate. The boiling curve in the stagnation zone is different than that in the parallel flow zone. It is associated with a high heat transfer rate over a wide range of surface temperatures, known as the "shoulder heat flux" region.

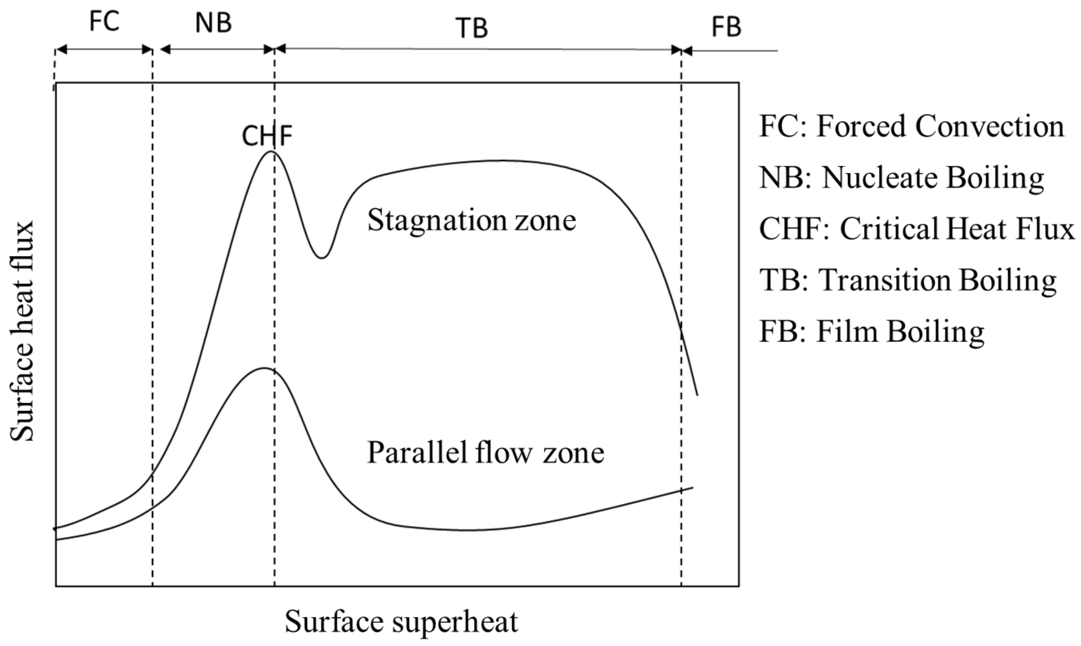

Figure 1.2: Boiling curve under an impinging jet.

Although JIB has been implemented in many applications, a mechanistic model based on the underlying physics has not been fully developed yet. The majority of the research carried out on JIB has focused on developing global models in which case the mechanisms of heat transfer at the surface are not properly captured. The following literature review covers the works that focused on the entire JIB curve under steady-state conditions, bubble dynamics within the nucleate boiling regime, and vapor layer instability within the transition boiling regime.

1.2. Literature Review

Two types of experiments are commonly carried out to investigate JIB: transient and steady-state experiments. Transient JIB experiments involve heating the boiling surface to a high starting temperature then the surface is subjected to the impinging liquid jet. Steady-state experiments are carried out by keeping the surface temperature of the boiling surface constant while the surface is subjected to the impinging jet. Wolf et al. [1] reviewed the research works carried out on JIB till 1993. Their review included different jet configurations, different boiling regimes, and the effect of system parameters, i.e., jet velocity, liquid subcooling, fluid properties, surface orientation, and jet-to-surface distance. Moreover, these studies investigated the general effect of these parameters on the boiling curve during transient experiments and steady-state experiments until the CHF. Yet the underlying physics have not been addressed. Qiu et al. [2] summarized the developments of JIB for the later two decades. Yet, the review paper focused on the nucleate boiling regime and critical heat flux during steady-state experiments.

There are extensive experimental studies on JIB under transient conditions [3]. During transient experiments, one can obtain information about the cooling rate and the boiling curve. However, it is challenging to acquire the details of the complicated JIB phenomenon necessary to understand the physics of the various heat transfer mechanisms associated with JIB due to the fast boiling process and the short period of time. During steady-state experiments, one can obtain details such as bubble growth rate, bubble departure diameter, bubble departure frequency, and active nucleation sites. In this case, the entire boiling curve can be studied under certain experimental conditions to capture and properly investigate the underlying physics. Because of the difficulty associated with carrying out steady-state JIB experiments, a limited number of studies investigated the entire JIB curve experimentally under steady-state conditions.

1.2.1. Steady-State Experiments of JIB

Miyasaka et al. [4] conducted steady-state experiments to investigate the effect of high subcooling (85 °C) and jet velocities (1.5, 3.5, and 15.3 m/s) on boiling heat transfer at the stagnation zone under an upward water jet impinging on a horizontal heated surface. The results revealed that the heat flux in the nucleate boiling regime was not affected by the jet velocity and fluid temperature. Furthermore, after the boiling curve reached its critical value (CHF), it exhibited a first transition mode in which the heat flux increased gradually with increasing surface temperature. Then it reached almost a plateau (shoulder heat flux) which extended over a wide range of surface temperatures, as shown in Figure 1.3.

Tokokai et al. [5] carried out steady-state experiments using two jet configurations: a circular water jet normal to a heated surface and a planar water jet parallel to the heated surface. They considered jet velocities up to 3 m/s and water subcooling up to 30 °C. The results showed that the heat flux increased with surface temperature after the CHF. This phenomenon was attributed to what they referred to as microbubble emission boiling

(MEB) where large bubbles breakup into microbubbles that enhance the wetting of the hot surface. The MEB phenomenon is discussed in detail in section 0. Furthermore, they found that at subcooling of 20 °C, the JIB curves for both configurations reached a plateau of heat flux for a wide range of surface superheat which agreed with the findings of [4]. The CHF and MEB increased with increasing the jet velocity and degree of subcooling.

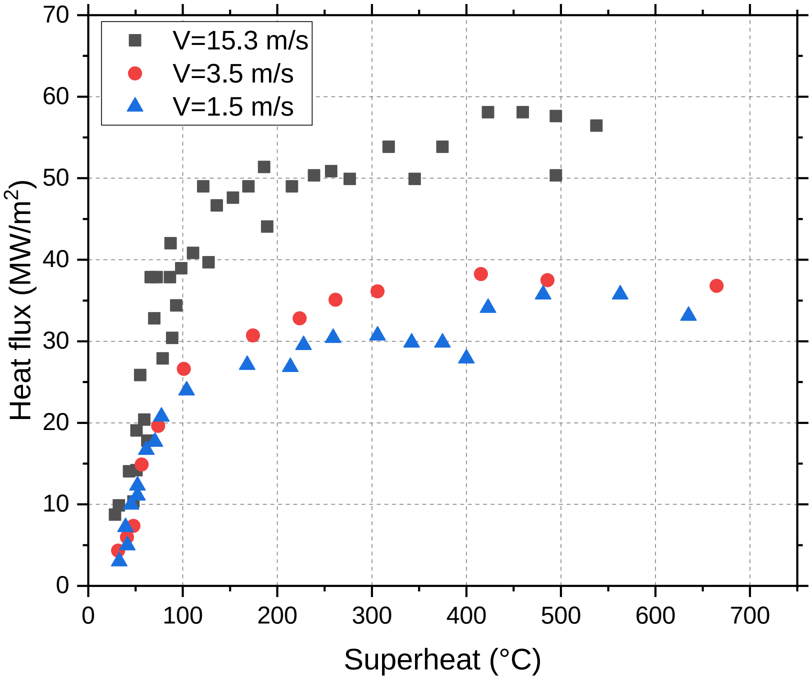

Figure 1.3: JIB curves at V_{jet} =1.5-15.3 m/s and ΔT_{sub} =85 °C obtained by Miyasaka et al[4].

Robidou et al. [6,7] performed experiments under surface temperature-controlled steady-state conditions to study the effect of jet velocity, degree of subcooling, and nozzle-to-surface distance on the boiling curve of a hot plate subjected to a planar water jet. They considered both the stagnation and the parallel flow regions. The boiling curve in the stagnation region was characterized by a shoulder heat flux region. The boiling curve within the parallel flow region at different locations downstream of the stagnation zone was similar to the classical pool boiling curve. The value of shoulder heat flux decreased with the increase in the distance from the stagnation line (x), as shown in Figure 1.4. For the studied range of jet velocity (0.7-0.8 m/s) and subcooling (7-17 °C), they found that the jet velocity and liquid subcooling did not affect the nucleate boiling heat transfer. However, the CHF, shoulder heat flux, and film boiling increased with increasing the degree of subcooling. Although increasing the jet velocity resulted in an increase in the heat transfer in the transition regime, the effect of subcooling dominated the effect of jet velocity.

On the contrary to Miyasak et al. [4], after the CHF, the boiling curve decreased within the transition regime to a first minimum then increased to the shoulder heat flux, as shown in Figure 1.5. When the subcooling increased, the boiling curve exhibited the first minimum at lower surface temperature as the MEB occurred at lower superheat when subcooling increased. They speculated that at a high degree of subcooling or high jet velocity, the MEB occurred just after the CHF which explained why the heat flux in [4] increased after the CHF.

Bogdanic et al. [8] used the same setup as used by [6] to carry out steady-state experiments using an optic fiber probe to investigate the vapor layer instability in the stagnation zone under JIB at a jet velocity of 0.4 m/s and subcooling of 20 °C. Ahmed and

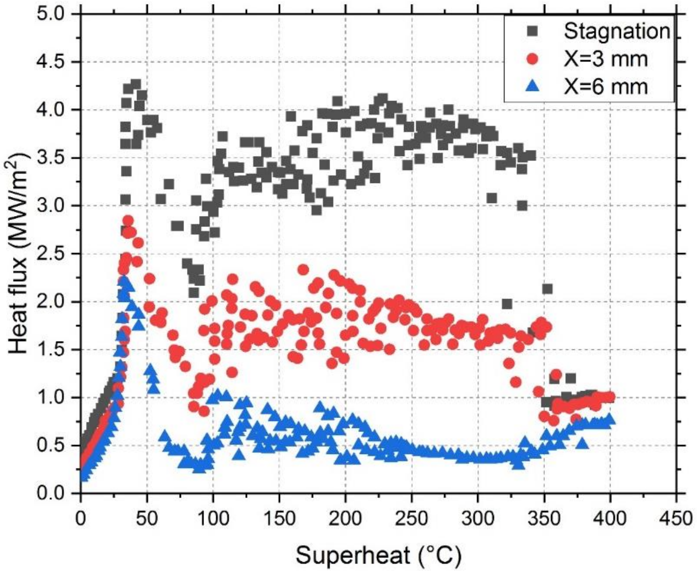

Figure 1.4: JIB curves at jet velocity of 0.8 m/s and subcooling of 16 °C[7].

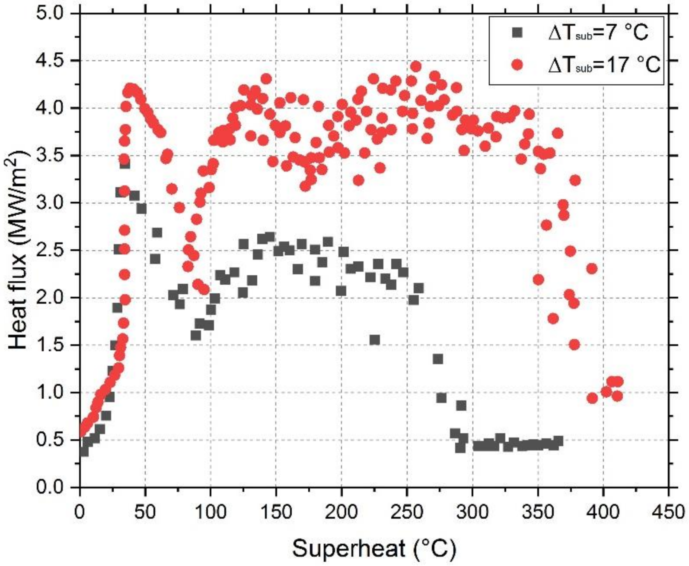

Figure 1.5: Experimental results obtained by [6] at a jet velocity of 0.7 m/s and degrees of subcooling of 7 °C and 17 °C.

Hamed [9] used high-speed imaging and fiber optic probe to study the liquid-vapor interface in the transition regime at the stagnation zone under JIB at a jet velocity of 0.6 m/s and subcooling of 15 °C. The boiling curves obtained by [8] and [9] had the same characteristics as the ones produced by Robidou et al. [6], as shown in Figure 1.6. Also, one can observe that the shoulder heat flux exceeded the CHF in the results obtained by[8] and it was lower than the CHF in [9]. The experimental conditions in previous works [6,8,9] were limited to a jet velocity of 1 m/s and a degree of subcooling of 20°C due to the limited heating capacity of the used experimental setup.

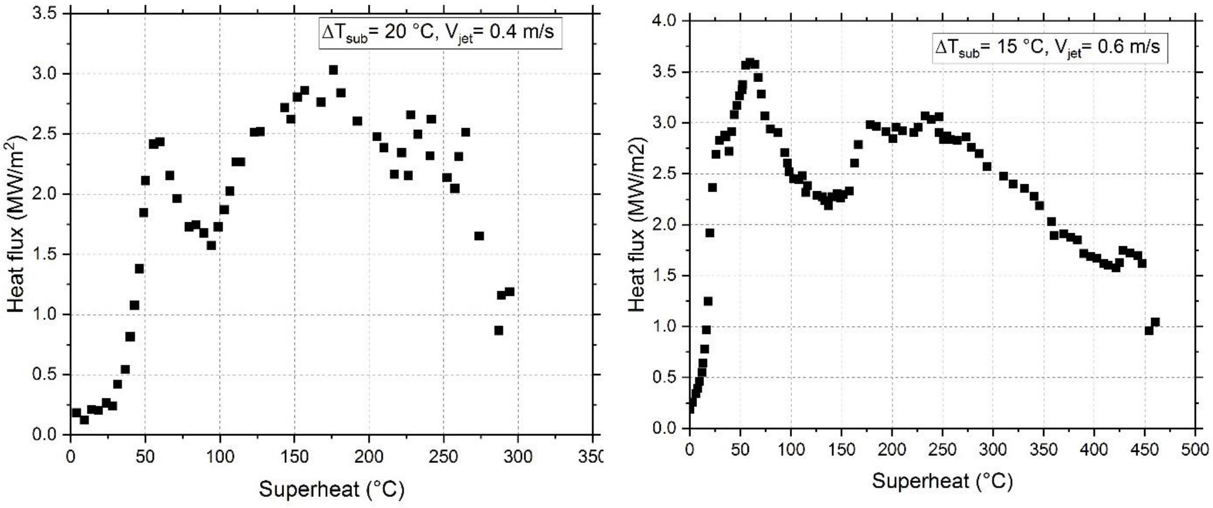

a b

Figure 1.6: JIB curves in the stagnation zone obtained by [8] (a) and [9] (b).

1.2.1.1. Microbubble Emission Boiling

Microbubble emission boiling (MEB) is a boiling phenomenon that occurs in the transition regime at relatively high degree of subcooling or relatively high velocity in flow boiling. During MEB, a coalesced bubble is broken into microbubbles on the heated surface resulting in an enhancement in the wettability of the dried surface with the subcooled liquid. Hence it increases the surface heat flux. MEB is usually accompanied by high noise and vibration[10].

In the literature, there is a lack of understanding of the mechanism associated with MEB and the conditions at which the phenomenon occurs. Some publications reported the occurrence of MEB at high degrees of subcooling in pool boiling [4,11–13] and flow boiling in channels [10,14,15]. Yet, these studies did not investigate the shoulder phenomenon, as the degree of superheat was relatively low (i.e.,100 °C). Ando et al. [11] investigated MEB experimentally in pool boiling on a circular copper surface with 5 mm and 10 mm diameters. They used high-speed imaging to visualize the repeated cycle of bubble growth and collapse. They provided visualized evidence of the role of microbubbles in driving the subcooled liquid towards the boiling surface. They found that the repetitive bubble cycle occurred with frequency of 800-2000 Hz. Tang et al. [12] carried out experiments to investigate MEB in pool boiling of water at different degrees of subcooling (0-60 °C). The results showed that at subcooling below 20 °C, the boiling curve exhibited a transition from the CHF to the film boiling regime without observation of MEB, while the MEB phenomenon appeared when subcooling was equal or greater than 20 °C. Also, increasing the subcooling caused the MEB to take place at a lower degree of superheating, as shown in Figure 1.7. With the aid of a high-speed camera, they observed a large vapor bubble/layer with a vigorous oscillating interface formed on the heated surface. During MEB, at subcooling of 20 °C , the large vapor bubble did not collapse nor depart the surface , while increasing the subccoling resulted in a partial collapse of the vapor bubble/layer. They concluded that subcooling of 20 °C is the threshold at which the MEB is triggered.

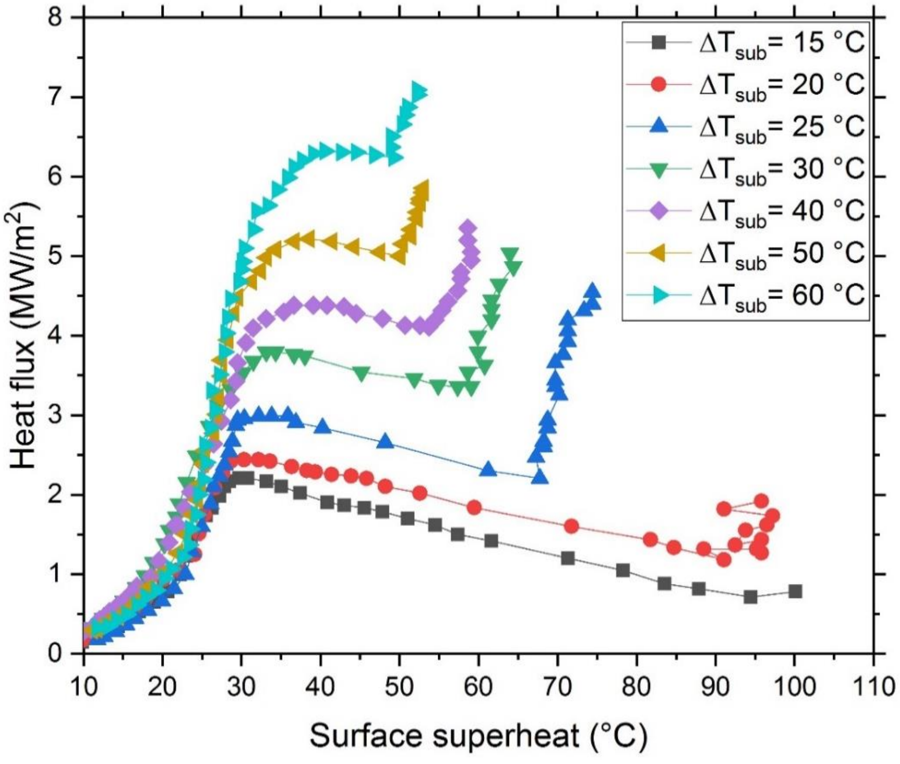

Figure 1.7: Effect of subcooling on MEB in pool boiling[12].

Nakamura et al. [16] investigated the MEB experimentally in pool boiling on different heating elements, a platinum wire of 0.3 mm in diameter, and a circular copper surface of 7 mm in diameter at subcooling of 40 °C and 60°C. They observed the occurrence of MEB on the flat surface but not on the wire surface. They attributed the existence of MEB to the effect of bubble formation on a flat surface.

Kawakami et al. [13] investigated the effect of space limitation on MEB in the transition regime in subcooled pool boiling. They limited the space above the boiling surface to 3 mm using a solid rod which caused an artificial imbalance between the condensation rate from the top of the coalesced bubble and the evaporation rate on the heated surface. They did that by controlling the subcooled water delivered to the surface. They found that the transition of boiling behavior from CHF to film boiling or MEB depended on the boiling space above the heated surface. Limiting the space above the boiling surface promoted the surface dryout and transition to film boiling. Figure 1.8 shows the effect of spatial restriction on the boiling curve at a subcooling of 40 °C. For an open space (no restriction applied), the transition from CHF to MEB occurred at a high flux of 7 MW/m^2. For a restricted space, they found two patterns occurred, depending on the heat flux value at which the restriction was applied. For example, the boiling curve exhibited transition from CHF to film boiling and from CHF to MEB when the space was limited below and above 4 MW/m^2, respectively.

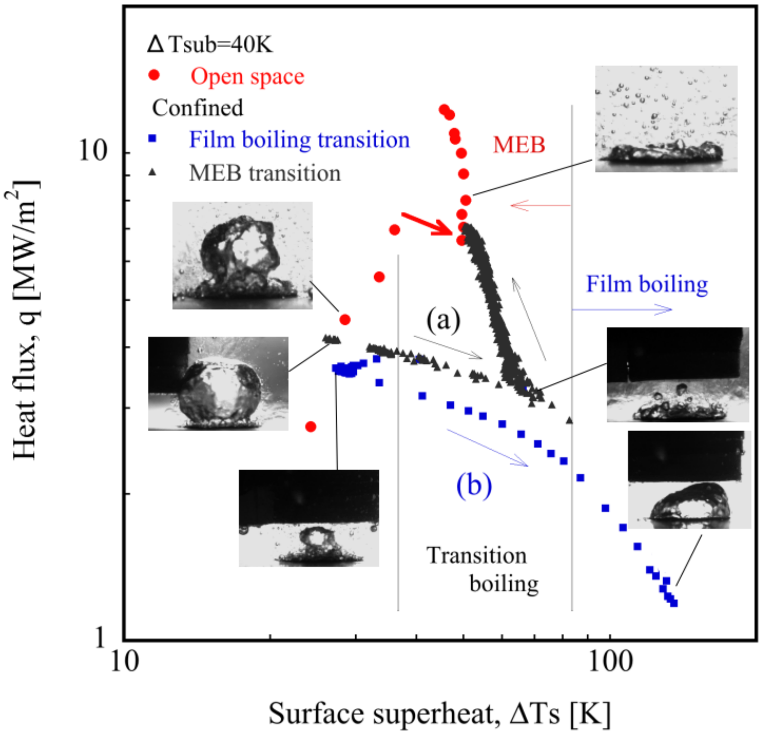

Figure 1.8: Effect of spatial restriction on the boiling curve[13].

Suzuki et al. [10] Studied the MEB phenomenon in subcooled flow boiling in a rectangular channel. They investigated the effect of subcooling (10 °C - 40 °C), flow velocity (0.01 m/s -1.5 m/s), and heated copper surface length (10 mm - 40 mm) on the behavior of MEB. The results revealed that, for the same flow conditions, MEB occurred in the case of the shorter heater (i.e., 10 mm), compared to the case of the longer heater (> 10 mm). They observed that MEB was triggered at subcooling above 20 °C at low velocities. However, increasing the flow velocity promoted the occurrence of MEB at very low subcooling. Increasing the subcooling and flow velocity accelerated what they called a stormy MEB, in which the heat flux increased after the CHF, with a loud boiling sound which was confirmed by [17] at subcooling as high as 40 °C in flow boiling in a channel at a velocity of 0.5 m/s. The effects of subcooling and flow velocity on MEB behavior are shown in Figure 1.9. In a later study, Suzuki et al. [18] found that not only does the heater area affect the occurrence of MEB in the transition regime, but the heating element's heat capacity has an effect as well.

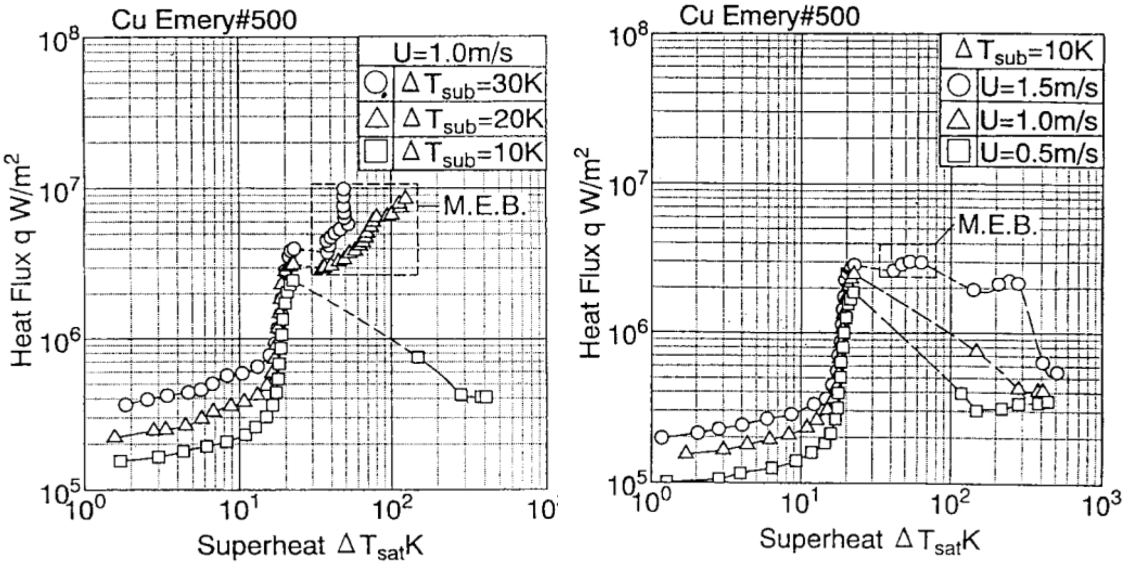

a

b

Figure 1.9: MEB behavior on a heater of 10 mm in length at different subcoolings (a) and flow velocities (b) [10].

1.2.1.2. Heating Techniques

It is worth mentioning that the research carried out by [6,7,9,19] used a similar experimental setup in which the boiling surface was heated using a resistive electric element made of thin NiCr foil, as shown in Figure 1.10. In the aforementioned papers, the experimental conditions were limited to a jet velocity of 1 m/s and subcooling of 20 °C. It was problematic to carry out steady-state JIB experiments at higher jet velocities and degrees of subcooling due to the burnout of the heating elements. Induction heating could be an alternative solution for such a technical challenge. It has the merits of high localized heating in short times without physically contacting the heated surface. When a conductive workpiece is placed inside the induction coil, an eddy current is induced inside the workpiece by the variable magnetic field then heat is generated inside the workpiece by the Joule effect [20].

Many researchers have used induction heating [21–23] to perform steady-state boiling experiments at high heat fluxes. Hernández et al. [21,22] investigated the effect of water mist characteristics, i.e., water impact density, droplet size, and droplet velocity on the entire boiling curve under steady-state conditions. They used a Platinum- disk with a diameter of 8 mm subjected to water-air mist. They could attain heat fluxes as high as 12 MW/m^2 and high surface temperatures up to 1200°C.

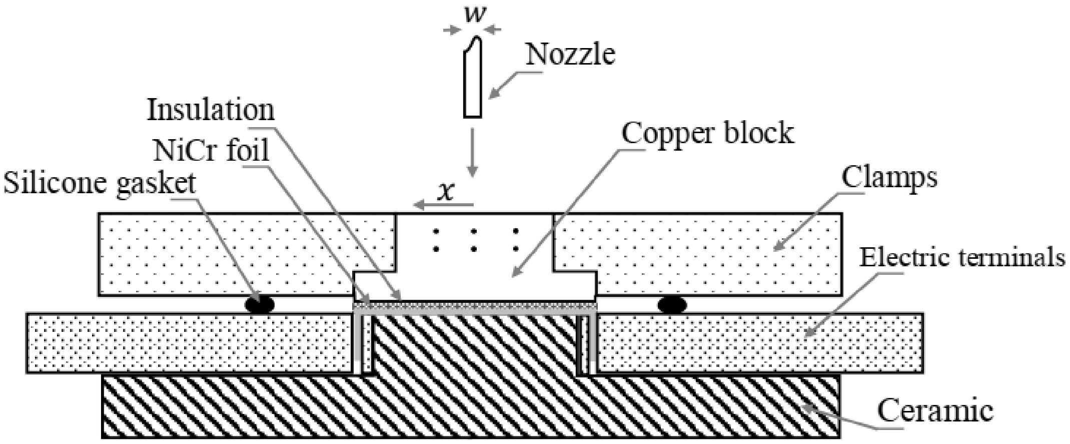

Figure 1.10: Experimental setup used in previous works[9].

One can conclude from this section that few works have investigated the boiling heat transfer experimentally in the stagnation area under impinging jets at steady-state conditions. Due to the technical challenge in the experimental setup, the flow conditions were limited to low jet velocities and low degrees of subcooling. The boiling behavior after the CHF in the transition regime and the shoulder heat flux is not yet fully understood. Some studies reported the existence of the first minimum of the heat flux within the transition regime, others did not observe it. It is believed that the first minimum is similar to the MEB phenomenon that has been reported in pool boiling studies at high degrees of subcooling or high flow velocities in subcooled flow boiling.

1.2.2. Modeling Approaches of Bubble Dynamics

There are two approaches to model the wall heat flux in JIB: (1) global modeling and (2) mechanistic modeling. In the former, the heat flux is correlated as a function of process parameters such as degree of subcooling, jet velocity, fluid properties, surface to jet area ratio, etc. In this case, the underlying physics is not explicitly represented in the produced model. Many investigations have focused on the global modeling of nucleate boiling under impinging jets [1,2]. In mechanistic modeling, the wall heat flux is represented as a sum of a number of wall heat flux partitions. Each partition represents an underlying physical contributing mechanism. The concept of wall heat flux partitioning was proposed and developed by Kurul and Podowski [24], presented in equation (1.1). They divided the total wall heat flux, $q_w^{"}$, into three partitions, as shown in Figure 1.11. The first partition, $q_{ev}^{"}$, represents the rate of heat transfer due to evaporation and formation of vapor bubbles. Once the bubbles depart the heated surface, subcooled liquid replaces the volume that was occupied by the departed vapor bubbles, hence resulting in a transient heat transfer, $q_q^{"}$, which is sometimes referred to as the heat transfer rate due to quenching. The rest of the heat transfer rate is due to convection to the bulk liquid, $q_c^{"}$. It can be clearly seen from equation (1.2) that the wall heat flux partitioning model depends on a number of key parameters that are related to bubble dynamics, including the bubble departure diameter D_b, bubble release frequency f, and density of active nucleation sites N_a . Consequently, submodels relating these key parameters to the jet and surface conditions are needed and must be developed.

$$q"_w = q"_q + q"_{ev} + q"_c \tag{1.1}$$

$$q"_w = \frac{2\sqrt{\rho_l c_{p,l} k_l t_w}}{\sqrt{\pi}} A_{2p} f\left(\Delta T_{sup} + \Delta T_{sub}\right) + \rho_v h_{fg} \frac{\pi}{6} D_b^3 f N_a$$

$$+ h_c A_{1p}\left(\Delta T_{sup} + \Delta T_{sub}\right) \tag{1.2}$$

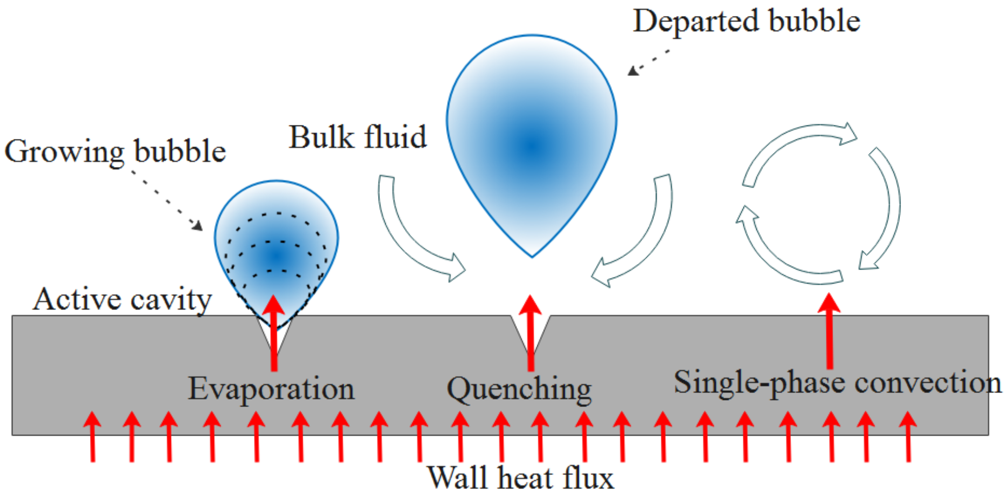

Figure 1.11: Schematic of wall partitioning heat flux concept.

Significant attention has been given to understanding and modeling bubble dynamics in pool and flow boiling [25,26]. In these studies, models of the bubble departure diameter (BDD) have been developed empirically or analytically. However, the literature lacks investigations that focus on bubble dynamics in jet impingement boiling (JIB). Sections1.2.2.1 and1.2.2.2 summarize experimental and analytical studies carried out on bubble dynamics.

1.2.2.1. Empirical Modeling

Unal[27] studied experimentally bubble dynamics during subcooled water flow boiling using high-speed imaging. Unal measured bubble diameters during boiling experiments for degrees of subcooling in the range of 3 to 86 ºC, flow velocities from 0.08 to 9.15 m/s, and pressures from 1 to 177 bar. A semi-empirical model to predict the average maximum bubble diameter was developed. He considered the heat added from the micro-liquid layer underneath the vapor bubble and heat loss from the upper half of the bubble to be the main mechanism for bubble growth. Furthermore, the contribution of the superheated layer was neglected because its thickness was small compared to the bubble departure diameter.

Prodanovic et al. [28] studied experimentally the bubble growth and departure in subcooled water flow boiling considering flow velocities of 0.08 - 0.8 m/s; subcooling degrees of 10 - 30 ºC; and pressures of 1.05 - 3 bar. They investigated the effect of flow velocity, heat flux, liquid subcooling, and pressure on the maximum bubble diameter. The results showed that bubble volume decreased with the degree of subcooling, fluid velocity, and heat flux. They observed a scatter in bubble measurements which was attributed to measuring bubbles at different nucleation sites and due to variations of local temperature and in the velocity field.

Basu et al. [29] investigated subcooled water flow boiling in a horizontal pipe considering mass fluxes in the range of 124 to 926 Kg/m^2.s, heat fluxes from 25 to 900 kW/m^2, and system pressures from 1.03 to 3.2 bar. They presented a correlation to predict the diameters of bubble departure and lift-off. They studied the effect of degree of subcooling in the range of 0 - 46 ºC, wall superheat of 5 -19 ºC and flow velocity of 0- 0.9 m/s. They found that the BDD increased with the wall superheat and decreased with the flow velocity and degree of subcooling. However, the effect of the degree of subcooling was not significant for the range of parameters considered in their experiments. The results of experimental work carried out by Sugrue et al. [30] confirmed the increase in the BDD with the increase in heat flux during subcooled water flow boiling. Also, the increase in the mass flux, surface orientation, liquid degree of subcooling, and pressure resulted in a decrease of the BDD. However, no empirical correlation was proposed.

Brooks and Hibiki [31] proposed a semi-empirical correlation to predict the BDD during subcooled flow boiling in a vertical channel. The model predicted the measurements of BDD reported in the literature with a maximum deviation of 30 %. Du et al. [32] proposed another correlation to predict the BDD in subcooled water flow boiling in horizontal and vertical channels with an average relative deviation of 19.7 %.

Ren et al. [33] studied experimentally the BDD in subcooled water flow boiling in a channel. They investigated the effect of the degree of subcooling, surface temperature, and flow rate on the BDD and the bubble growth rate. Their results indicated that the BDD increased with the wall superheat and decreased with the degree of subcooling and the flow rate, which is in agreement with previous works. They proposed an empirical model to predict the BDD with a maximum deviation of 30 %. Levin and Khan [34] studied experimentally bubble dynamics during subcooled flow boiling of water. They investigated the effect of the degree of subcooling and unsteady heat flux on the maximum bubble diameter. Their results revealed that models developed under steady-state boiling conditions could not accurately predict bubble diameter under transient heat flux conditions. They applied the correlation developed by Prodanovic et al. [28] with modified coefficients to predict their experimental data with an average variation of 15 %. Zhou et al. [35] investigated experimentally the BDD in subcooled water flow boiling in a horizontal channel considering degrees of superheat from 7 to 14 ºC, flow velocities from 1.0 to 2.0 m/s, degrees of subcooling from 5 to 12 ºC, and system pressures from 121 to 232 kPa. They developed an empirical model for the BDD and correlated the BDD to the degree of subcooling, wall superheats, flow velocity, and system pressure. The model achieved good accuracy with maximum deviation of deviation of 12.7 %.

Few studies in the literature investigated the bubble dynamics under jet impingement boiling. Omer[36] experimentally investigated bubble dynamics in the parallel flow region of an impinging free water jet using high-speed imaging considering jet velocity of 0.4-1.7 m/s, degree of subcooling of 10-28 ºC, and wall superheat of up to 0-30 ºC. Omar developed an empirical correlation of the BDD in the parallel zone as a function of the degree of subcooling, wall superheat, the jet velocity with a maximum deviation of 35 %. The maximum deviation of Omar's model compared with the models developed by Unal et al. [27] and Basu [29] was within ± 50 %. Omar attributed such deviation to the difference between boiling configurations, JIB vs flow boiling. Ahmed [37] extended Omer's study [36] using the same experimental setup to investigate bubble dynamics in the stagnation zone of a free impinging jet. The bubble growth rate and the BDD were measured considering the jet velocity of 0.65 - 0.9 m/s and water subcooling of 13 - 30 ºC. No empirical correlation was developed. Table 1.1 presents a summary of the empirical BDD models available in the literature for flow and Jet impingement boiling.

1.2.2.2. Mechanistic Modeling

In the mechanistic modeling approach, the growth and departure of a bubble on a heated surface are governed by the thermal (heat) balance and momentum (force) balance experienced by the vapor bubble. Klausner et al. [38] presented an analytical model to predict the average bubble diameter in saturation flow boiling of R113. The model considered the balance of all forces experienced by the vapor bubble growing on the heated surface. They also used the bubble growth model developed by Mikic et al. [39]. Many studies adopted Klausner's force balance approach and applied some improvements to the

Table 1.1: Empirical models for BDD available in the literature.

Author	Model
Prodanovic et al [28]	$\frac{D_b\sigma}{\rho_l\alpha^2} = 236.749Ja_{sup}^{-0.581}\left(\frac{T_w - T_l}{T_w - T_{sat}}\right)^{-0.8843}(\rho_l/\rho_v)^{1.772}BO^{0.138}$
Basu et al. [29]	$\frac{D_b}{\sqrt{\sigma/g\Delta\rho}} = 1.3(sin\gamma)^{0.4}[0.13\exp(-1.75\times 10^{-4}Re + 0.005)]$ $\times Ja_{sup}^{0.45}\exp(-0.0065Ja_{sub})$
Brooks and Hibiki[31]	$\frac{D_b}{\sqrt{\sigma/g\Delta\rho}} = 2.11\times 10^{-3}(\rho_l/\rho_v)^{-0.78}Bo^{0.44}Pr^{1.72}\left(Ja_{sup}\times\frac{T_w - T_l}{T_w - T_{sat}}\right)^{-0.49}$
Du et al. [32]	$\frac{D_b}{\sqrt{\sigma/g\Delta\rho}} = 10^{7.196}\times(\rho_l/\rho_v)^{-0.319}{Ja_{sup}}^{0.123}Re^{-0.751}Pr^{-1.939}$ (horizontal) $\frac{D_b}{\sqrt{\sigma/g\Delta\rho}} = 10^{-0.433}\times(\rho_l/\rho_v)^{-0.018}{Ja_{sup}}^{0.261}Re^{-0.323}Pr^{3.381}$ (vertical)
Ren et al. [33]	$\frac{D_b}{\sqrt{\sigma/g\Delta\rho}} = 0.34Ja_{sup}^{1.4}\exp(-0.114Ja_{sub})\,Re^{-0.36}$
Zhou et al. [35]	$\frac{D_b}{\sqrt{\frac{\sigma}{g\Delta\rho}}} =$ $10^{2.4086}(\rho_l/\rho_v)^{-0.6613}{Ja_{sup}}^{0.1557}{Ja_{sub}}^{-0.0159}Re^{-0.6647}Pr^{-1.8477}sin\gamma^{0.4}$
Omer [36]	$D_b = 2.3136 - 0.00261\times Re + 3.6896\times 10^{-7}\times Re^2 - 0.01055\times Ja_{sub}$ $+ 9.95\times 10^{-5}\times Ja_{sub}^2 + 0.127\times Ja_{sup} - 0.00146\times Ja_{sup}^2$

model parameters and used several modified bubble growth rate models [35,40,41]. In Klausner's model, a growing bubble would depart the heated surface if any of the two force balance equations ($\sum F_y=0$ and $\sum F_x= 0$) is violated. If the force balance in the x-direction (i.e., parallel to the flow direction) is violated, the bubble will slide. If the unbalance occurs in the y-direction (i.e., normal to the flow direction), the bubble will lift off.

Zuber [42] studied bubble growth during pool boiling on a heated surface. He proposed a bubble growth model with a correction factor, b, for saturation boiling and heat flux as low as 23.3 kW/m^2. Correction factor b was introduced to account for the effect of the non-sphericity of the vapor bubble. Cooper and Lloyd [43] considered the evaporation of the liquid microlayer underneath a bubble as the most important mechanism for bubble growth. They developed a bubble growth model in a saturated pool boiling with a proposed empirical constant C = 0.8 that appears in the initial thickness of the microlayer. Mikic et al. [39] derived a simple bubble growth model in saturation and subcooled pool boiling that was applicable for both heat diffusion-controlled and inertia-controlled growth ranges.

Yun et al. [40] modeled BDD in subcooled flow boiling. They applied the force balance proposed by Klausner et al. [38] and the bubble growth rate developed by Zuber[42]. Their model considered heat loss from the bubble top side. They assumed that the top half of the bubble surface area was in contact with the subcooled fluid. They proposed a modified correction factor b =1.56 that was originally introduced by Zuber [42]. However, the contribution of the microlayer to the bubble growth was not considered. The most recent studies in flow boiling [35,44–46] adopted Klausner's force balance approach and bubble growth models that consider the contribution of the superheated layer, the evaporation of the microlayer to the bubble growth rate, and also the effect of the heat loss from the bubble surface area exposed to the subcooled liquid.

Colombo and Fairweather [44] developed a bubble growth model that considered three mechanisms contributing to the bubble growth rate. The first mechanism was the heat transfer from the superheated layer to the growing bubble that was calculated as proposed by Plesset and Zwick[47]. The second mechanism accounting for the contribution of microlayer evaporation was calculated following Cooper and Lloyd [43] with a proposed empirical constant C=1.78, which was selected to best fit their experimental data in flow boiling. The third mechanism considered the effect of heat loss from the growing bubble. The model developed by [44] was able to predict the experimental data reported in the literature with an average relative deviation of 26.8 %. Raj et al. [45] evaluated the contribution of each heat transfer mechanism to the bubble growth rate. Their results showed that the contribution of microlayer evaporation was significant compared to the other two mechanisms and the heat loss from the bubble top side was important at heat fluxes as low as 100 kW/m^2. Zhou et al. [35] adopted the same model as used by [44] with a modified parameter C=1.45 achieving good agreement with their experimental data with an average relative deviation of 12 %.

Regarding studies in JIB, Omer and Hamed [48] developed an analytical model to predict the termination scenario of a growing bubble in the parallel flow area under an impinging jet. Their model calculated the maximum bubble diameter independently from the dynamic equilibrium condition (force balance) and the thermal equilibrium condition (heat balance). The minimum of the two diameters was considered the BDD. They applied Zuber's model with a modified correction factor b = 0.3. Ahmed [37] applied the force balance approach and different bubble growth models to predict the average BDD within the stagnation zone in JIB. Ahmed assumed that a growing bubble in the stagnation zone would depart the surface when the force balance in the y-direction (normal to the surface) is violated. The model captured his experimental data with a normalized root mean squared deviation of 21 %. A summary of bubble growth models available in the literature is presented in Table 1.2.

Table 1.2: Bubble growth models available in the literature.

Author	Growth model	Boiling configuration	Superheated layer	Microlayer	Condensation
Plesset and Zwick[47]	$R(t) = 2\sqrt{\frac{3}{\pi}}\frac{k_l(T_{sup} - T_l)}{\rho_v h_{fg}}\sqrt{\frac{t}{\alpha}}$	Pool		✓	
Zuber [42]	$R(t) = \frac{2b}{\sqrt{\pi}} Ja\,\sqrt{\alpha t}$, 1<b< $\sqrt{3}$	Pool	✓		
Cooper and Lloyd[43]	$R(t) = \frac{2}{C} Ja\, Pr^{-0.5}\sqrt{\alpha t}$, C=0.8	Pool		✓	
Mikic et al. [39]	$R(t) = 2\sqrt{\frac{3}{\pi}} Ja\,\sqrt{\alpha t}\left\{1 - \frac{(T_w - T_l)}{(T_w - T_{sat})}\left[(1 + \frac{t_w}{t})^{1/2} - (\frac{t_w}{t})^{1/2}\right]\right\}$	Pool	✓		✓
Van Stralen et al. [49]	$R(t) = 0.470\, Ja\, Pr^{\frac{1}{6}}\sqrt{\alpha t}$	Pool	✓	✓	
Yun et al. [40]	$R(t) = \frac{2b}{\sqrt{\pi}} Ja\,\sqrt{\alpha t} - \frac{b q_c''}{2\,\rho_v h_{fg}} t$, b=1.56, $q_c'' = h_c(T_{sat} - T_l), h_c = \frac{k}{D_b}(2 + 0.6 Re_d^{0.5} Pr_l^{0.3})$	Flow boiling	✓		✓

Continue Table 1.3: Bubble growth models available in the literature.

Author	Growth model	Boiling configuration	Superheated layer	Microlayer	Condensation
Colombo and Fairweather [44]	$R(t) = 2\sqrt{\frac{3}{\pi}} k_l\left(T_{sup} - T_l\right)\sqrt{\frac{t}{\alpha}} \times (1- f)+\frac{2}{C}\, Ja\, Pr^{-0.5}\sqrt{\alpha t} - \frac{h_c}{\rho_g h_{fg}}(T_{sat} - T_l) \times f$, C=1.78	Flow boiling	✓	✓	✓
Omer and Hamed[48]	$R(t) = \frac{2b}{\sqrt{\pi}}\, Ja\, \sqrt{\alpha t}$, modified b=0.3	JIB	✓		✓
Ahmed [37]	$R(t) = \frac{2b}{\sqrt{\pi}}\, Ja\, \sqrt{\alpha t} - \frac{b q_c''}{2\, \rho_v h_{fg}} t$, modified b=π/7	JIB	✓		✓

Most studies summarized in Table 1.2 focused on bubble dynamics during the pool and flow boiling. The available bubble growth models during JIB considered two heat transfer mechanisms representing heat transfer from the superheated layer and heat loss by convection to the subcooled liquid. Yet they ignored the heat addition due to microlayer evaporation. In addition, no empirical models have been developed to predict the BDD within the stagnation zone of the impinging jets. There is a need to expand the scope of investigating bubble dynamics within the stagnation zone under jet impingement boiling conditions, considering the effect of wall superheat, degree of subcooling, and jet velocity. The development of empirical and mechanistic models of bubble dynamics under JIB conditions is one of the main objectives of the present study.

1.3. Transition Boiling

Seiler-Marie et al. [50] attempted to develop a mechanistic model of the wall heat flux under jet impingement boiling. They assumed that the heat flux within the shoulder region was due to jet hydrodynamic fragmentation causing periodic bubble oscillations at the heated surface. They analyzed the experimental data obtained by Robidou[51], as shown in Figure 1.12. They hypothesized that the wall heat flux in the transition regime is mainly due to the heat transfer to the subcooled fluid that rushed to the heated surface and ignored the amount of heat used in liquid vaporization. The boiling mechanism presented in [50]considered a Rayleigh-Taylor instability at the vapor-liquid interface that resulted in fragmentation of large bubble and hence spray-like wetting of the heated surface, which led to the removal of high heat fluxes at the surface. However, the study did not provide visualized evidence to verify this hypothesis. They proposed the total wall heat flux mechanistic model as expressed in equation (1.3).

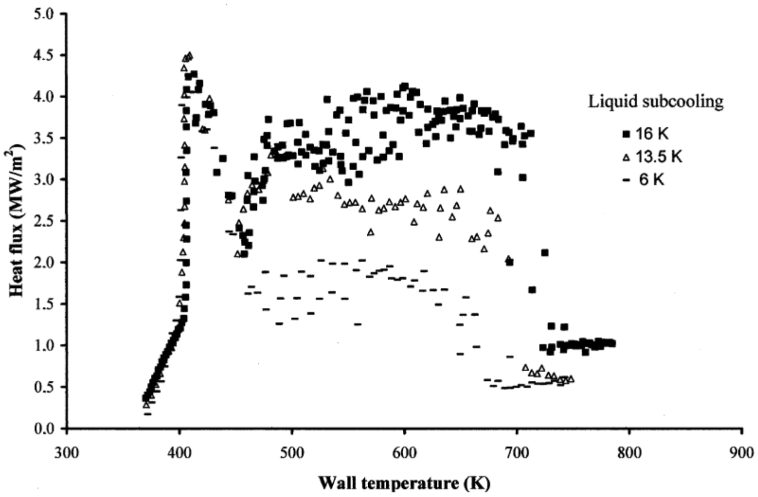

Figure 1.12: Boiling curves at the stagnation obtained by Robidou[51].

$$q''_{sh} = K\rho_l \left(\frac{\sigma}{\rho_l - \rho_v}\right)^{1/4} C_{p,l}\,\Delta T_{sub} \left(\frac{V_j^2}{D_j} + g\right)^{1/4} \qquad (1.3)$$

Where K is an empirical constant. A value of K = 0.15 was suggested by [50] for the experimental range that they considered in their study, $0.64 \leq V_j \leq 0.96\ \mathrm{m/s}$, $5 \leq \Delta T_{sub} \leq 19\ ℃$, and $D_j = 1.8$ mm).

To the best of my knowledge, only Bogdanic et al. [52] and Ahmed and Hamed [9] measured the vapor breakup frequency within the transition boiling regime during steady-state JIB experiments. Bogdanic et al. [52]investigated the vapor breakup frequency in the stagnation zone under an impinging water jet using a miniaturized optical probe at a degree of subcooling of 20 °C, jet velocity of 0.4 m/s, and up to surface temperature of 400 °C. Their results showed that the frequency increased dramatically with surface temperature, as shown in Figure 1.13. They observed that the heated surface was almost covered by vapor at the first minimum and the liquid jet penetrated the vapor layer with a frequency of 900 Hz. The vapor layer frequency increased to 2 kHz at the beginning of the shoulder heat flux region by increasing the surface temperature. They developed a simple empirical model to predict the shoulder heat flux. They considered the shoulder heat transfer as the sum of the transient heat due to the intruded liquid and the heat due to the vaporization of the intruded liquid that touches the heated surface.

The authors[53] considered that the surface rewetting frequency contributed significantly to the heat transfer in the transition regime. Yet the trend of vapor breakup frequency was not aligned with that of the transition heat flux. They assumed that a decrease in liquid contact time during the shoulder heat flux might compensate for the dramatic increase in contact frequency. However, their results showed that the liquid contact time remained almost constant. They hypothesized that it was difficult for the liquid to wet the surface at high wall temperatures, as the generated vapor repels the liquid away from the surface and reduces the possibility of surface rewetting. Although no experiments were carried out at a degree of subcooling higher than 20°C, they anticipated that the vapor layer frequency would increase with increasing the degree of subcooling. This matter warrants more investigation, which is one of the objectives of this study.

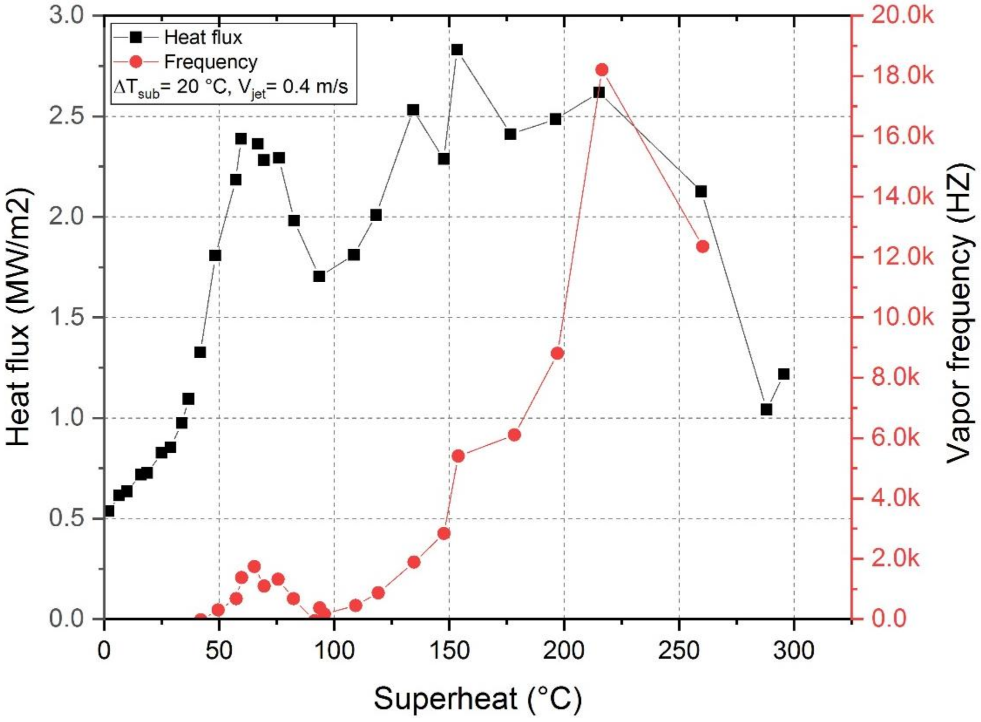

Figure 1.13: Variation of surface heat flux and vapor layer breakup frequency with surface superheat [52].

Ahmed and Hamed [9] used high-speed imaging and a fiber optic probe to study the liquid-vapor interface within the transition regime at the stagnation area under JIB conditions. They considered jet velocity of 0.6 m/s and degree of subcooling of 15 °C. Their high-speed images confirmed the existence of RT instability at the liquid-vapor interface. The frequency measurements carried out by Ahmed and Hamed [9] showed that the trend of vapor breakup frequency was in agreement with the trend of heat flux obtained in the transition regime. They did not observe a dramatic increase in the vapor breakup frequency with the surface temperature, as shown in Figure 1.14.

They hypothesized that not all the liquid volume in contact with the heated surface evaporated. However, only the layer that touched the wall did while the rest of the liquid lost the energy required for vaporization. Based on their high-speed imaging, they proposed a mechanistic model that considered two wetting mechanisms(i) wetting by direct contact between the liquid and the heated surface and (ii) partial wetting by the liquid jets that intruded through the vapor layer due to the RT instability. The wall heat flux was divided into two components: quenching heat flux and intrusion heat flux. Both coexisted during the transition regime. Details of their model are presented in Chapter 5.

Looking at some of the works that have been carried out within the transient and the film boiling regimes might enhance our understanding of the heat transfer mechanisms involved in the transition boiling regime. Jones et al. [53] used X-ray imaging synchronized with high-speed imaging to study the cycle of vapor film formation and collapse during film boiling during transient experiments. Based on the high X-ray images, the study concluded that the following two mechanisms affected the vapor film formation and collapse: (i) the liquid-vapor instability, which affected the way the liquid reached and wetted the surface; and (ii) liquid vaporization, which determined the reformation of the vapor layer.

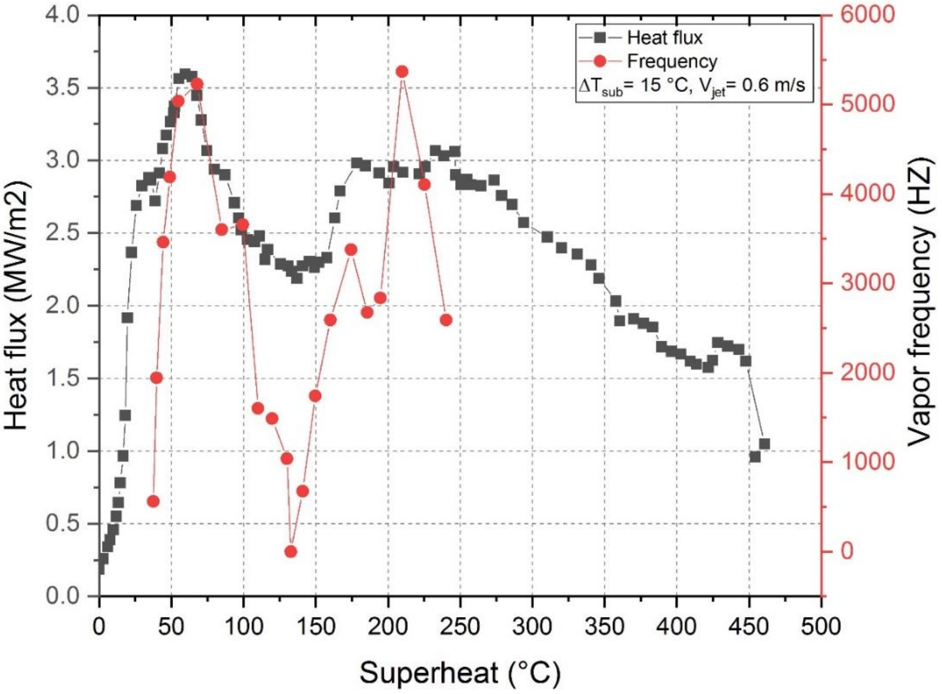

Figure 1.14: Variation of surface heat flux and vapor layer breakup frequency with surface superheat[9].

Gomez et al. [54] used high-speed imaging to study the rewetting mechanism in the stagnation zone during quenching of high-temperature surfaces by water jet at velocity of 3.1 m/s and degree of subcooling of 75 °C. The results revealed the existence of what they called explosive boiling and intermittent wetting and dryness frequency when the liquid touches a hot surface at a high temperature. Based on their observations, they presented an interpretation for the explosive boiling cycle. When the subcooled liquid touches a surface at high temperature, the liquid temperature adjacent to the wall increases rapidly beyond the saturation temperature and reaches the thermodynamic limit of superheat TLS (302 °C for water), the superheated water experiences a vigorous phase change called explosive boiling which cause the generated bubble to grow rapidly. When the bubble size exceeds the superheated liquid layer, it touches the subcooled liquid and collapses. Then the cold liquid ruches to the surface to reform the superheated layer and repeat the cycle. They observed a relationship between the explosive boiling frequency and the area of vapor patches. The frequency of explosive boiling is significantly higher in small vapor patch areas compared to that that happened over the total stagnation area.

Based on the literature review presented above, one can conclude that few studies have attempted to investigate the boiling curve under JIB using steady-state experiments. These studies considered relatively low jet velocities (up to 1 m/s) and low degrees of subcooling (up to 20 °C). In previous works, the high instability of the jet and high heat flux in the transition regime caused the heater element to burn out, making it challenging to investigate JIB in the stagnation area at high heat fluxes. The technical challenge warranted using a different heating technique which was carried out in the current study. In the nucleate boiling regime, the literature is rich with empirical and mechanistic models to predict the bubble growth rate and BDD during pool boiling and flow boiling. However, there is a need to expand the scope of bubble dynamics investigation to the jet impingement boiling conditions. Furthermore, the experimental data of vapor breakup frequency within the transition boiling regime is lacking, which hindered previous efforts to develop a sound mechanistic model of the shoulder heat flux region.

1.4. Research Objectives

The main objectives of this study are:

1. Study JIB under a wider range of jet and surface parameters. This required a redesign of the heating technique of the heated boiling surface.
2. Obtain the entire boiling curve using steady-state experiments under the expanded jet and surface parameters.
3. Develop empirical and mechanistic models of bubble growth rate and bubble departure diameter within the stagnation zone during JIB in the nucleate regime.
4. Study the effect of the degree of subcooling on the vapor breakup frequency within the stagnation zone during JIB in the transition regime.
5. Develop a mechanistic model of the transition heat flux.

1.5. Thesis Outline

The thesis consists of six chapters containing the following:

Chapter One:	Introduction of JIB, its applications, literature review, and research objectives.
Chapter Two:	Description of the experimental facility and experimental procedures.
Chapter Three:	The experimental results of the boiling curve at different jet velocities and degrees of subcooling.
Chapter Four:	Results and discussion of bubble dynamics measurements in the nucleate boiling regime and the proposed empirical and mechanistic models.
Chapter Five:	Results and discussion of vapor layer breakup frequency measurements in the transition boiling regime and the proposed mechanistic model.
Chapter Six:	Conclusions and recommendations for future work.
Appendices:	Experimental data of BDD and measurements uncertainty.

2. Chapter 2: Experimental Facility

2.1. Facility Description

Figure 2.1 shows the experimental setup used in the current study. The setup consists of a flow loop, a heater block, and a data acquisition system. A distilled water is circulated from a 60-liter tank to the test section by a 0.5 HP centrifugal pump. A 3 kW immersion heater was used to heat the water in the collecting tank to the desired temperature. An accumulator was installed at the discharge line to reduce flow fluctuation. The volume flow rate was controlled using a globe valve and measured by a turbine flow meter (Omega FTB-9504)). A type-T thermocouple was used to measure the water temperature at the nozzle inlet. The heated water flows through a nozzle that normally impinges on the heated surface, after which water is returned to the collecting tank. The vertical distance between the nozzle and the heated surface was 10 mm. Two different nozzles were used in the current study. The same planar nozzle used by [37] with the dimensions of 1×8 mm^2 was used to investigate the boiling curve at high operating conditions. A circular nozzle with a diameter of 8 mm was used to investigate the bubble dynamics in the nucleate boiling regime and the vapor layer breakup frequency in the transition regime.

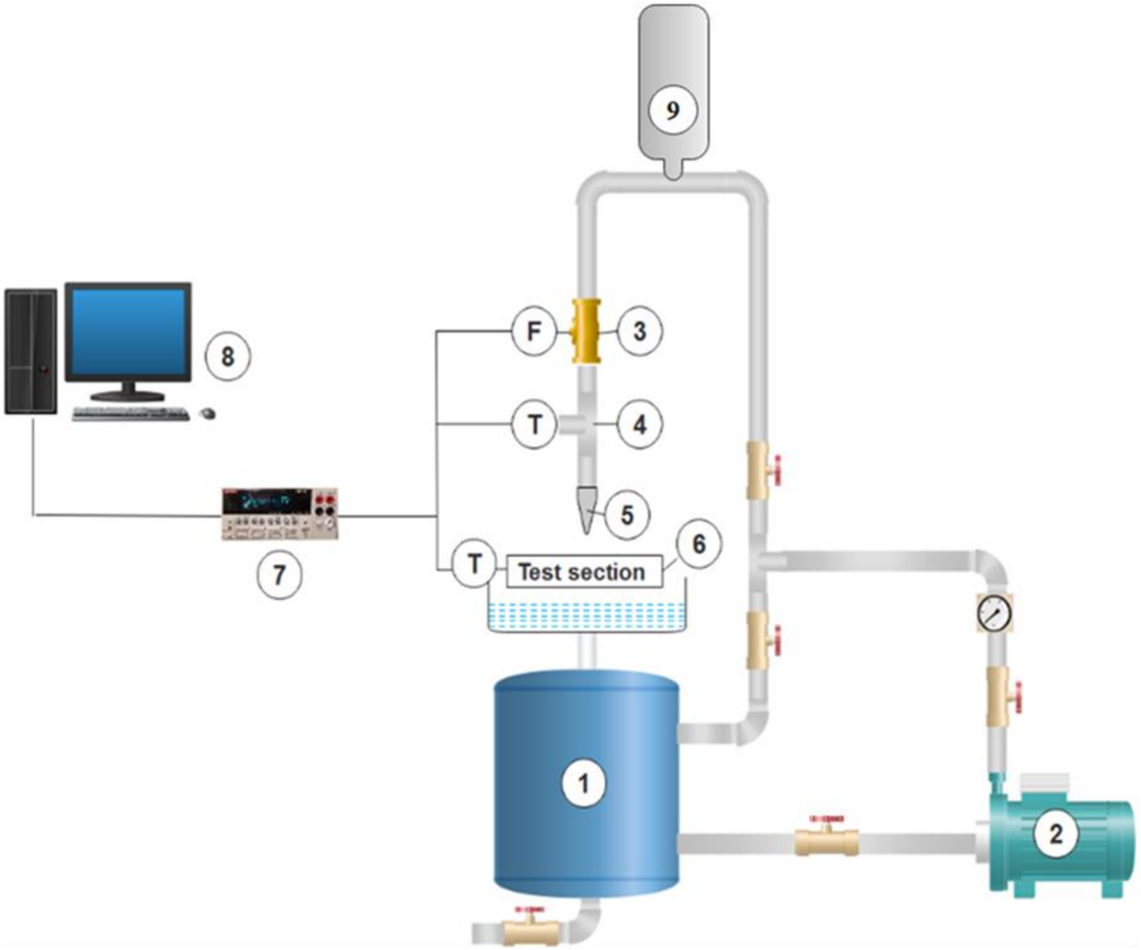

1-Water tank, 2-Centrifugal pump, 3-Turbine flow meter, 4-Thermocouple,
5-Round nozzle, 6-Heater block, 7-DAQ, 8-PC, 9- Accumulator

Figure 2.1: Layout of the experimental setup.

2.2. Boiling Module

Figure 2.2 shows a schematic of the heater block used in the present study. The heater block consists of a copper cylinder fitted inside a hollow steel cylinder. The top of the heated copper cylinder is the boiling surface machined to 8x8 mm^2 and insulated using machinable ceramic (902 Alumina Silicate). The boiling surface was polished using sandpaper #1200/4000. The average surface roughness was 0.071 μm measured using Mitutoyo Surftest SJ-210. Two pieces of high transparent acrylic were used to confine the flow. Three 0.5 mm type-K thermocouples were used to measure the interior temperatures of the copper heater block. All thermocouples used in the current study were calibrated against class A- RTD. The temperature measurements were collected by using a Keithly DAQ model 2700. The heater block was heated by an induction heating coil connected to a 5 kW power supply (VERSAPOWER) with a maximum capacity of 200A/350V. The induction coil was cooled with chilled water to avoid damage by overheating. A PID controller was used to adjust the induction current that passes through the coil to maintain the surface temperature at a preset value.

2.3. Data Reduction

The surface heat flux, q_s'', was calculated using equation (2.1). The temperature measurements taken from the three thermocouples embedded in the heater block have been fitted using the second-order polynomial shown in equation (2.2). The heated surface temperature T_s was determined by extrapolation, equation (2.3). The temperature gradient at the surface was calculated from the temperature derivative calculated from equation (2.2). The surface heat flux, q_s'', was calculated using equation (2.4).

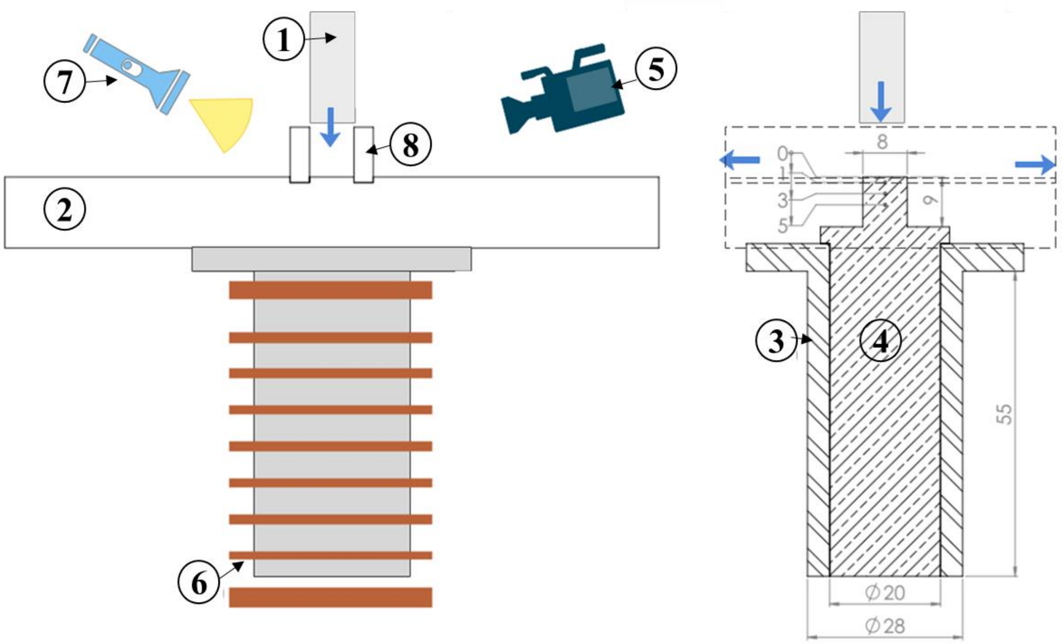

1: Round jet d=8 mm, 2: Ceramic insulation, 3: Steel cylinder, 4: Copper cylinder, 5: High-speed camera, 6: Induction coil, 7: light source, 8: Acrylic channel

Figure 2.2: The heater block design used to investigate the boiling curve under JIB.

$$q_s^{''}=k_{cu}\left.\frac{\partial T}{\partial y}\right|_{y=0} \tag{2.1}$$

$$T(y)=c_0y^2+c_1y+c_2 \tag{2.2}$$

$$T_s=\frac{1}{16}(6T_5-20T_3+30T_1) \tag{2.3}$$

$$q_s^{''}=\frac{-k_{cu}}{2}(T_5-3T_3+2T_1) \tag{2.4}$$

where T_5, T_3, and T_1 in equations (2.3) and (2.4) refer to the temperature measurements at locations y = 5 mm, y = 3 mm, and y = 1 mm measured from the heated surface (see Figure 2.2). The copper thermal conductivity (k_{cu}) is assumed constant value of 380 W/m.K.

2.4. Bubble Dynamics Measurements

2.4.1. High-Speed Imaging

A high-speed camera (Photron FASTCAM model 100K) was used to capture the bubble dynamics with a sampling rate of 10,000 frames per second. In each experiment, the bubble departure diameter (BDD) was calculated as the average of one hundred bubbles chosen randomly. The method of bubble diameter measurement is depicted in Figure 2.3. The measured bubble diameter at a certain frame was considered as the average of ten diameters with different interval angles [33,35] to reduce the measurement error due to the non-sphericity of the bubble. Before each experiment, the high-speed camera was validated using a spherical ball with a diameter of 1.5 mm. In the present study, a set of 55 experiments were carried out in the isolate bubble nucleate boiling regime with a total of

5,500 bubbles during the experimental conditions shown in Table 2.1. ImageJ software was used to analyze and determine the average BDD. The distribution of the measured bubble diameters was found almost normal in all cases, as shown in Figure 2.4 which agrees with the findings reported in [27,36,37].

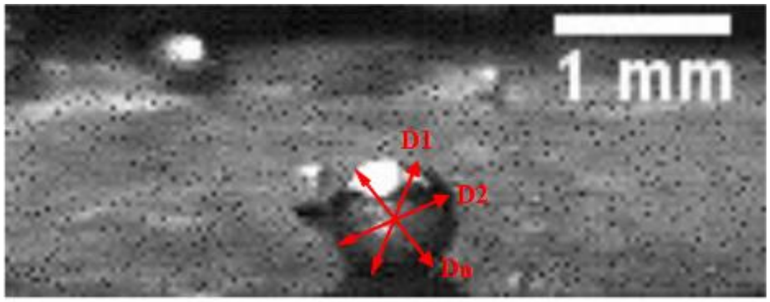

Figure 2.3: Measurement method of bubble diameter.

Table 2.1: Experimental matrix of the present study.

P_{sys} (KPa)	ΔT_{sup} ($°C$)	ΔT_{sub} ($°C$)	V_j (m/s)
101.3	12.6-33.7	11.7-37.6	0.2-0.8

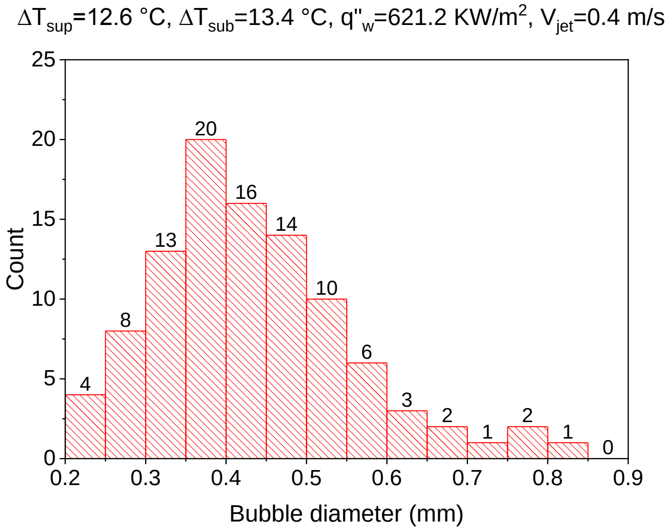

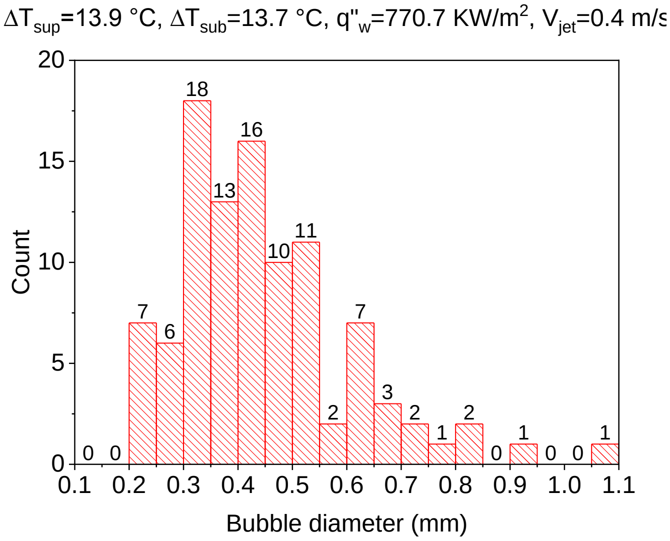

Figure 2.4: Typical frequency of measured bubbles.

2.4.2. Fiber Optic Probe

2.4.2.1. Fiber Optic System Description

Figure 2.5 shows the fiber optic system that was used to measure the vapor layer breakup frequency in the transition regime. It consists of a laser source, coupler, photodiode, glass fiber cable, glycerin, and PC. A laser source (ILX Lightwave MPS-8033) was used to transmit a laser beam to a beam splitter (single mode 2x2 coupler) that requires 50 % of the light intensity to be transmitted to the fiber probe tip and the remaining 50 % is dissipated into glycerin[36]. The current study used a single-mode fiber cable (THORLABS-P1-SMF28Y-FC) with a core diameter of 10.5 microns that is surrounded by a cladding material with a diameter of 125 microns. When the fiber tip is exposed to a medium of high refractive index (i.e., water) the beam is reflected back into the fiber with low intensity and vice versa when the tip is in contact with low refractive index (vapor). The light reflected in the fiber is converted into a voltage signal by a photodiode (THORLABS- PDA10CS) which is equipped with an amplifier. Hence, the signal voltage of the optic probe is high when the tip is in contact with vapor and low when it touches a liquid.

Before using the fiber-optic probe to distinguish between the two phases, the probe was etched chemically using Hydrofluoric acid (HF-48 %) to reduce the tip diameter to enhance the strength of the collected signal and reduce the interference with the liquid-vapor interface. The etching process reported in Ahmed and Hamed [9] was adopted in the present study, as shown in Figure 2.6.

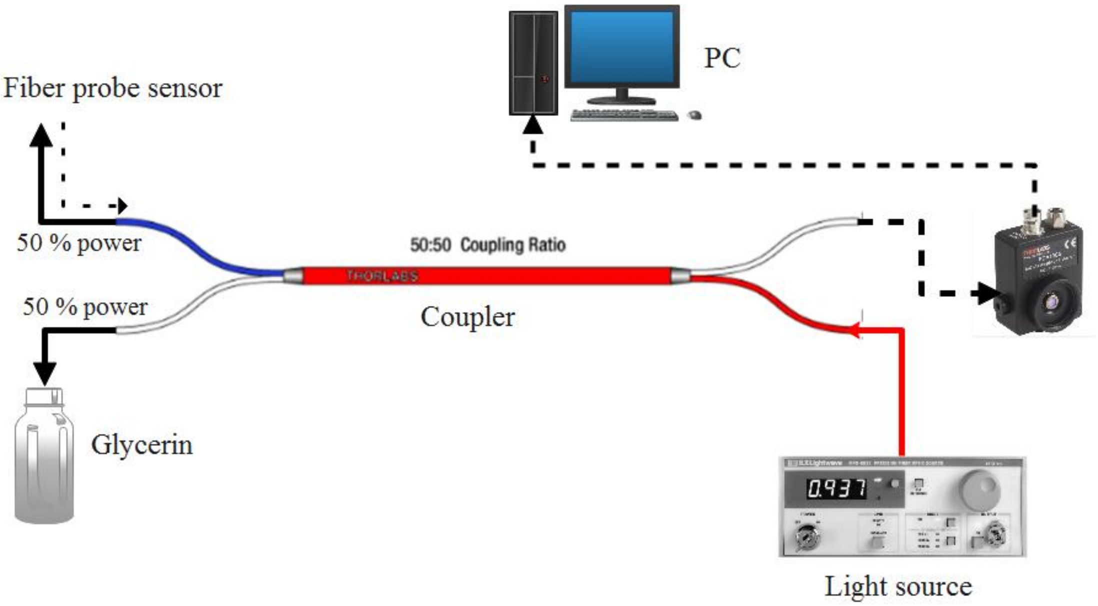

Figure 2.5: Fiber optic probe system.

2.4.2.2. Fiber Optic Sensor Validation

Two tests were carried out to calibrate the fiber optic system in which air bubbles were released from a small diameter needle in a water pool, as depicted in Figure 2.7. The frequency of the released bubbles was measured by the optic probe. It is defined as the number of signal spikes (peaks) divided by the sampling time then calibrated against the one measured by a high-speed camera which is defined as the number of bubbles captured in frames divided by the sampling time. Table 2.2 shows a comparison between the frequency obtained by fiber-optic and the one obtained from processing the images of the high-speed camera for two different flows of bubbles. The results show a good agreement between the two measurement techniques. Actual pictures of the two tests are shown in Figure 2.8

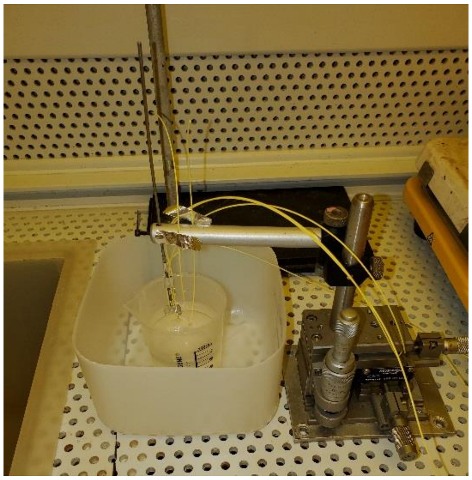

Figure 2.6: Etching process of fiber optic.

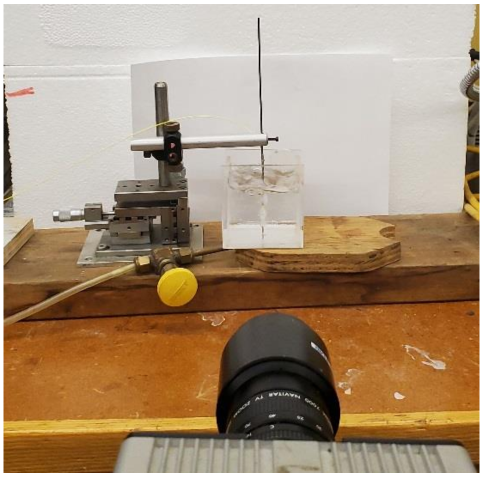

Figure 2.7: Fiber optic calibration.

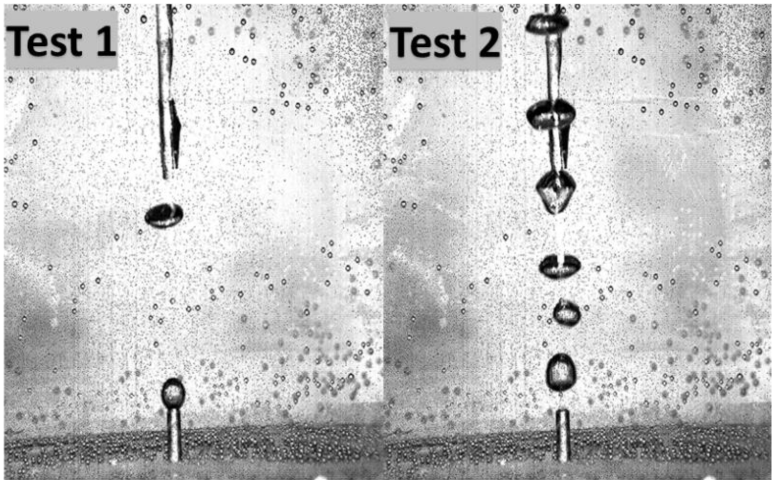

Figure 2.8: Actual image of calibration test.

Table 2.2: Results of fiber optic calibration.

Technique	Frequency (Hz) in Test 1	Frequency (Hz) in Test 2
Fiber-optic probe	11.50	37.6
High-speed camera	11.56	37.03
Relative error %	0.54	-1.53

2.4.2.3. Probe Signal Processing

At each wall temperature, the probe was used to collect ten samples with a rate of 250 K sample/sec for a recording time of 5 Sec. Then, the raw data were processed to estimate the average vapor layer break-up frequency. The signal processing procedures are shown in Figure 2.9. First, the raw signal was smoothed to eliminate any noise. Then a MATLAB signal processing tool was used to estimate the low and high levels of the raw signal. A threshold voltage V_{thresh} was required to distinguish between the signal that had an intermediate voltage value between the high voltage signal V_H and low voltage signal V_L. The threshold voltage was estimated as $V_{thresh} = V_L + 0.15(V_H - V_L)$ as recommend by [36].The voltage of raw signal above the threshold value was considered as vapor and the value below the threshold was considered as liquid. Based on this definition, the fluid phase function (FPF) and vapor contact frequency are obtained by equation 2.5 and equation 2.6, respectively. Figure 2.10 illustrates an example of the raw signal data and the obtained FPF of calibration test 2. As shown clearly, the threshold value of 0.1 (v) obtained by the equation of V_{thresh} could distinguish between the two phases.

Fluid Phase Function (FPF) is defined as

$$FPF(y,t) = \begin{cases} 0 & \text{for liquid} \\ 1 & \text{for Vapor} \end{cases} \tag{2.1}$$

Vapor contact frequency is calculated according to

$$f = \frac{N}{t_s} = \frac{Number\ of\ peaks}{sampling\ time} \tag{2.2}$$

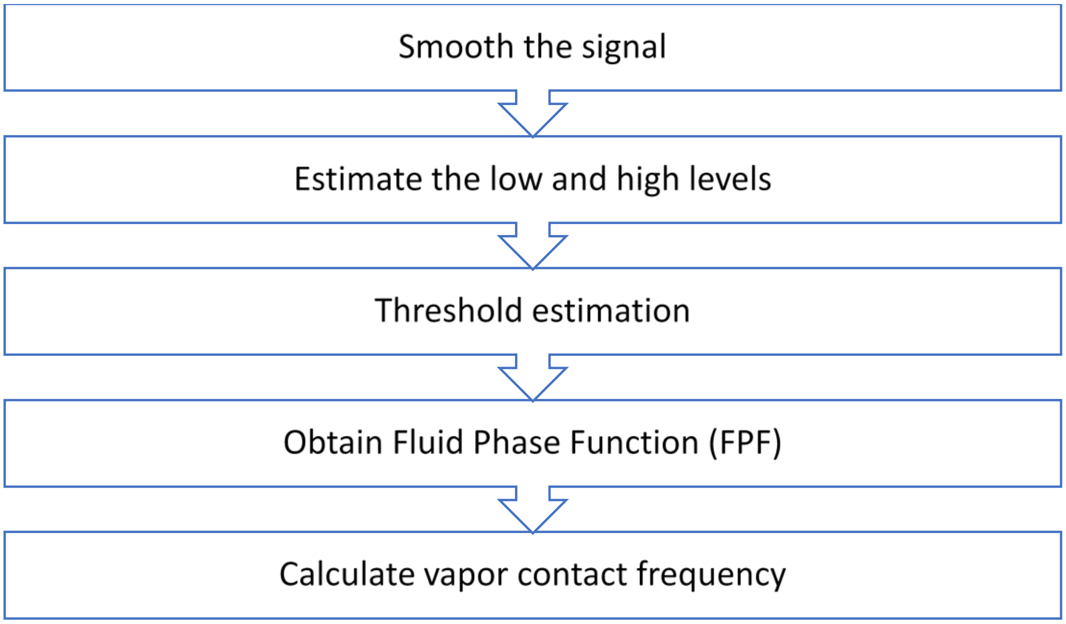

Figure 2.9: Procedures of signal processing of the optic probe raw signal.

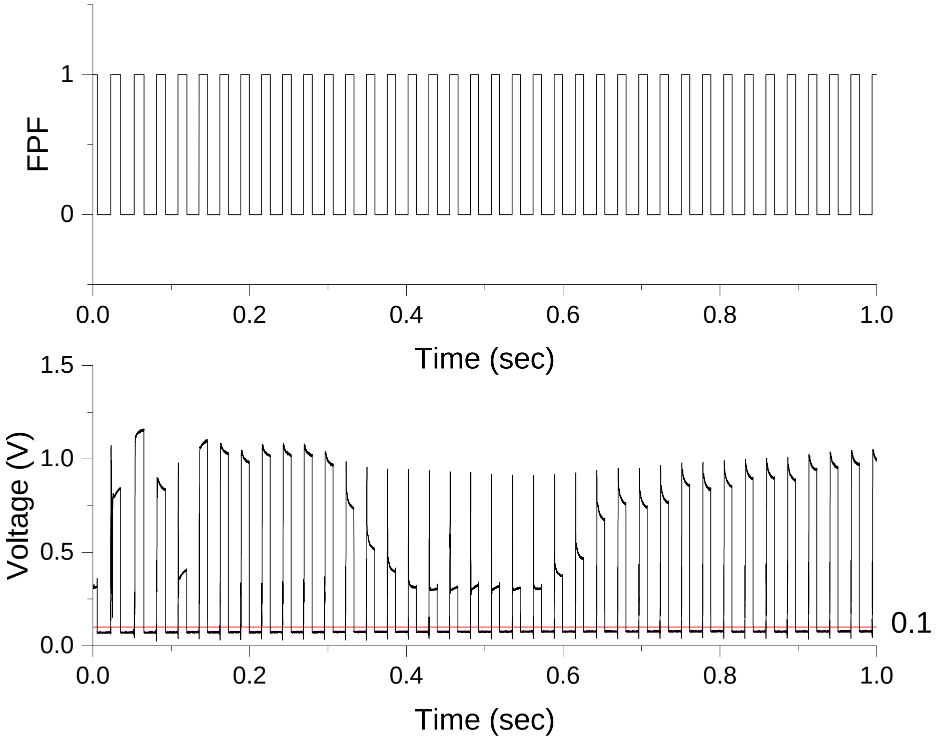

Figure 2.10: Raw signal of the fiber probe and FPF in calibration test 2.

2.5. Analysis of Heat Losses

As mentioned earlier, the steady-state of the temperature readings inside the copper cylinder were used to estimate the temperature and heat flux at the boiling surface. The measurements were taken at the block center and the temperature distribution inside the block was assumed uniform. Although the sidewall was insulated by ceramic, one can not assure that the sidewall losses can not affect the temperature distribution in the direction normal to the jet flow (x-direction), especially at an extensive cooling rate. In this section, numerical simulation using COMSOL-Multiphysics software was carried out to estimate how significant the sidewall losses were compared to the surface heat flux. Figure 2.11

shows the computational domain of one-half of the heater block. The heater block consists of a copper cylinder fitted inside a hollow steel cylinder which was heated by an induction coil.

COMSOL Multiphysics solves the electromagnetic field coupled with induction heating inside the heater block. The boundary conditions were defined as follows. The left boundary was defined as symmetric surface (adiabatic). The boiling surface was exposed to a cooling rate of 9.7 MW/m^2, corresponding to a jet velocity of 1 m/s and a subcooling of 49 °C. The heat loss from sidewalls is unknown. The remaining boundaries were assumed to lose heat by radiation. An induction coil heated the heater block with an induction power of 2.09 KW and a frequency of 30.2 kHz.

The sidewall losses were estimated by solving the inverse heat conduction problem [22,37] by minimizing the error between the predicted temperatures T(0,z) at z= 63 mm, 65 mm, and 67 mm and the corresponding measurements at the locations 5 mm, 3 mm, and 1 mm, respectively below the boiling surface. Figure 2.12 shows a comparison of the numerical results and experimental data at the center of the copper block (x=0). The predicted temperatures agree well with the measurements with a maximum relative error of 4.3 %. The relative absolute error between the surface temperature obtained from equation (2.3) and the numerical simulation is 3 %. The sidewall heat loss ($q^{"}_{losses}$) was estimated as 2.6 MW/m^2 which represents 12.9 % of the heat source ($q^{"}_{heat\ source}$= 20.13 MW/m^2). The sidewall loss caused the interior temperatures to vary within 10 °C, as shown in Figure 2.13.

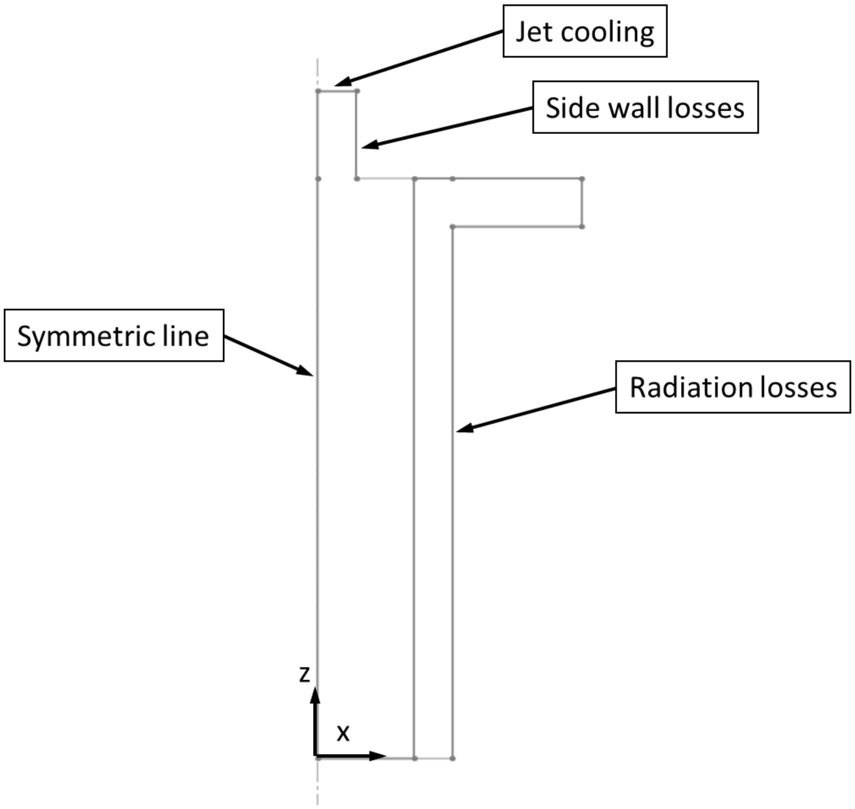

Figure 2.11: Computational domain of the heater block.

This variation has an insignificant effect on the present results either in the nucleate regime or the transition regime since all measurements were collected around the position x=0. The temperature distribution and internal heat generation inside the heater block are shown in Figure 2.14 and Figure 2.15, respectively. The average heat generation in the copper cylinder was 2.37E5 W/m^3, the steel cylinder was 5.47E07 W/m^3, and the small copper part was 1.67E4 W/m^3. The induction heating technique generated almost a uniform heat generation inside the copper piece. However, the heat generation inside the steel part was significant compared to that in the copper because of the skin effect that always exists in induction heating where the current density is high at the outer surface[20].

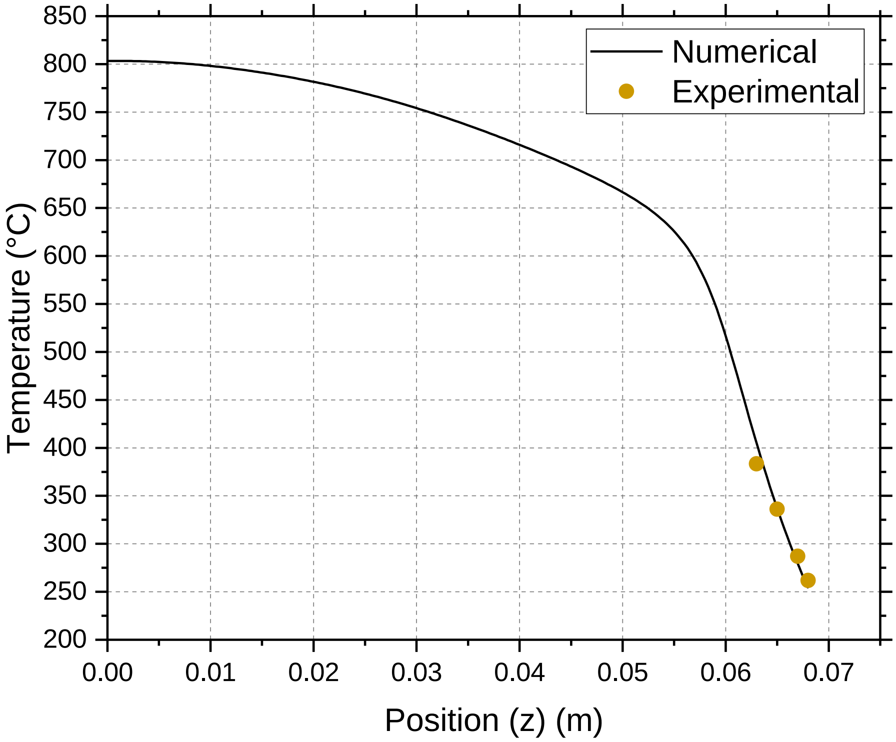

Figure 2.12: Comparison of predicted and measured temperatures inside the heater block at $\Delta T_{sub} = 49$ °C, V_{jet}= 1 m/s.

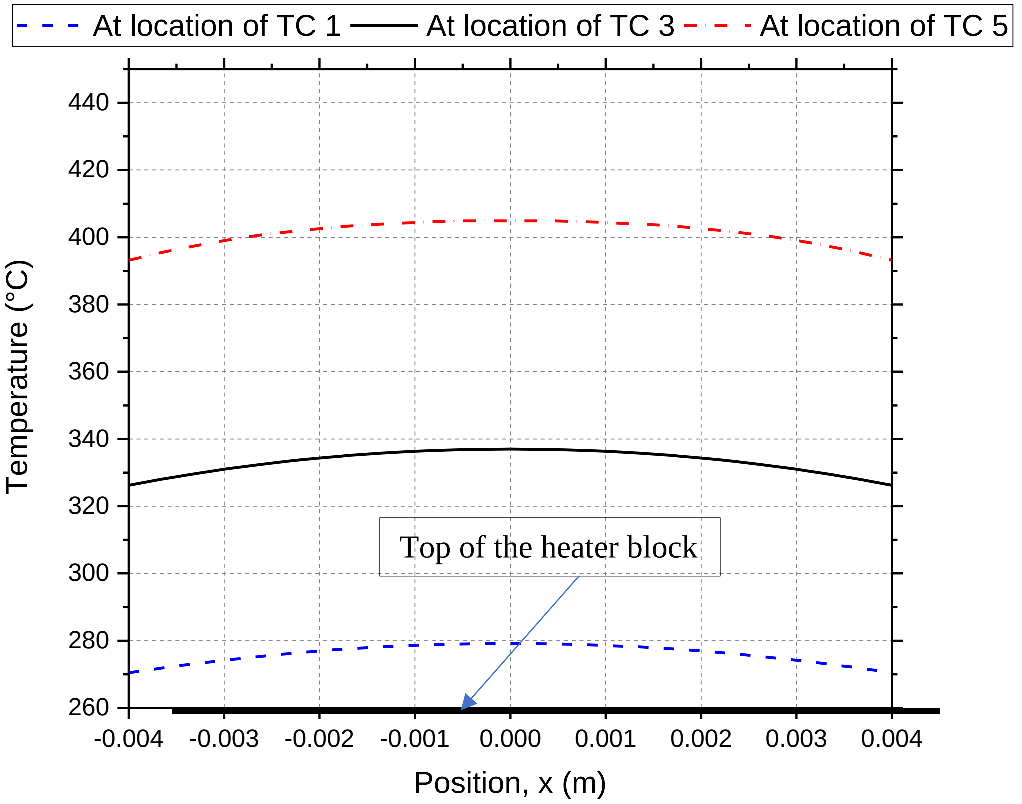

Figure 2.13: Interior temperature of the copper block at $\Delta T_{sub} = 49$ °C, V_{jet}= 1 m/s.

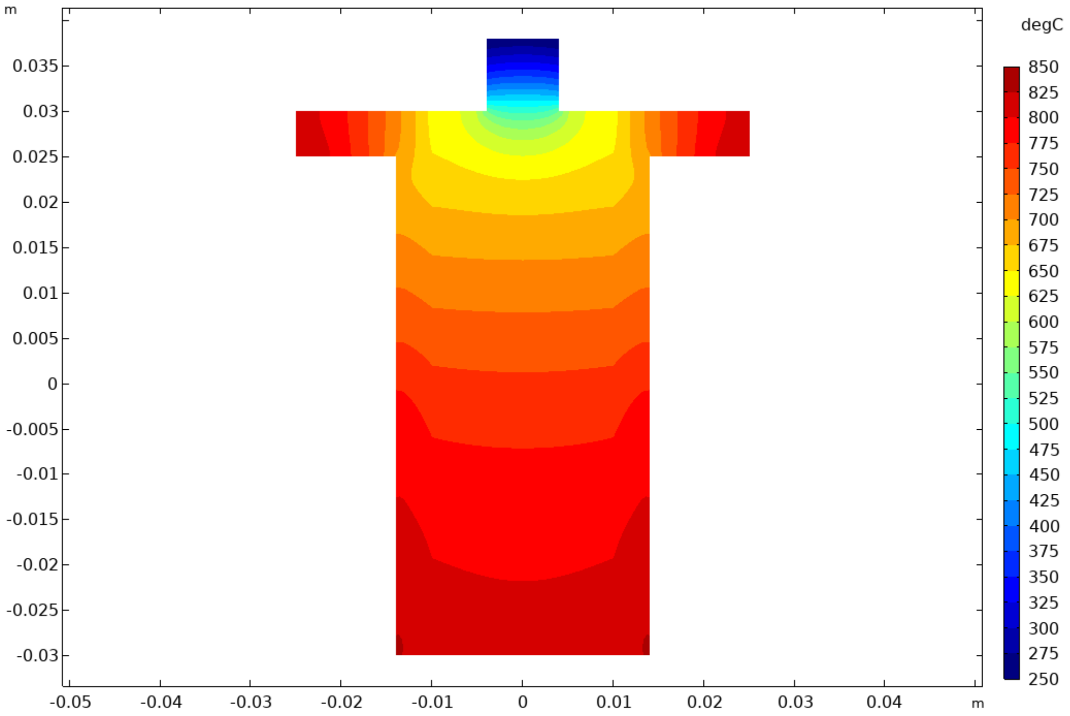

Figure 2.14: Temperature contours inside the heater block.

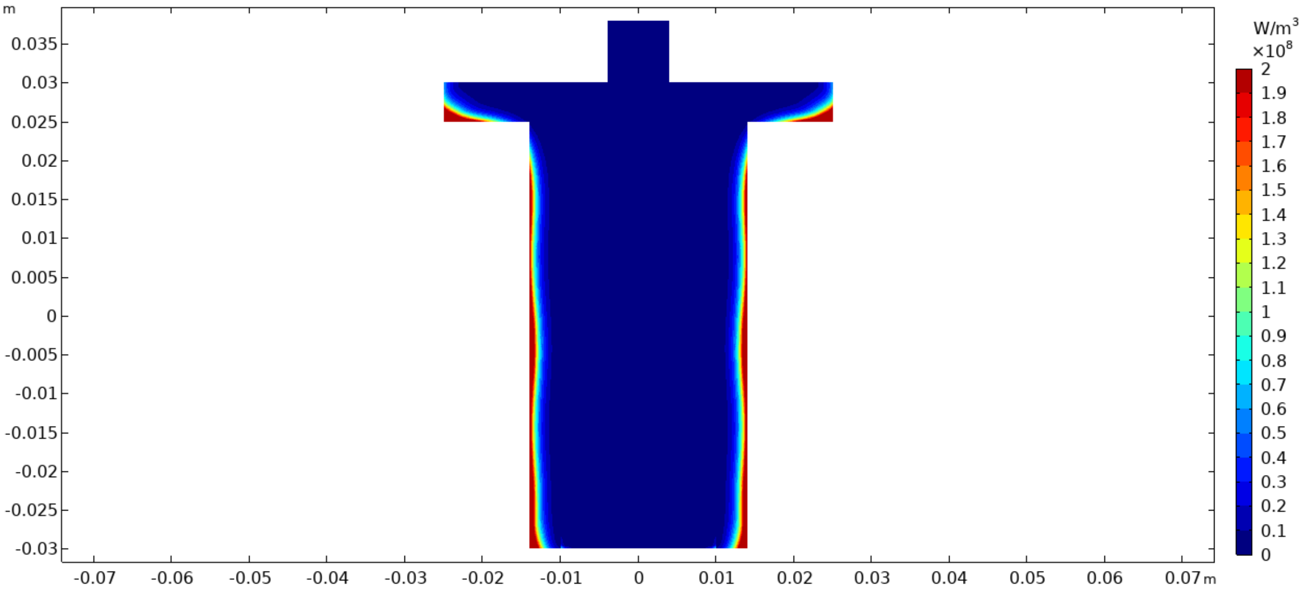

Figure 2.15: Distribution of the internal heat generation.

2.6. Experimental Procedure

During each experiment, the water was heated in the tank using a thermostatic control immersion heater to a temperature slightly higher than the desired fluid temperature to compensate for the heat loss in the piping system. After the water reached a steady state, the pump was turned on and the flow rate was adjusted manually to the desired jet velocity using a control valve. The surface was carefully taken care of before each experiment to maintain the initial conditions. It was cleaned using a commercial rust removal and a cotton swab to remove any oxidation layer or any residuals from the previous test. The induction heating system was turned on as soon as the jet velocity and fluid temperature reached a steady-state condition. The induction coil was connected to a control unit with a PID controller adjusted to autotune mode. The PID controls the power delivered to the induction coil to achieve the set point. The jet velocity, water temperature, and interior temperatures were recorded when a steady state was reached. It was considered a steady state when the maximum variation in temperature readings of the three thermocouples inside the copper block was less than 1 ºC. Besides the above procedures in studying bubble dynamics, before turning the heater on, a 1.5 mm small steel ball was rested in the middle of the boiling surface to calibrate the high-speed camera. Before collecting the data of the vapor layer breakup frequency, a static test was carried out. The probe was dipped into a water pool multiple times to verify the output voltage of the probe that should be high in the air and low in the water. If the signal was degraded and no distinction between the two phases, the fiber probe was chemically etched and then cleaved.

2.7. Summary of Measurements

The following points summarize the measurements in the current work

- Investigation of the boiling curve at high operation conditions:
    - The surface temperature was calculated from the extrapolation of the measurements of interior temperature.
    - The wall heat flux was calculated from the gradient of the temperature profile at the boiling surface.
- Bubble dynamics in nucleate boiling regime:
    - High-speed images were recorded then bubble departure diameter (BDD) was obtained from image processing.
- The vapor break-up frequency in the transition boiling regime:
    - The vapor breakup frequency was measured using fiber optic probe and high-speed camera was used to capture Rayleigh-Taylor instability.

3. Chapter 3: Experimental Investigation of the Jet Impingement Boiling Curve

This section presents the results of the experiments that have been carried out at steady-state conditions. The effects of jet velocity and liquid subcooling on the boiling curve are discussed in sections 1 and 2, respectively. To verify the reliability of the current experimental facility, the boiling curve produced from the current experimental setup was compared with the boiling curves reported in the literature in [6,9] considering almost the same operating conditions, boiling surface area, and jet dimensions. Figure 3.1 shows a comparison of the boiling curve obtained from the current work and the boiling curves reported in the literature[6,9]. The current results were in a good agreement with the boiling curves reported in previous works. Moreover, the values of the CHF and the shoulder heat flux were comparable.

However, the current boiling curve did not exhibit the drop first minimum observed before the shoulder heat flux reported in [6,9]. The current boiling curve showed the transition from the CHF to the film boiling in two stages. The first stage represents a plateau of the heat flux. In the second stage, the heat flux decreased with increasing the surface temperature. Recalling the conclusion of reviewing the work that has been carried out on MEB in section 1.2.1.1 0, the behavior of the boiling curve after the CHF is affected by many parameters such as flow velocity, subcooling, surface conditions, heater dimensions, etc. The current setup has the same boiling surface area, planar jet dimensions, surface

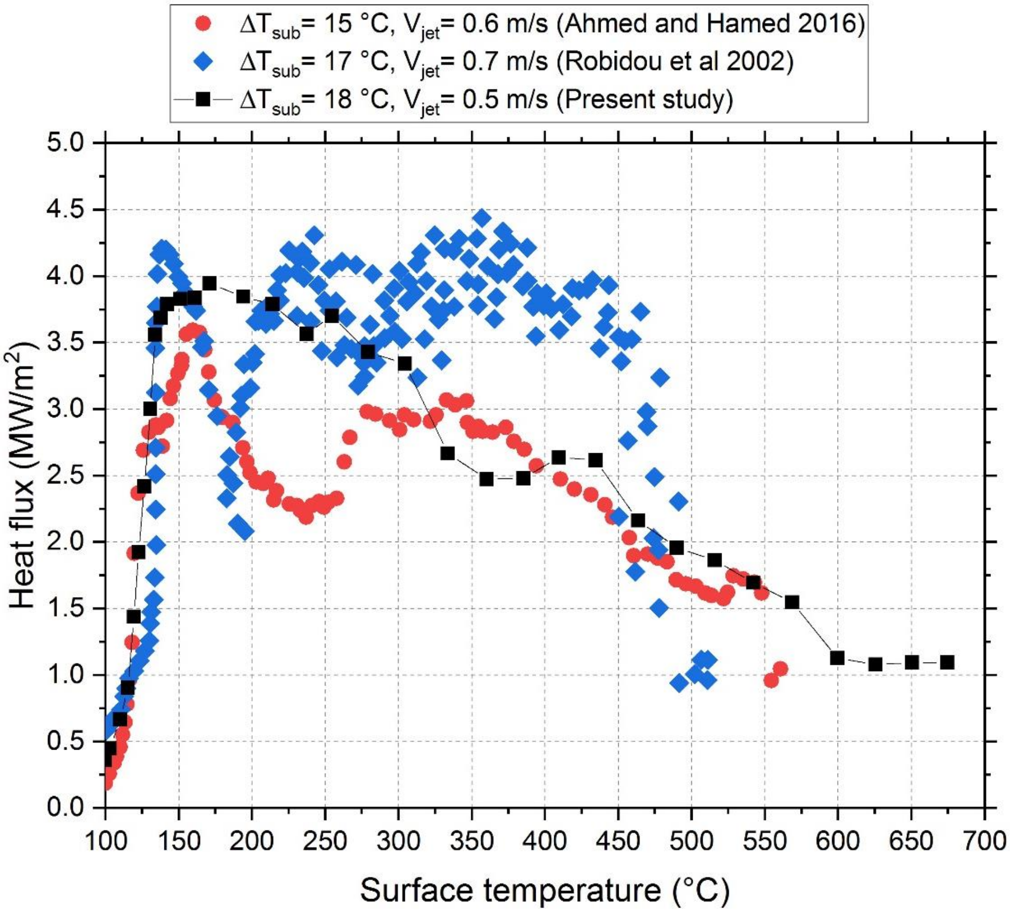

Figure 3.1: Comparison of the current boiling curve and boiling curves reported in [6,9].

finish, and surface material. The disappearance of the first minimum in the boiling curve obtained in the current study might be attributed to the high heating rate provided by the induction heating system and the relative bigger mass of the heater block compared to that reported in previous works. This made the response time of the current setup faster than that in the literature. Hence, the boiling surface obtained sufficient heat to sustain the vapor generation, which increased the vapor layer instability, preventing heat flux drop after the CHF.

It is interesting to note here that in the study carried out by Estes and Mudawar[55], they compared the performance of a free jet and spray cooling. They observed that the occurrence of the CHF was affected by the rate of heat supplied to the boiling surface, which supports the current hypothesis that the faster rate of heating supplied by the current induction system might affect the boiling curve around the CHF and the first minimum.

3.1. Effect of Jet Velocity

Figure 3.2 shows the effect of changing the jet velocity from 0.5 m/s to 3.8 m/s on the JIB curve. It can be noticed that the effect of jet velocity on the nucleate heat transfer was insignificant. Yet, the value of the CHF increased noticeably by increasing jet velocity. The high jet momentum breaks the vapor layer that covers the surface and prevents the liquid from wetting the hot surface, causing a decrease in heat transfer rate. The CHF increased from 4.4 MW/m^2 to 8.46 MW/m^2 when the jet velocity increased from 1 m/s to 3.8 m/s. Figure 3.3 shows the change in the CHF with jet velocity and compares the measured CHF with the predicted CHF using the correlation developed by Monde and Katto[56], equation (3.1) and the correlation developed by Lee et al. [57], equation (3.2). The measured CHF was within the predicted values obtained from the correlations developed by [56,57] at the same experimental conditions. However, the CHF in the current work was proportional to $V_j^{0.5}$ while the CHF in [56] and [57] is proportional to $V_j^{1/3}$ and $V_j^{0.27}$, respectively.

$$\frac{q''_{CHF}}{\rho_v h_{fg} V_j} = 0.0745 \left(\frac{\rho_l}{\rho_v}\right)^{0.725} \left(\frac{\sigma}{\rho_l V_j^2 D}\right)^{\frac{1}{3}} \left[1 + 2.7 \left(\frac{\rho_l}{\rho_v}\right)^{0.5} \left(\frac{c_{p,l} \Delta T_{sub}}{h_{fg}}\right)^{2.0}\right] \tag{3.1}$$

$$\frac{q''_{CHF}}{\rho_v h_{fg} V_j} = 0.0956 \left(\frac{\rho_l}{\rho_v}\right)^{0.761} \left(\frac{\sigma}{\rho_l V_j^2 D}\right)^{0.365} \left[1 + 0.952 \left(\frac{\rho_l}{\rho_v}\right)^{0.118} \left(\frac{c_{p,l} \Delta T_{sub}}{h_{fg}}\right)^{1.414}\right] \tag{3.2}$$

In the transition regime, the shoulder phenomena existed in all cases. This phenomenon was attributed to the breakup and formation of vapor pockets on the heated surface. The breakup of large bubbles into micro bubbles enhanced fluid mixing, hence increasing the wettability of the surface. The value of the shoulder heat flux is comparable to the CHF for all operating conditions and increases with the jet velocity.

3.2. Effect of Liquid Subcooling

The effect of liquid subcooling on the boiling curve at a jet velocity of 1 m/s is depicted in Figure 3.4. In general, the liquid subcooling did not affect the nucleate boiling regime. Yet, the effect was significant on the value of the CHF and the value of the shoulder heat flux, even with a small increase in the degree of subcooling. The CHF increased from 4.4 MW/m^2 to 6.0 MW/m^2 when the subcooling increased from 12 ºC to 22 ºC. It is worth noting that the shoulder heat flux increased above the value of the CHF at degrees of subcooling higher than 12 ºC.

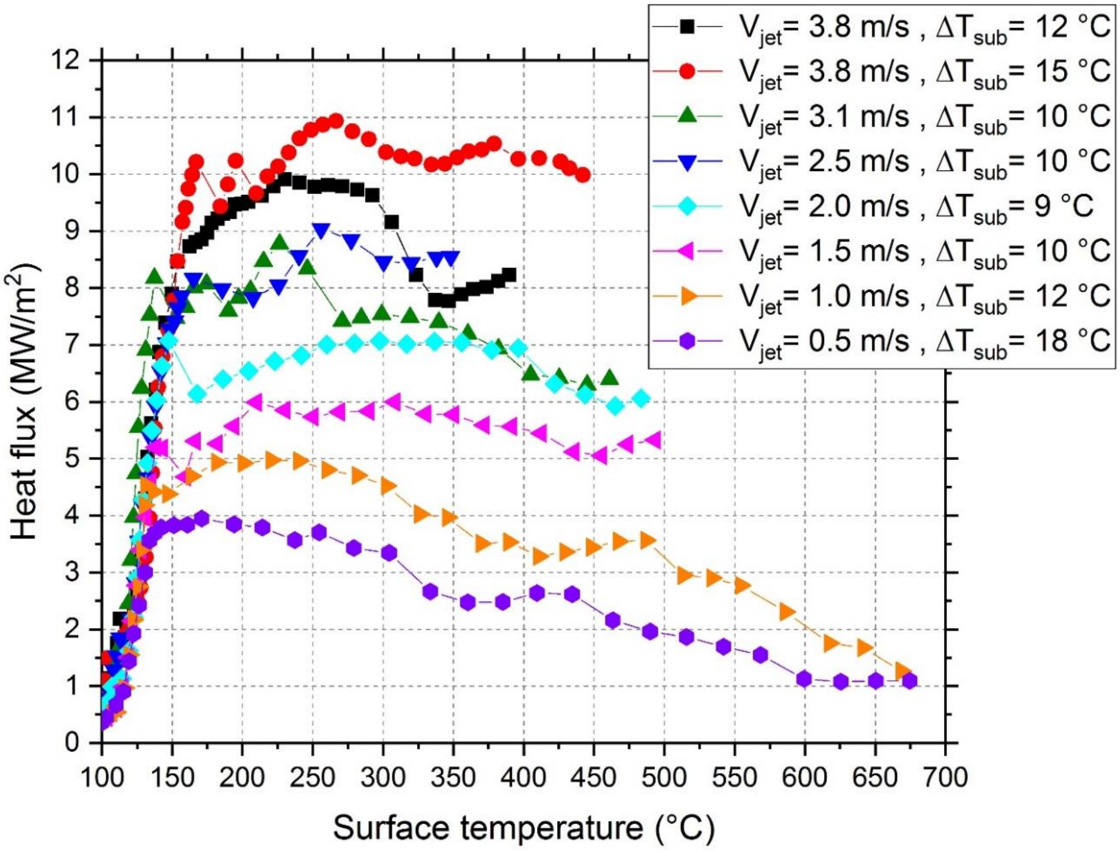

Figure 3.2: Effect of jet velocity on the boiling curve.

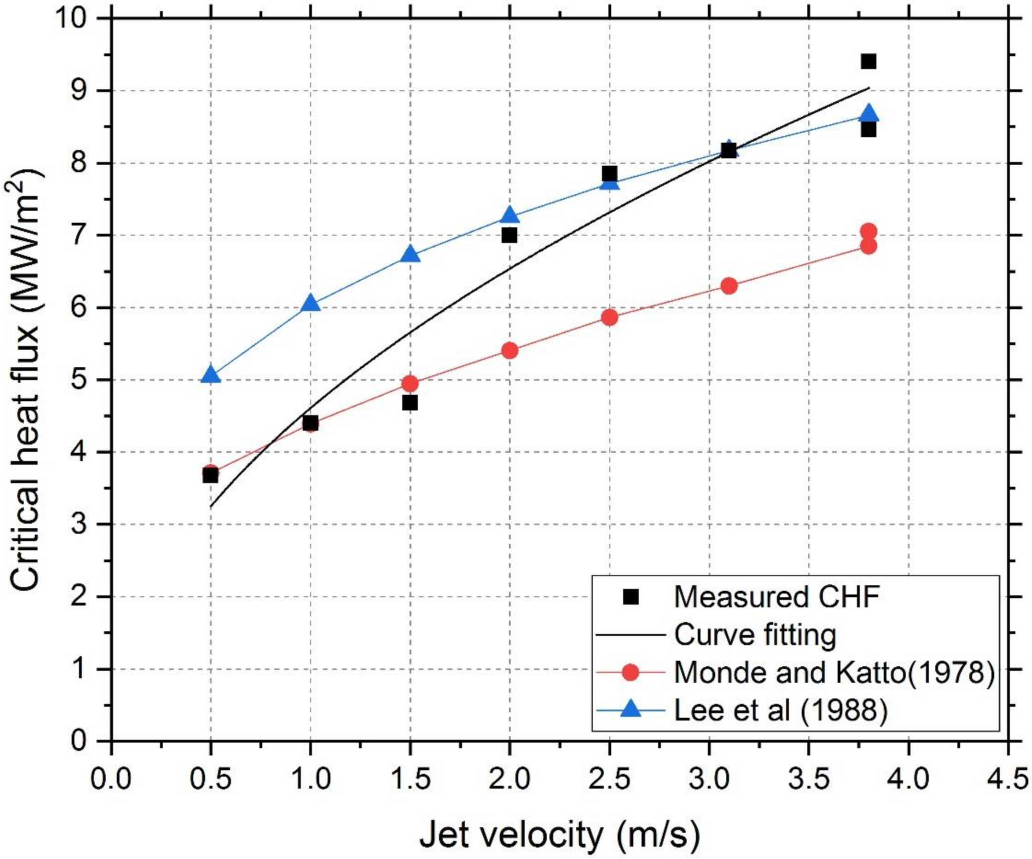

Figure 3.3: Variation of the critical heat flux with jet velocity.

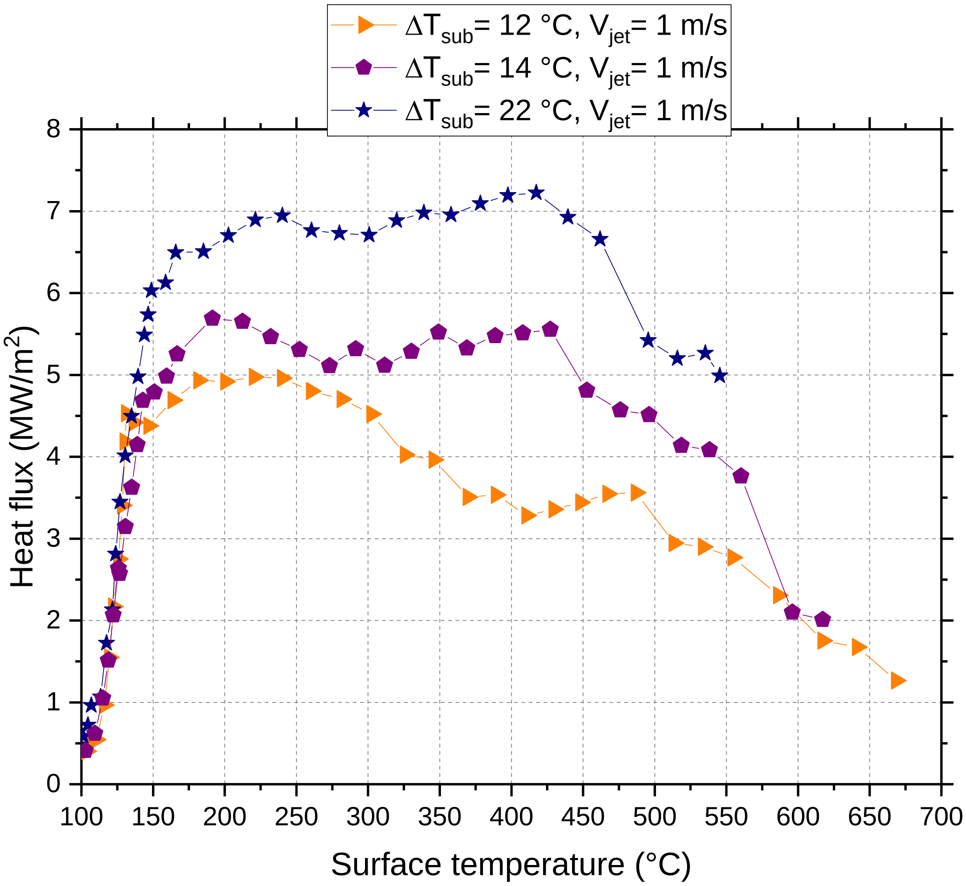

Figure 3.4: Effect of subcooling on the boiling curve.

4. Chapter 4: Experimental and Numerical Investigation of Bubble Dynamics within The Nucleate Boiling Regime

4.1. Mechanistic Model Description

This section describes the calculation methodology of BDD and bubble growth rate within the nucleate boiling regime. The bubble growth rate was determined by applying the energy balance for the growing bubble. The bubble departure diameter, BDD, was determined from the force balance. Figure 4.1 shows all forces acting on a growing bubble located within the stagnation zone of an impinging jet [37]. The BDD is defined as the bubble diameter at which the force balance in the vertical direction, presented here in equation (4.1), is violated. The growing bubble within the stagnation zone is subjected to the following forces : (1) the surface tension force,F_σ, (2) the buoyancy force, F_b, (3) the contact pressure force, due to pressure distribution at the bubble interface, (4) the hydrodynamic pressure force, F_h, due to jet momentum, and (5) the unsteady drag force, F_{du}, due to bubble growth. The different expressions used to determine these forces are presented in Table 4.1.

$$\sum \mathrm{F_y} = \mathrm{F_{\sigma y}} + \mathrm{F_b} + \mathrm{F_{cp}} + \mathrm{F_h} + \mathrm{F_{du}} \tag{4.1}$$

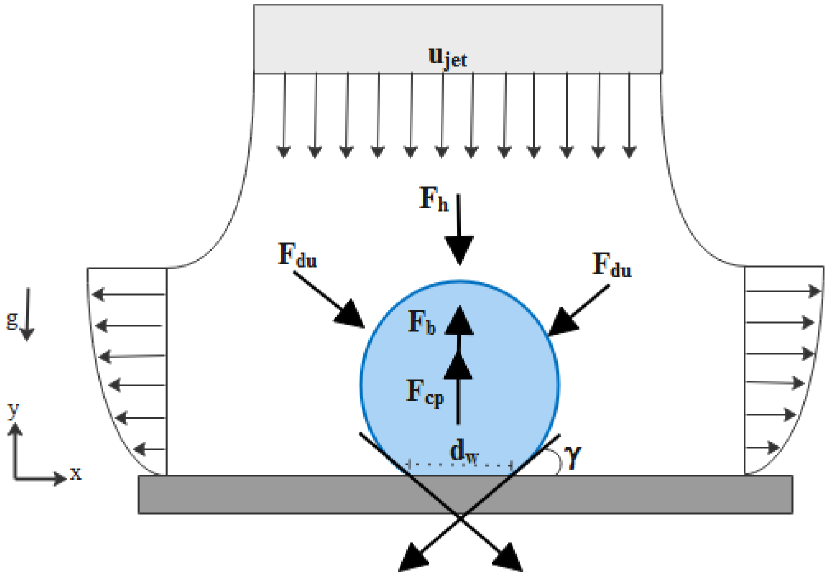

Figure 4.1: Forces acting on a growing bubble located within the stagnation zone of an impinging jet.

Expressions listed in Table 4.1 indicate that the force balance approach strongly depends on the accurate determination of the instantaneous bubble diameter and the bubble growth rate. Bubble growth is governed by the heat balance experienced by the growing bubble. Figure 4.2 shows the three important heat transfer mechanisms that affect a growing bubble located on the heated surface. A growing bubble gains heat from the superheated liquid layer adjacent to the heated surface and the evaporation of the liquid microlayer underneath the bubble. Furthermore, the growing bubble could lose heat from its top side if subjected to the subcooled liquid.

Table 4.1: Expressions used to determine various forces included in equation 4.1 [37].

Force	Equation
Surface tension force	$F_{\sigma y} = -2\pi d_w \sigma \sin(\gamma)$
Buoyancy force	$F_b = \frac{4}{3}\pi R_b^3(\rho_l - \rho_v)g$
Hydrodynamic pressure force	$F_h = -0.5\,\rho_l V_j^2 \frac{\pi d_w^2}{4}$
Contact pressure force	$F_{cp} = \frac{2\sigma}{5R_b}\frac{\pi d_w^2}{4}$
Unsteady drag force due to bubble growth	$F_{du} = -\rho_l \pi R_b^2 \left(\frac{3}{2}\dot{R}_b^2 + R_b\ddot{R}_B + 2V_j\dot{R}_b\right)$

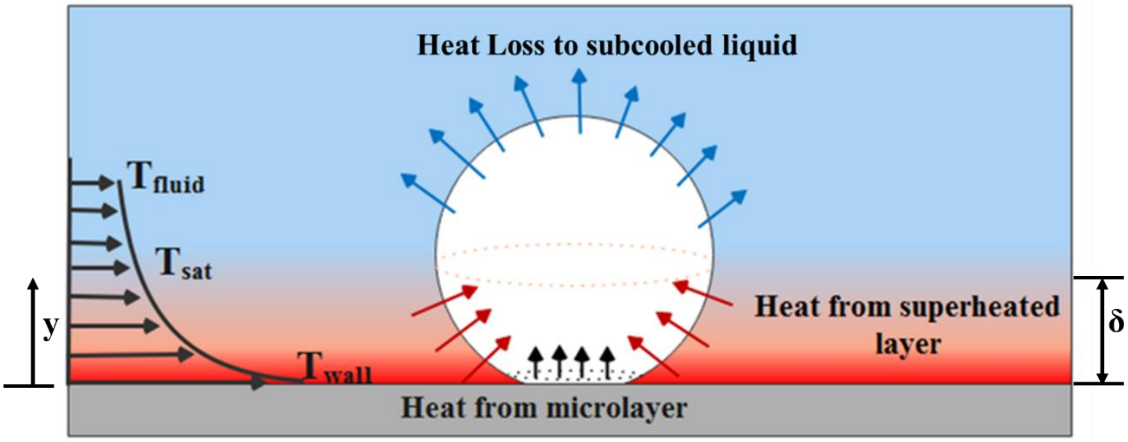

Figure 4.2: Heat transfer mechanisms involved in the bubble growth process.

The current study adopted the bubble growth model developed by Colombo and Fairweather [44] expressed here in equation (4.2). The first term represents the rate of growth due to heat transferred from the thermal boundary layer to the growing bubble. The second term represents the rate of growth due to heat transferred from the microlayer to the growing bubble. The last term represents a negative rate of bubble growth due to heat lost to the subcooled liquid.

$$R(t) = 2\sqrt{\frac{3}{\pi}}k_l\left(T_{sup} - T_l\right)\sqrt{\frac{t}{\alpha}} \times (1-\chi) + \frac{2}{C}Ja\,Pr^{-0.5}\sqrt{\alpha t} - \frac{h_c}{\rho_v h_{fg}}(T_{sat} - T_l) \times \chi \tag{4.2}$$

Where C is an empirical constant, χ is the part of the bubble surface area exposed to the subcooled liquid which was calculated using equation (4.3).

$$\chi = 1 - \frac{y_{sat}}{2R_b} \tag{4.3}$$

Where R_b is the instantaneous bubble radius and y_{sat} is the distance from the wall at which the temperature reached the saturation temperature of the liquid [45]. y_{sat} was calculated from the temperature distribution within a turbulent boundary layer proposed by Kader [58], equation (4.4).

$$\frac{T_w - T}{T_\tau} = Pry^+ \exp(-\Gamma) + \left\{2.12\, ln\left[\frac{2.5(1+y^+)\left(2-\frac{y}{\delta}\right)}{1+4\left(1-\frac{y}{\delta}\right)^2}\right] + \beta(Pr)\right\} \exp\left(-\frac{1}{\Gamma}\right) \tag{4.4}$$

Where $y^+ = \frac{yu_\tau}{\nu}$, $\Gamma = \frac{0.01(Pry^+)^4}{1+5Pr^3y^+}$, $\beta(\mathrm{Pr}) = (3.85Pr^{\frac{1}{3}} - 1.3)^2 + 2.12\ln(Pr)$, $T_\tau = \frac{q_w^{"}}{\rho c_p u_\tau}$, u_τ is the frictional velocity and T_τ is the frictional temperature

To solve equation (4.4) for (y, δ), two boundary conditions are applied: (1) $T = T_{fluid}$ at y = δ and (2) $T = T_{sat}$ at y= y_{sat}.

The condensation heat transfer coefficient h_c in equation (4.2) is calculated from the correlation developed by Unal[27] given here in equation (4.5).

$$h_c = \frac{65\Phi h_{fg}R}{1/\rho_v - 1/\rho_l} \tag{4.5}$$

Where $\Phi = \begin{cases} (\frac{V_j}{0.61})^{0.47} & \text{for } V_j > 0.61 \text{ m/s} \\ 1 & \text{for } V_j \leq 0.61 \text{ m/s} \end{cases}$

Figure 4.3 shows the flowchart for the calculation of the BDD and the bubble growth rate. The model results have been validated using the current experimental data obtained for isolated bubbles observed with the nucleate boiling regime.

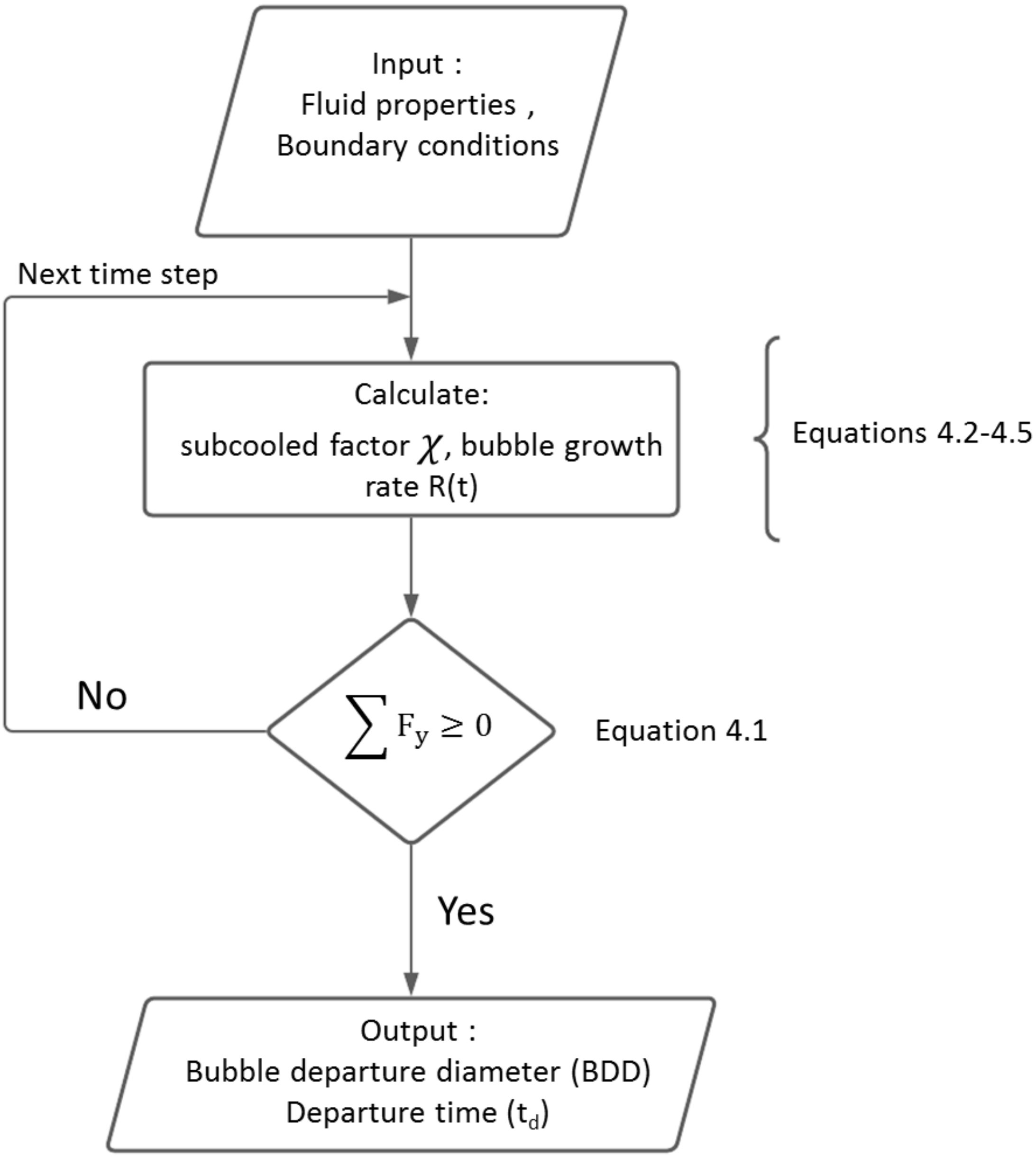

Figure 4.3: Flowchart of the calculation procedure of the BDD and the bubble growth rate.

4.2. Empirical Modeling of BDD

Figure 4.4 shows the change in the measured BDD with the degree of superheat at different flow conditions, i.e., different jet velocities and degrees of subcooling. The experimental results are categorized into four levels of velocities (0.2, 0.4, 0.6, and 0.8 m/s) and three degrees of subcooling, low (12.7 ºC - 16.3 ºC), medium (21.1 ºC - 24.1 ºC), and high (36.3 ºC - 37.4 ºC).

One can observe the general trend of the increase in the BDD with the increase in the surface temperature (or the surface heat flux). At jet velocity of 0.2 m/s, increasing the surface superheat by about 18 % resulted in an increase in the BDD by about 30 %. At jet velocity of 0.8 m/s, increasing the surface superheat by 15% resulted in an increase in the BDD by about 45%. This could be explained in the context of the energy balance on a growing bubble. When the surface temperature or the surface heat flux is increased, the superheated layer thickness adjacent to the heated surface increases; hence the amount of heat transferred to the growing bubble increases, yielding a bigger departing bubble. The experimental results reported by Levin and Khan [34] showed the thickness of the superheated layer increased with the increase in wall heat flux.

Among the current experimental range, it can be noticed that relatively larger BDDs are observed at the low degree of subcooling (12.7 ºC - 16.3 ºC) and small BDDs are observed at the high degree of subcooling (36.3 ºC - 37.4 ºC). The reduction in bubble size at a relatively higher degree of subcooling is attributed to the fact that colder fluid reduces the superheated layer thickness and increases the heat loss by condensation from the bubble top side. Furthermore, increasing the degree of subcooling at the same jet velocity resulted in a delay in the onset of the bubble nucleation until relatively higher surface temperatures. The onset of nucleation surface temperature increased by 8 ºC when the degree of subcooling was increased by 10 ºC, as shown in Figure 4.5.

Since increasing the jet velocity produces more momentum resulting in a thinner boundary layer, one can expect that the BDDs would decrease with increasing jet velocity. The effect of jet velocity on the BDD has been noticeably observed only at the high level of subcooling, as shown in Figure 4.6. The BDD decreased from about 0.496 mm to 0.3 mm when the jet velocity increased from 0.2 m/s to 0.8 m/s. The reduction in the BDD with the jet velocity could be explained as (1) increasing jet velocity producing more momentum that reduces the superheated layer thickness, (2) increasing the jet velocity enhanced the rate of condensation heat transfer. The trend of the current results is consistent with the findings reported in [33,34,59].

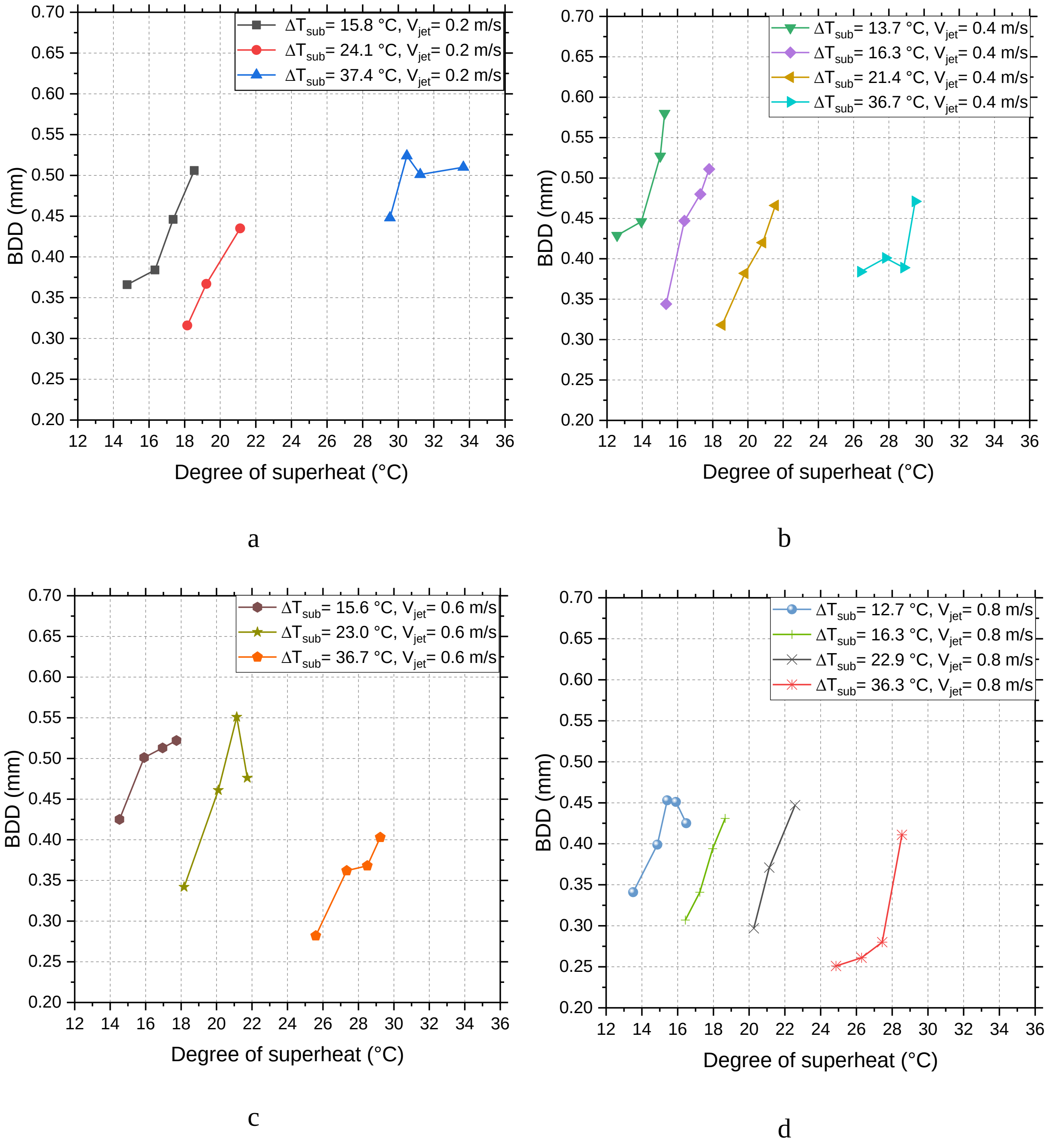

a

b

c

d

Figure 4.4: Variation of bubble departure diameter with the degree of superheat at jet velocities (a) 0.2 m/s, (b) 0.4 m/s, (c) 0.6 m/s, and (d) 0.8 m/s.

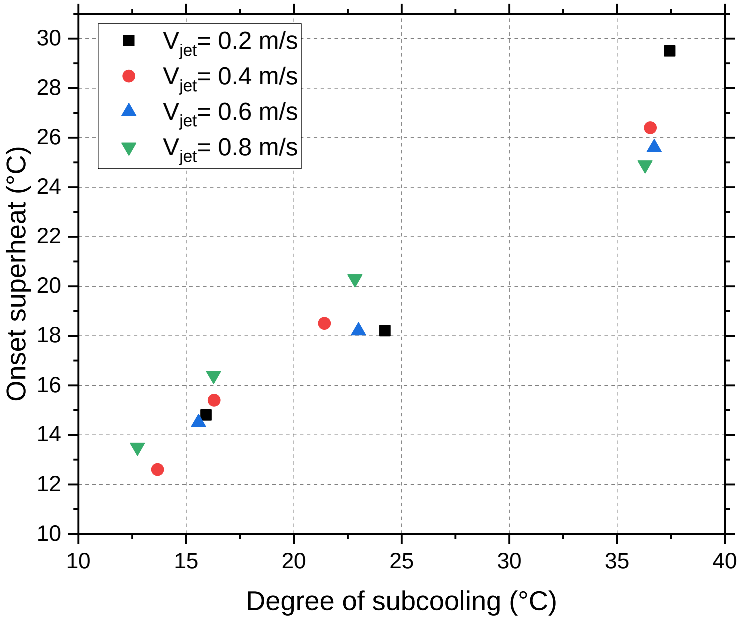

Figure 4.5: Effect of degree of subcooling on the onset of bubble nucleation.

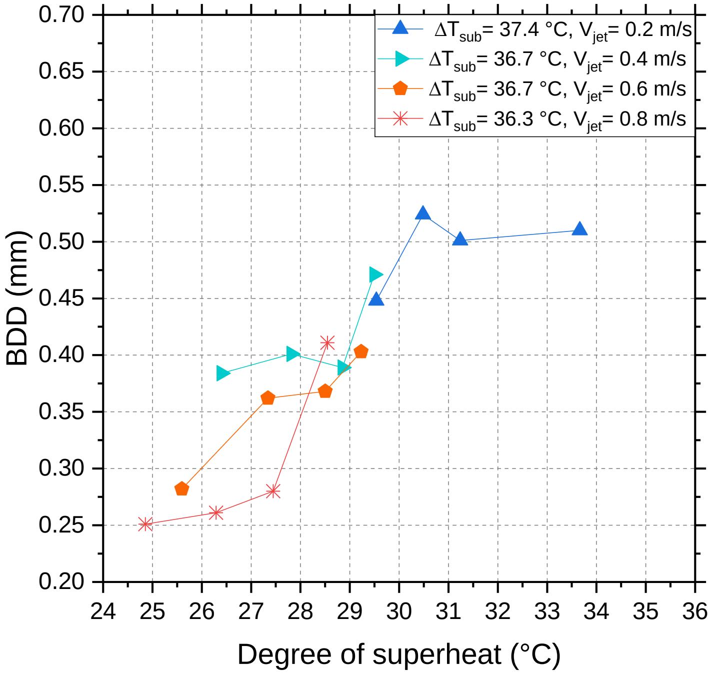

Figure 4.6: Effect of jet velocity on the BDD at relatively higher degree of subcooling.

The BDD data obtained from the 55 experiments conducted during this study is provided in Table A.1 in Appendix (A). An empirical model has been developed using this data. The model is provided here in equation (4.6).

$$D^* = 0.141 \times \frac{Ja_{sup}^{1.263}}{Ja_{sub}^{0.934} \times Re^{0.120}} \tag{4.6}$$

Where $\boldsymbol{D}^* = \frac{D_b}{\sqrt{\sigma/g\Delta\rho}}$, Reynolds number $Re = \frac{\rho_l V_j D_j}{\mu_f}$, superheat Jacob number $Ja_{sup} = \frac{\rho_l c_p \Delta T_{sup}}{\rho_v h_{fg}}$, and subcooled Jacob number $Ja_{sub} = \frac{\rho_l c_p \Delta T_{sub}}{\rho_v h_{fg}}$.

Figure 4.7 shows a comparison of the measured BDD with the predicted BDD using the empirical model in equation (4.6). The comparison also includes results obtained using the empirical models developed by Prodanovic et al. [28] and Du et al. [32] under flow boiling conditions. It is worth noting here that the values of the BDD observed under flow boiling conditions [29, 33] are larger than those observed under jet impingement boiling conditions, which is expected due to the effect of jet momentum on the force balance and heat balance. The values of the predicted BDD using the present model agree with the present experimental data with a relative deviation of 11.7 %, compared to 31.1 % and 82.5 % using Prodanovic's and Du's models, respectively. To the best of the author's knowledge, the empirical model presented in equation (4.6) is the first empirical model that has been developed to predict the BDD within the stagnation zone under JIB conditions.

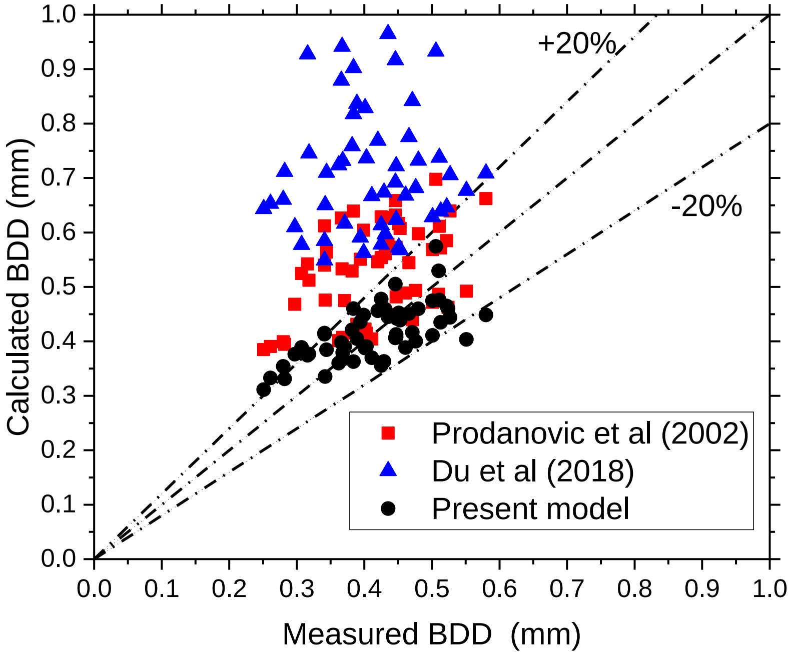

Figure 4.7: Comparison of the predicted BDD using the present empirical model and models reported in [28,32] and current experimental data.

Figure 4.8 shows consecutive images taken for a single growing bubble, starting from its embryo state to its disappearance due to condensation from the subcooled liquid. These images have been taken during an experiment conducted at a degree of subcooling of 16.5 °C, degree of superheat of 14.8 °C, wall heat flux of 708.6 kW/m^2, and jet velocity of 0.2 m/s. One can notice that the bubble grew rapidly at the early stages (at time < 0.5 ms). The bubble growth slowed down before the bubble departed the surface at t = 1.3 ms. After that, the bubble shrunk and collapsed within the subcooled liquid. It is worth noting that all bubbles observed within the jet stagnation zone during the current study did not slide over the surface before departing the heated surface. Rather, all bubbles lifted off (departed) and then collapsed within the subcooled liquid.

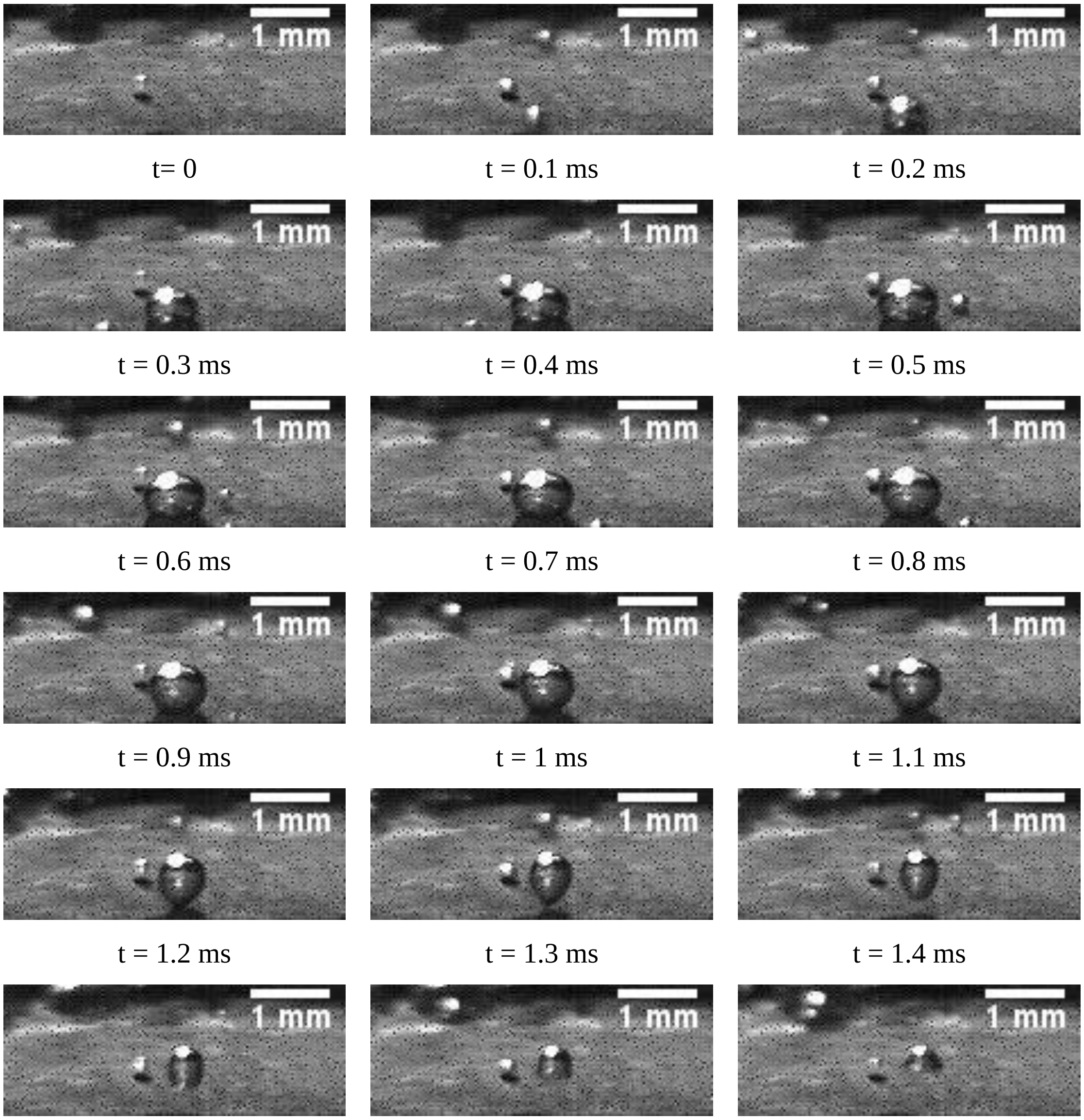

t= 0 | t = 0.1 ms | t = 0.2 ms

t = 0.3 ms | t = 0.4 ms | t = 0.5 ms

t = 0.6 ms | t = 0.7 ms | t = 0.8 ms

t = 0.9 ms | t = 1 ms | t = 1.1 ms

t = 1.2 ms | t = 1.3 ms | t = 1.4 ms

t = 1.5 ms | t = 1.6 ms | t = 1.7 ms

Figure 4.8: Consecutive images taken for a single growing bubble taken at ΔT_{sub}=16.5 $°C$, ΔT_{sup}= 14.8 $°C$, $q_w^{''}$= 708.6 kW/m^2, V_{jet} =0.2 m/s.

4.3. Results of Mechanistic Modeling of BDD

In this section, a mechanistic model of the BDD was developed based on the force balance approach developed by [60] and the bubble growth models developed by [35,39,40,44,60]. The model has been validated using the current experimental data observed within the stagnation zone under JIB conditions. The relative deviation between the value of the predicted bubble departure diameter (BDD_P) by the current developed model and the experimentally obtained (BDD_{ex})is calculated using equation (4.7). This relative deviation has been used as a means of assessing the accuracy of the developed bubble growth model.

$$\text{Relative deviation (R.D.)} = \frac{\sum\left|(BDD_{ex}-BDD_{cal})/BDD_{ex}\right|}{N} \times 100 \qquad (4.7)$$

Where N is the number of experimental data.

Figure 4.9 shows a comparison between BDD_P calculated using different bubble growth models combined with the force balance equation (4.1) and the measured BDD from the current experiments. The bubble growth model developed by Mikic et al. [39] underestimated the current experimental BDD with a R.D. of about 48.8 %. Since their model was developed for pool boiling, one can expect a slower bubble growth rate compared with the flow boiling and JIB conditions. The bubble growth model developed by Yun et al. [40] overestimated the current experimental data with a R.D. of about 61.7 %. It is worth mentioning that the bubble growth models in [39,40] considered only heat transfer from the superheated layer and heat loss to the subcooled liquid. Colombo and

Fairweather [44] and Zhou et al. [35] improved these models by including heat transfer due to microlayer evaporation. Colombo and Fairweather [44] proposed an empirical constant C = 1.78 (see equation (4.2)) that best fitted the experimental data available in the literature during flow boiling conditions. The bubble growth model developed by [44] agreed well with the current measurements of BDD, with a R.D. of about 20.1 %. The bubble growth model by [35] using C= 1.45 predicted the present measured BDD with a R.D. of 37.1 %.

Ahmed and Hamed [37,60] applied the bubble growth model developed by Yun et al. [40] with a modified correction factor b=π/7 to predict the BDD in the stagnation area under JIB. Figure 4.11 shows a comparison of the BDD predicted using the model proposed by [60] and the current experimental data. Their model predicted 25% of the experimental data accurately with a R.D. of about 10.2 %. For the rest of the experimental conditions, the bubbles grew to the maximum diameter then shrank and vanished without departure.

Although the predicted BDD obtained by the model reported in [44] agreed with the current experimental data, the accuracy of the prediction could be further improved by adjusting the value of empirical constant C. The current mechanistic model uses the empirical constant C = 2.5 that gave the best agreement with the current experimental data, with a R.D. of about 17.8 %, as shown in Figure 4.11. This improvement could be explained by the fact that increasing the value of C reduced the contribution of the microlayer evaporation, which is expected under JIB conditions, in which case the BDD would be smaller than the BDD under flow boiling conditions.

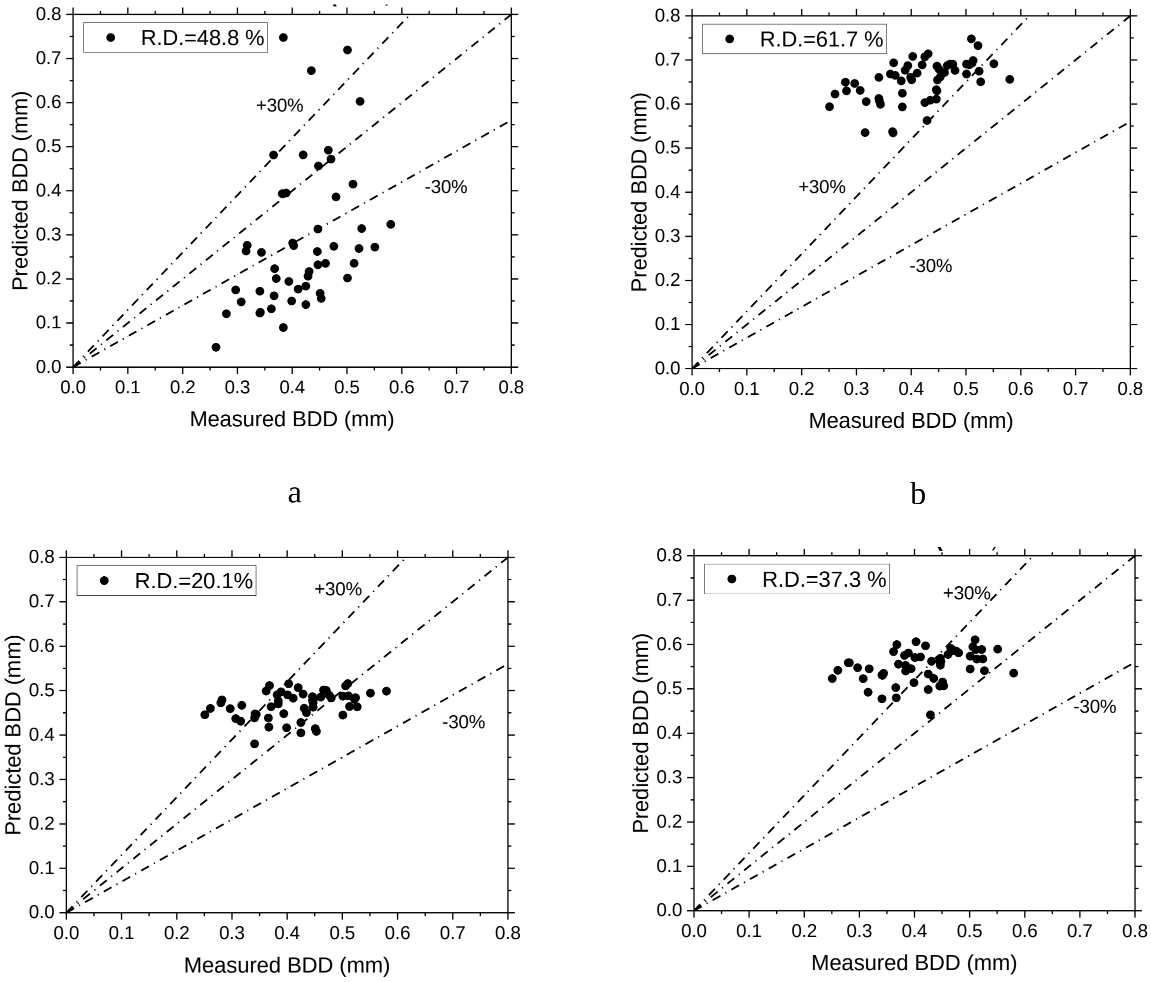

a

b

c

d

Figure 4.9: Comparison of the predicted BDD using models reported in a [39],b[40],c[44], d [35] and the current experimental results.

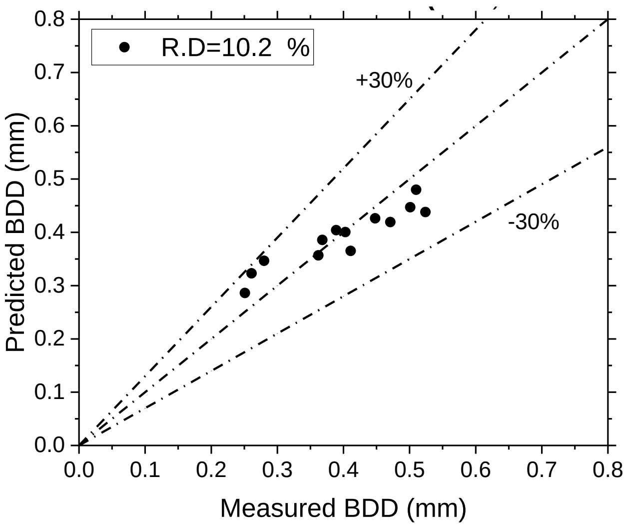

Figure 4.10: Comparison of the predicted BDD using the model developed by [60] and the current experimental data.

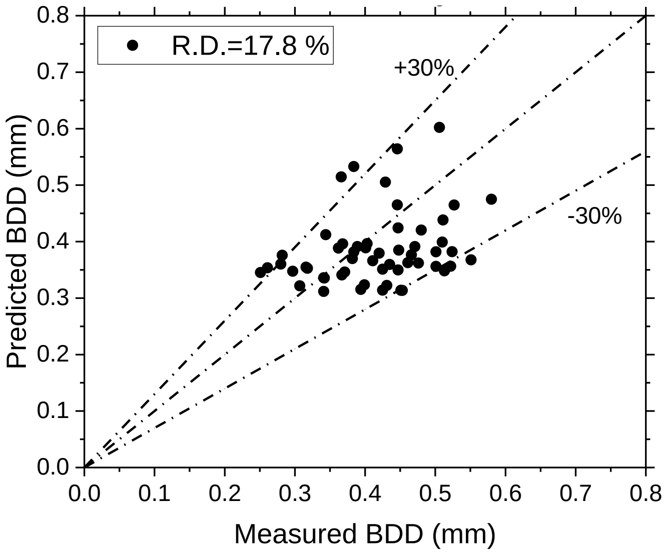

Figure 4.11: Comparison of the predicted BDD using the present model and the measured BDD.

4.4. Results of Mechanistic Modeling of Bubble Growth Rate

Figure 4.12 compares the predicted bubble growth rate obtained using different models with the measured growth rate during a JIB carried out at degree of subcooling of 16.3 °C, superheat of 16.4 °C, heat flux of 836.21 kW/m^2, and jet velocity of 0.8 m/s. Among the used models, the model developed by Yun et al. [40] produced the fastest growth rate hence it overpredicted the BDD. The slowest growth rate was obtained using the model developed by Mikic[39]. The bubble growth rate obtained by Colombo and Fairweather [44] is slightly higher than that observed in the current experiments. It can be seen that the proposed model (with C = 2.5) not only improved the accuracy of the predicted BDD, but also enhanced the agreement with the current bubble growth rate experimental data.

Figure 4.13 shows the contribution of each heat transfer mechanism, included in equation 4.2, to the bubble growth process. It can be seen clearly that the contribution of the heat transfer from the microlayer evaporation (D_{mic}) underneath the growing bubble dominates the bubble growth process. Moreover, the contribution of the heat transfer from the superheated layer (D_{sup}) to the bubble growth is insignificant due to the small surface area of the growing bubble in the stagnation zone exposed to the subcooled liquid. These results agree with the results reported in [45] for flow boiling conditions.

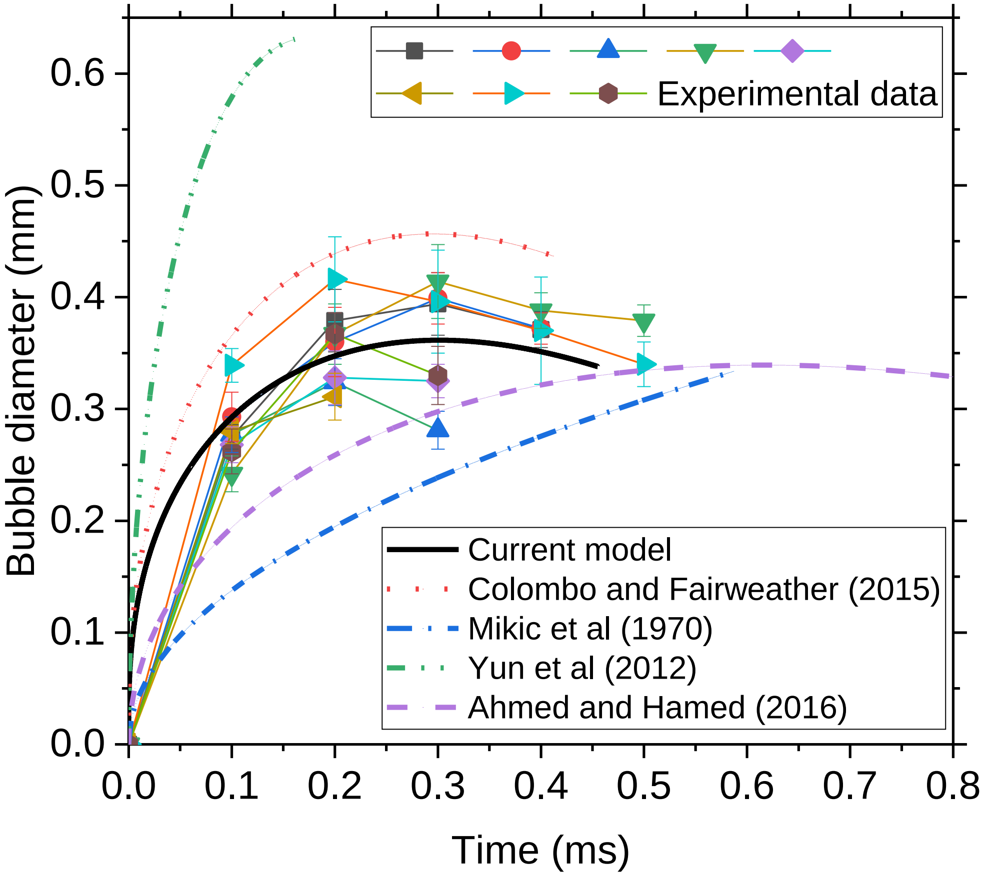

Figure 4.12: Comparison of bubble growth predictions with experimental transient growth at $\Delta T_{sup} = 16.4\ °C, q''_w = 836.21\ KW/m^2, \Delta T_{sub} = 16.3\ °C, V_{jet} = 0.8\ m/s$.

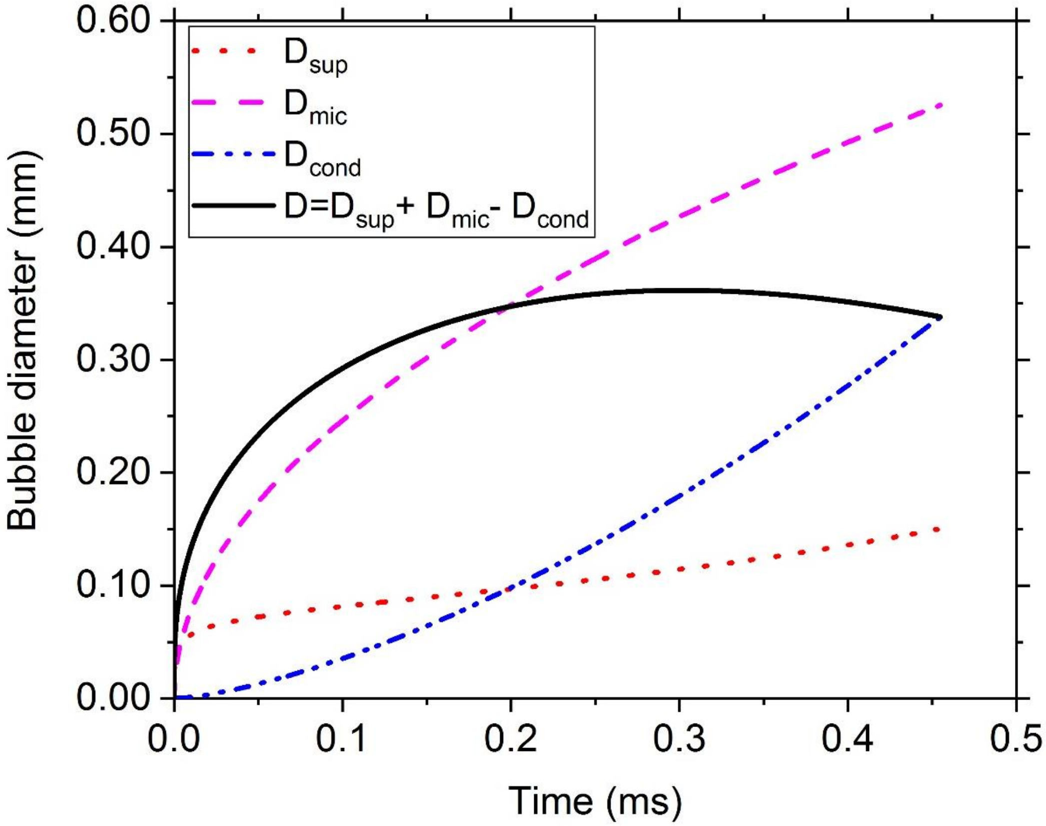

Figure 4.13: Predicted bubble growth and contributions of different mechanisms obtained by the current model at ΔT_{sup}=16.4 °C, q''_w= 836.21 kW/m^2 ,ΔT_{sub}=16.3 °C , V_{jet}=0.8 m/s.

5. Chapter 5: Transition Boiling Heat Transfer

5.1. Mechanistic Modeling of Transition Boiling

The current study adopted the mechanistic model developed by Ahmed and Hamed [9]. They divided the total heat flux $q_w^{"}$ into two heat transfer partitions (mechanisms) that coexisted during the transition boiling regime: (i) intrusion heat transfer, $q_i^{"}$ and (ii) quenching heat transfer, $q_q^{"}$.The original model has been revised by considering the rate of heat transfer due to evaporation $q_l^{"}$. The model developed in this study is presented here by equation (5.1)

$$q_w^{"} = Aq_i^{"} + (1 - A)q_q^{"} + q_l^{"} \tag{5.1}$$

Where A is a weighting function to transition from the quenching component at moderate surface superheat to the intrusion component at high surface superheat. A is calculated in [9] by equation (5.2)

$$A = \left(\frac{\Delta T_{sup}}{\Delta T_{min}}\right)^{n}, \text{ n=0.4} \tag{5.2}$$

The quenching heat transfer, $q_q^{"}$, in equation (5.1) is calculated by using equation (5.3)

$$q_q^{"} = \frac{k_l(T_w - T_l)}{\sqrt{\pi\alpha t}} \tag{5.3}$$

k_l, α, T_w, T_l, and t in equation (5.3) are the liquid thermal conductivity, the liquid thermal diffusivity, the wall temperature, the liquid temperature, and the liquid-surface contact time, respectively. The liquid-surface contact time, t, can be estimated as $t = 1/f$ if the vapor layer frequency, f, is known [9,19]. In the current work, the vapor layer frequency at each boiling condition was measured and used to estimate $q"_q$.

Ahmed and Hamed[9] showed that the heated surface rewetting mechanism is governed by a Rayleigh-Taylor instability of the liquid-vapor interface. In reference to Figure 5.1, the Rayleigh-Taylor instability occurs when fluid 2, with a relatively higher density, lays on top of fluid 1, which has a relatively lower density. Due to the density difference between the liquid and vapor, the liquid accelerates into the vapor layer, which disturbs the liquid-vapor interface. When the acceleration is from the lighter fluid (vapor) into the denser fluid (liquid), the disturbance of the liquid-vaper interface grows, otherwise, the disturbances will diminish and the instability of the vapor interface decreases [61]. In jet impingement boiling, the jet momentum contributes to the instability of the vapor interface, besides the effect of the density difference.

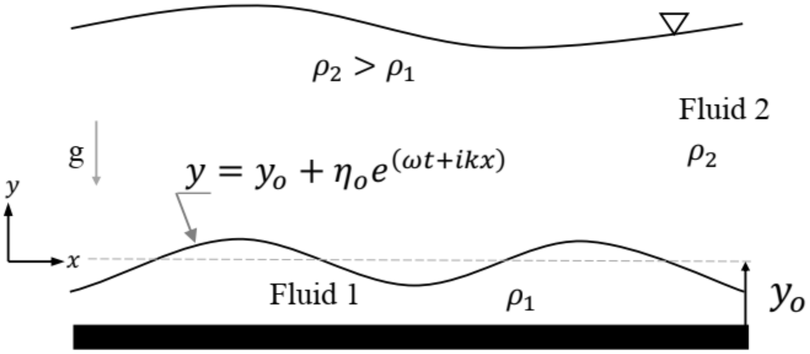

Figure 5.1: Rayleigh-Taylor instability[9].

Ahmed and Hamed [9] assumed the intrusion component, $q_i^{"}$, is due to transient conduction. They used equation (5.4) to calculate $q_i^{"}$.

$$q_i^{"} = \frac{\rho_l A_l \delta_v C_{p,l} \Delta T_{sub}}{A_{eff}} \frac{A_l}{A_c} \omega \tag{5.4}$$

ρ_l is the liquid density,

$C_{p,l}$ is the liquid specific heat capacity,ΔT_{sub} is the liquid subcooling,

A_l is the liquid intrusion area. A_{eff} is the effective area where surface is rewetted. For stagnation zone, $A_{eff} = cA_h$, c=0.4, A_h is the heater area, $\frac{A_l}{A_c}$ is the area ratio between the liquid area and total area occupied by two phases, see Figure 5.2 and calculated as $\frac{A_l}{A_c} = \frac{\pi}{8\sqrt{3}}$, δ_v is the liquid intrusion height, which is assumed to be equal to the vapor layer thickness[9], ω is the instability growth rate.

The instability growth rate is calculated from the dispersion equation (5.5) originally developed by Taylor[62] and Lewis[63] and modified by Hsieh[64] to consider the effect of heat and mass transfer on Rayleigh-Taylor instability.

$$[\rho_v \coth(k\delta_v) + \rho_l \coth(k\delta_l)]\omega^2 + \left[\frac{k_v \Delta T_{sup}}{\delta_v h_{fg}} \left(\frac{1}{\delta_v} + \frac{1}{\delta_l}\right) (\coth(k\delta_v) + \coth(k\delta_l))\right] \omega + [(\rho_v - \rho_l)ak + \sigma k^3] = 0 \tag{5.5}$$

ρ_v is the vapor density, ρ_l is liquid density, k_v is the vapor thermal conductivity, h_{fg} is the latent heat, σ is the surface tension, a is the total acceleration, δ_l is the liquid layer thickness, δ_v is the vapor layer thickness, k is the wavenumber defined as $k = 2\pi/\lambda$.

From the Rayleigh-Taylor instability analysis, the liquid intrudes the vapor layer and touches the surface at locations separated by the most dangerous wavelength λ_d which is defined as the wavelength with the maximum instability growth rate and calculated as expressed in equation (5.6)

$$\lambda_d = \sqrt{3}\lambda_c \tag{5.6}$$

where λ_c is the critical wavelength at which the perturbation starts to grow calculated from equation (5.7). The vapor layer thickness δ_v in equation(5.5) is estimated by the most cited correlation proposed by Berenson[65], equation (5.8)

$$\lambda_c = 2\pi\sqrt{\frac{\sigma}{a(\rho_l - \rho_v)}} \tag{5.7}$$

$$\delta_v = \mathrm{C}_{min}\left[\frac{\mu_v k_v \Delta T_{sup}}{\rho_v \Delta\rho h_{fg} a}\left(\frac{\sigma}{\Delta\rho a}\right)^{1/2}\right]^{1/4} \tag{5.8}$$

Where $\mathrm{C}_{min} = 2.35$ is an empirical constant proposed by Berenson[65] for pool boiling conditions. The total acceleration a in the above equations is calculated from equation (5.9).

$$a = g + \frac{V_j^2}{2\delta_l} \tag{5.9}$$

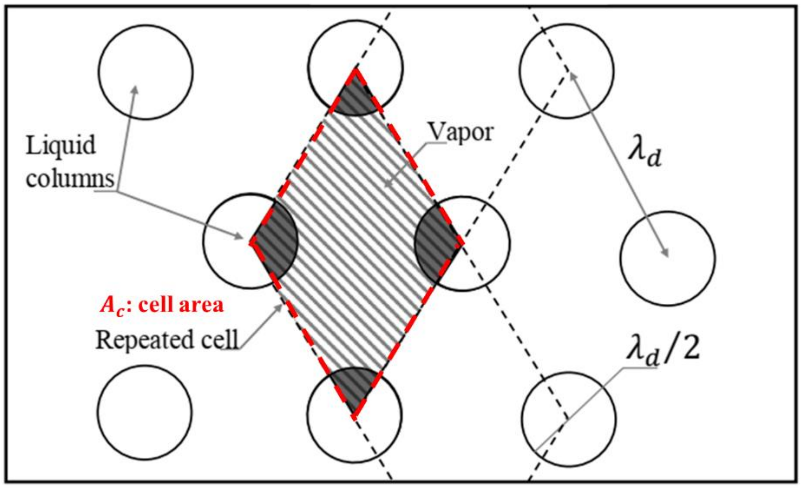

Figure 5.2: Schematic of liquid columns intruding a vapor layer[9].

The third component of the mechanistic model, latent heat, $q_l^{"}$, is calculated from the correlation proposed by Zuber[61] who calculated the film boiling heat flux in pool boiling. The correlation takes the following form:

$$q_l^{"} = \mathrm{C}\rho_v h_{fg}\lambda_d\omega \tag{5.10}$$

Where C is an empirical constant. Zuber [61] proposed C= 0.131 for pool boiling conditions . The empirical constant C, equation (5.11), is proposed to fit the total heat flux measured during JIB conditions.

$$\mathrm{C} = 5.33576\times10^{-5}\Delta T_{sub}^2 - 2.73\times10^{-3}\Delta T_{sub} + 5.77\times10^{-2} \tag{5.11}$$

5.2. Boiling Curve and Vapor Breakup Frequency

This section presents the measured boiling heat flux and corresponding vapor breakup frequency during JIB experiments carried out at jet velocity of 1 m/s and degrees of subcooling of 11 °C, 27 °C, 41 °C, and 49 °C. At each flow condition, the measurements of the boiling curve and the corresponding vapor breakup frequency were repeated three times. The average frequency was then calculated.

In general, the boiling curves have good repeatability within the nucleate boiling regime. However, the measurements of heat flux within the transition regime were scattered, as shown in Figures 5.3, 5.5, 5.7, and 5.9. It is worth mentioning that Bogdanic [19] observed scattering in the shoulder heat flux and attributed it to the explosive boiling where the liquid experiences a vigorous phase change during the wetting of superheated surfaces. The results of vapor breakup frequency have poor repeatability within the nucleate and transition regimes, as shown in Figures 5.4, 5.6, 5.8, and 5.10. The scattering in the vapor breakup frequency in the nucleate regime might be caused by the effect of neighboring nucleation sites on the optical probe signal. The scatter in the transition boiling might be attributed to the stochastic nature of the instability associated with the transition boiling regime. To the best of my knowledge, there is no published data on the repeatability of vapor layer frequency within the transition regime that can be used to compare with the results of the present study. The solid black line in Figures 5.3-5.10 represents the average of the three repeated experiments. The average frequency and heat flux have been used to validate the developed mechanistic model presented in section 5.1.

All averaged data for the boiling heat flux and the corresponding vapor breakup frequency are summarized in Figure 5.11 and Figure 5.12, respectively. At a degree of subcooling of 11°C, the shoulder heat flux reached almost 3.75 MW/m^2 then it started to decrease at a surface temperature of about 400 °C. The vapor breakup frequency exhibited a similar trend. It reached a plateau of about 1100 Hz, then it decayed. By increasing the degree of subcooling from 11 °C to 27 °C, 41°C, and 49 °C, the shoulder heat flux increased to 5.5 MW/m^2, 8.5 MW/m^2, and 10 MW/m^2, respectively. Furthermore, the frequency increased to 2000 Hz at 27 °C and about 3000 Hz at 41 °C and 49 °C. Increasing the vapor breakup frequency might be attributed to the increase in vapor layer condensation caused by the higher degree of subcooling, which increased the instability of the vapor-liquid interface. It should be noted that the boiling curves obtained at a degree of subcooling of 41 °C and 49 °C overlapped at surface temperature of about 400°C. The frequency curves overlapped at surface temperature of about 300 °C. The resolution of the results could have been improved by increasing the number of frequency measurements.

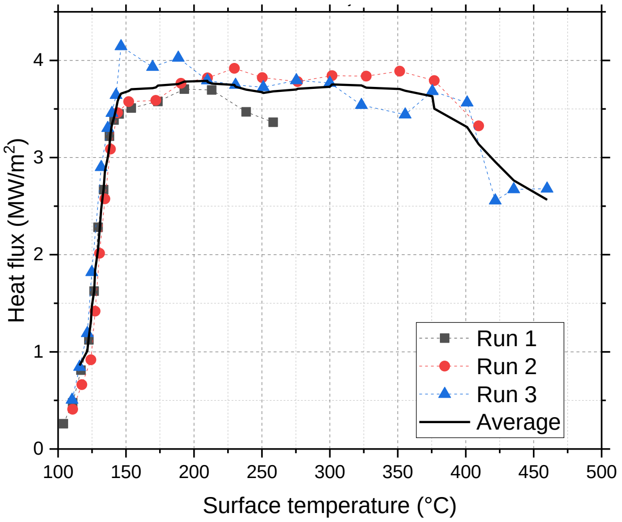

Figure 5.3: Variation of heat flux with surface temperature at ΔT_{sub} =11 °C, V_{jet}= 1 m/s.

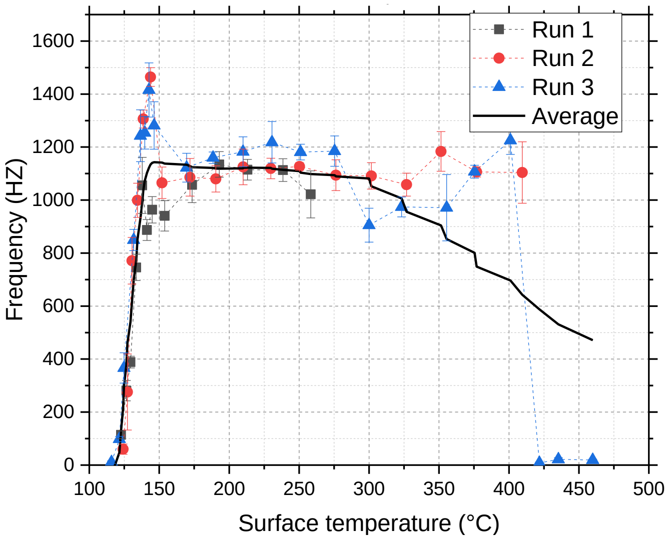

Figure 5.4: Variation of vapor breakup frequency with surface temperature at ΔT_{sub} =11 °C, V_{jet}= 1 m/s.

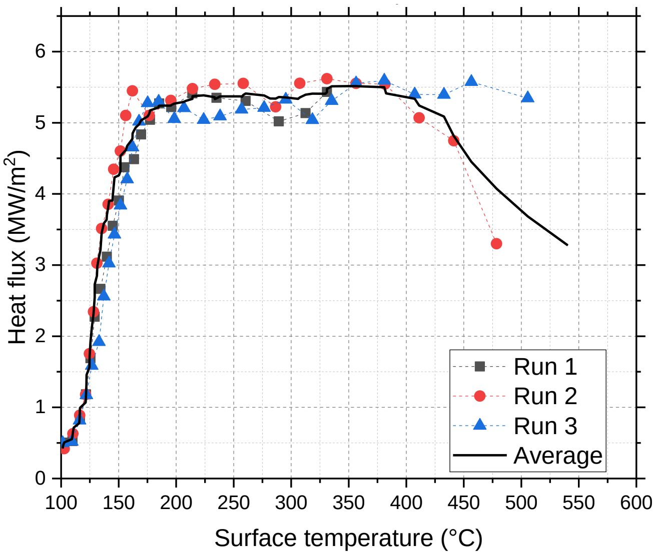

Figure 5.5: Variation of heat flux with surface temperature at ΔT_{sub} =27 °C, V_{jet}= 1 m/s.

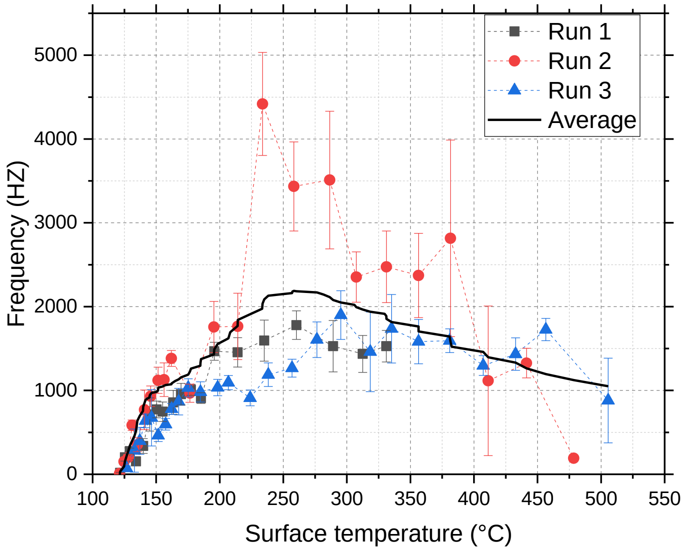

Figure 5.6: Variation of vapor breakup frequency with surface temperature at ΔT_{sub} =27 °C, V_{jet}= 1 m/s.

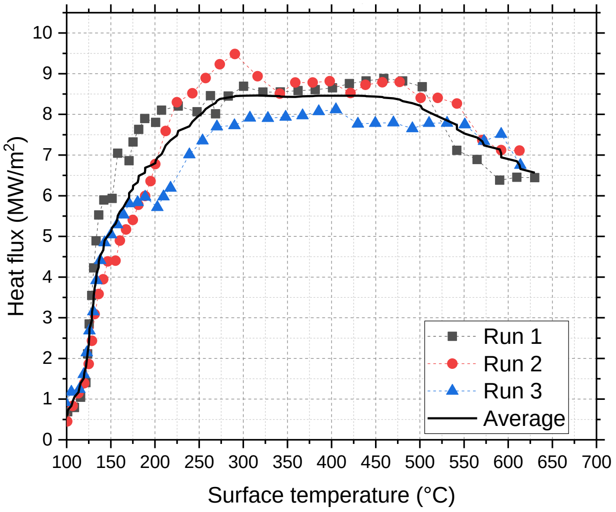

Figure 5.7: Variation of heat flux with surface temperature at ΔT_{sub} =41 °C, V_{jet}= 1 m/s.

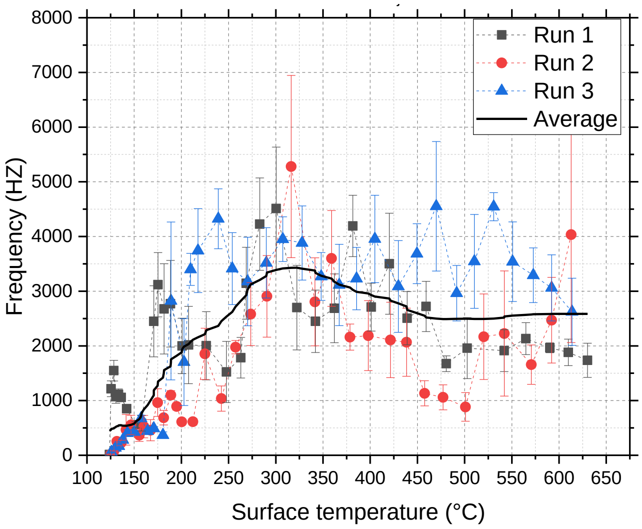

Figure 5.8: Variation of vapor breakup frequency with surface temperature at ΔT_{sub} =41 °C, V_{jet}= 1 m/s.

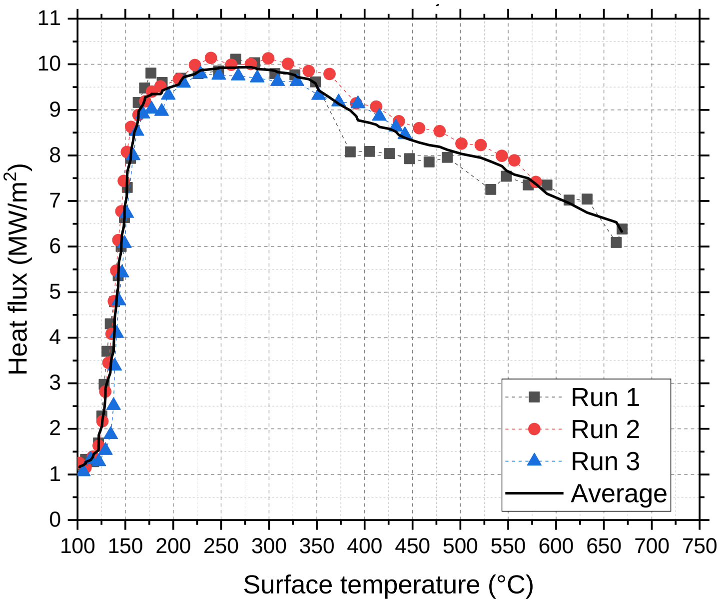

Figure 5.9: Variation of heat flux with surface temperature at $\Delta T_{sub} = 49$ °C, V_{jet}= 1 m/s.

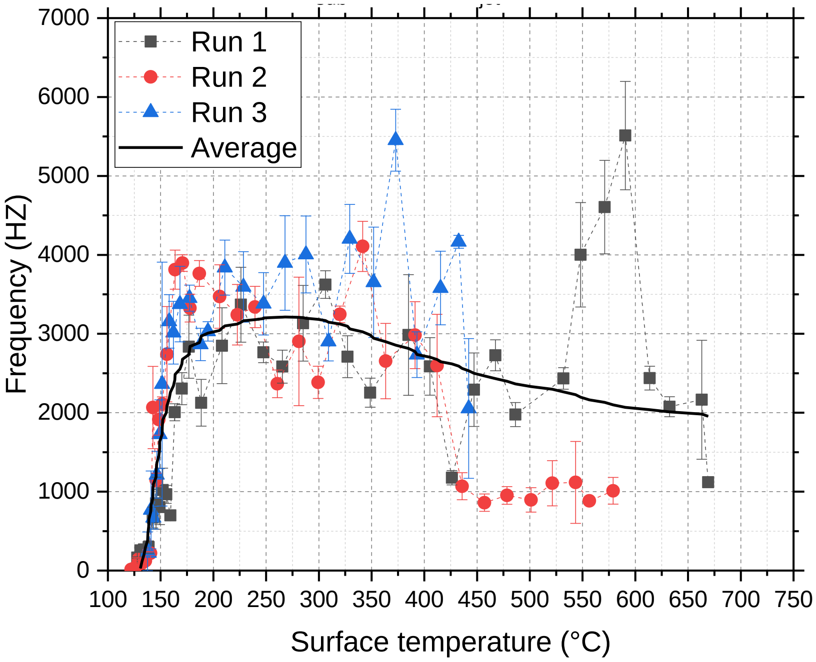

Figure 5.10: Variation of vapor breakup frequency with surface temperature at $\Delta T_{sub} =$ 49 °C, V_{jet}= 1 m/s.

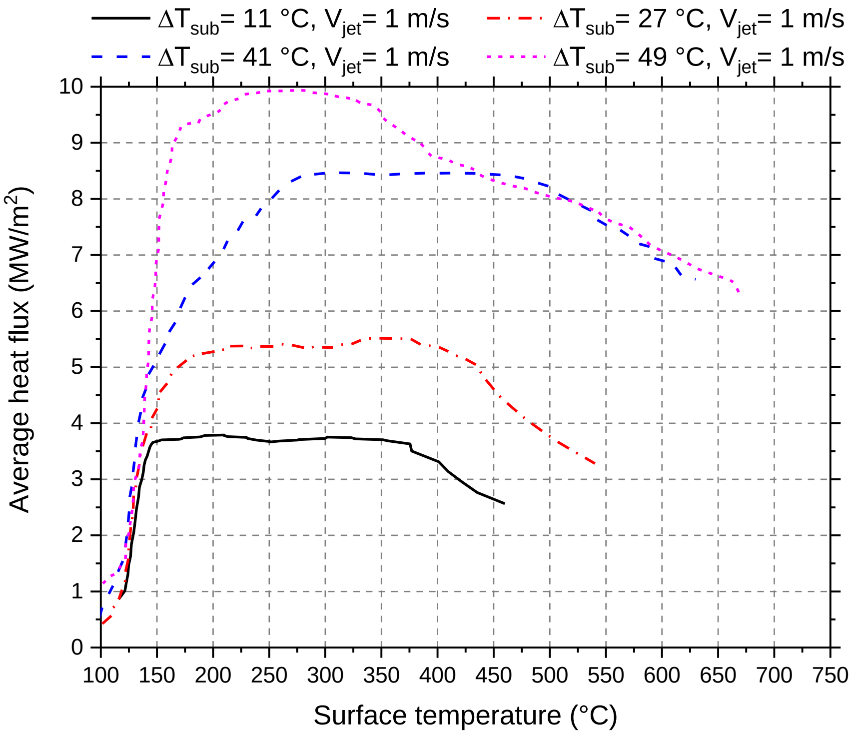

Figure 5.11: Average heat flux obtained for all experiments.

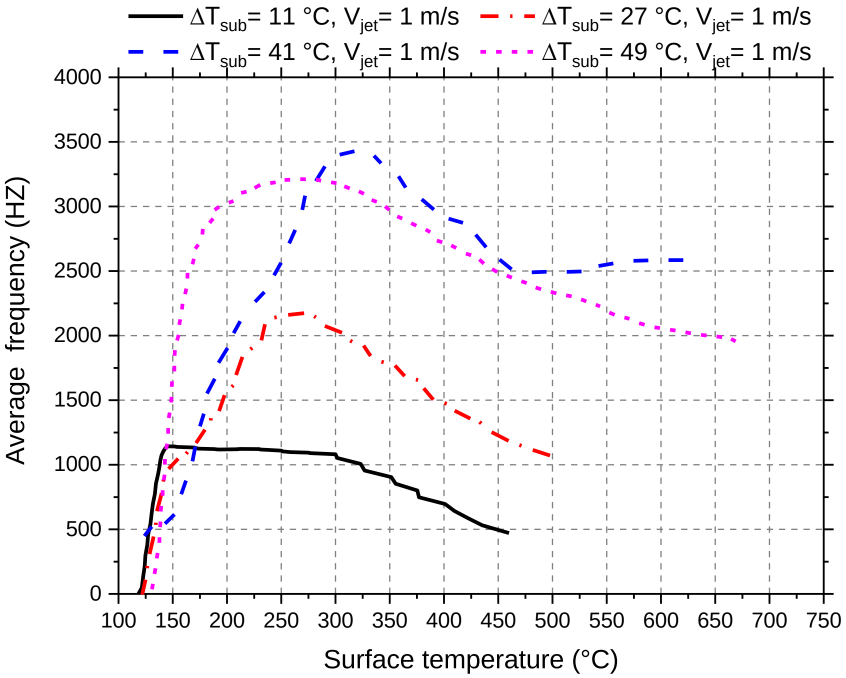

Figure 5.12: Average vapor breakup frequency obtained for all experiments.

5.3. Mechanistic Model Validation

The mechanistic model described in Section 5.1 has been used to predict the total surface heat flux within the transition regime under JIB conditions. The model predictions have been compared with the experimental data available in the limited literature, reported in [9,19]. The model predictions have also been compared with current experimental data shown in Figure 5.11.

Figure 5.13 and Figure 5.14 show a comparison of the surface heat flux predicted by the current mechanistic model and experimental data obtained by [9] and [19], respectively. The current mechanistic model predicted the experimental data with acceptable accuracy. The model gave relative deviations of 12 % with results reported in [9] and 25 % with results reported in [19]. It is worth noting here that the available data in the literature, especially the measurements of vapor contact frequency, is limited to degrees of subcooling of 20 °C and degrees of surface superheat of 340 °C. The current study was able to attain a surface superheat of about 570 °C, as shown in Figure 5.15.

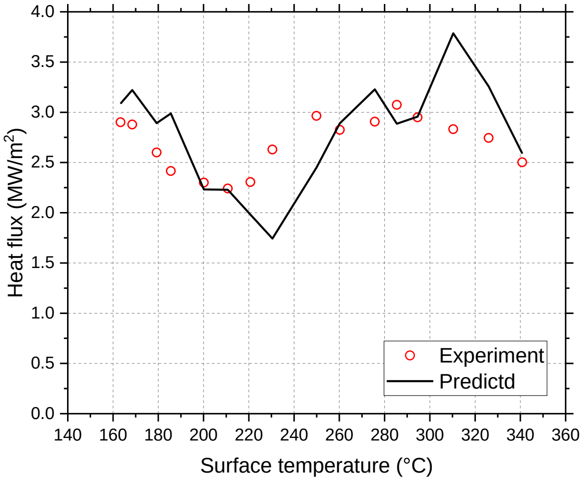

a

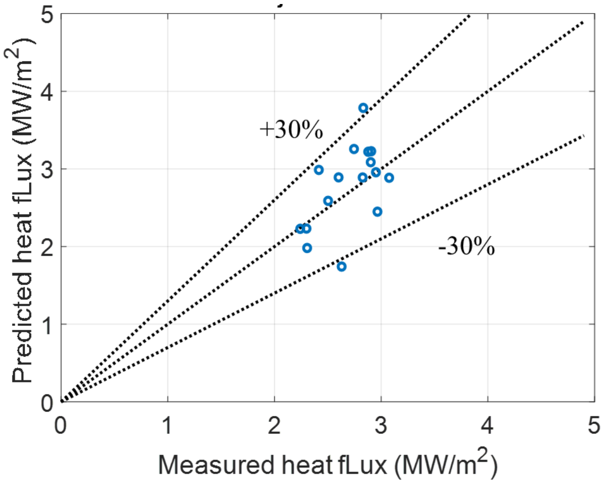

b

Figure 5.13: Comparison of the predicted heat flux and the measured heat flux in [9] at

ΔT_{sub} = 15 °C, V_{jet}= 0.4 m/s.

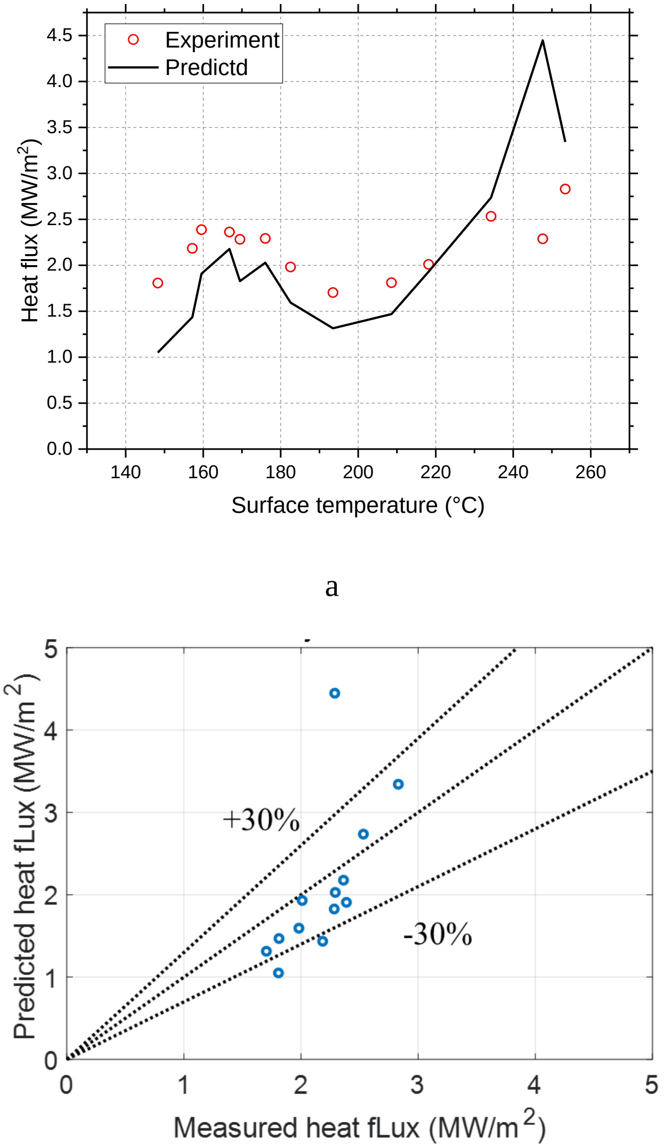

a

b

Figure 5.14: Comparison of the predicted heat flux and the measured heat flux in [19] at $\Delta T_{sub} = 20$ °C, V_{jet}= 0.4 m/s.

.

Figure 5.15 shows a comparison between the measured heat flux in the current work and the heat flux predicted by the current mechanistic model. The model was able to predict the experimental data reasonably well. The maximum relative deviation is within ± 20 % for all experiments. The relative deviation is 3.7 %, 4.9%, 4.6 %, and 11.3% for degrees of subcooling of 11 °C, 27 °C, 41 °C, and 49 °C, respectively, see Figure 5.16. Although the relative deviation in the predicted shoulder heat flux at the degree of subcooling of 49 °C is acceptable, the trend of the predicted heat flux is not consistent with the trend observed in the measured data. The predicted heat flux increases with the increase of the degree of subcooling. However, the effect of the degree of subcooling on the measured heat flux was noticeable up to surface temperature of about 350 °C. After that, the boiling curve overlapped with the boiling curve obtained with degree of subcooling of 41°C.

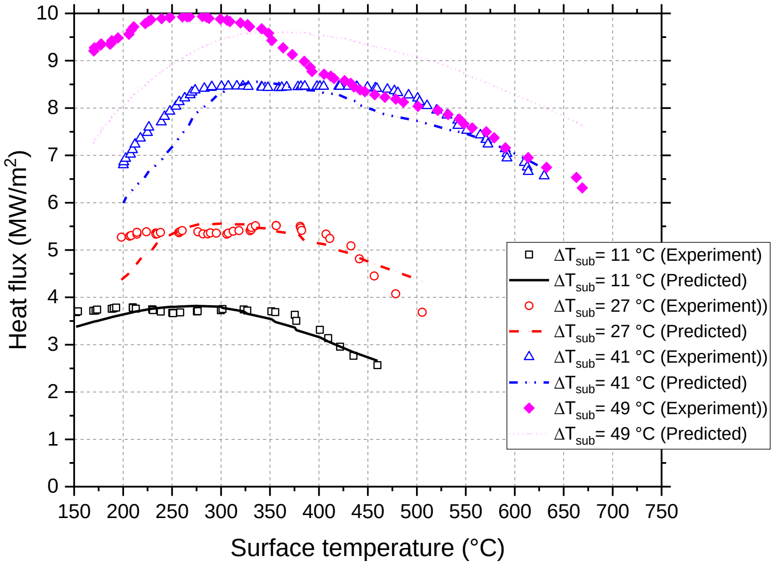

Figure 5.15: Comparison of the predicted and the measured heat flux in the present study.

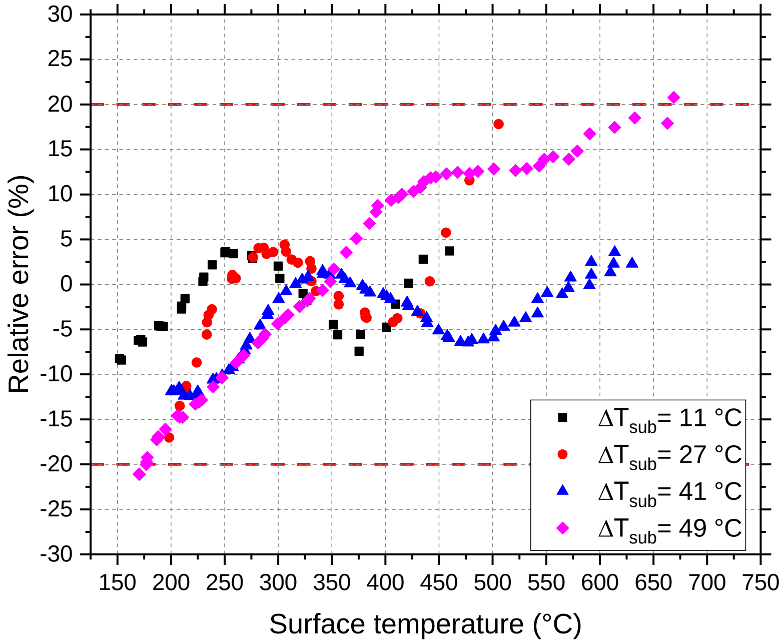

Figure 5.16: Relative deviation between the predicted and the measured heat flux.

Figure 5.17(a-c) shows the contribution of each heat transfer mechanism towards the total wall heat flux at all degrees of subcooling considered in this part of the study. At a degree of subcooling as low as 11 °C, the latent heat contribution represents 35-55 % of the total heat flux, depending on the surface superheat. This contribution is almost the same as the contribution of the quenching heat component. The intrusion heat flux represents the lowest contribution (about 10%), especially at low surface superheat. It increases with the surface superheat, which agrees with the findings reported in [9]. For higher degrees of subcooling, i.e., 27 °C, 41 °C, and 49 °C, the contribution of the latent heat decreases to 15-20 % of the total heat flux. The intrusion heat and quenching heat represent 20-40 % and 40-60 %, respectively. It is worth mentioning that Seiler-Marie et al. [50] hypothesized that the main heat transfer mechanism within the shoulder heat flux region is the heating up of the intruded liquid. Based on the current results, this assumption can be considered valid only at relatively high degrees of subcooling, where the contribution of latent heat decreases with the increase in the degree of subcooling compared to the other contributing mechanisms.

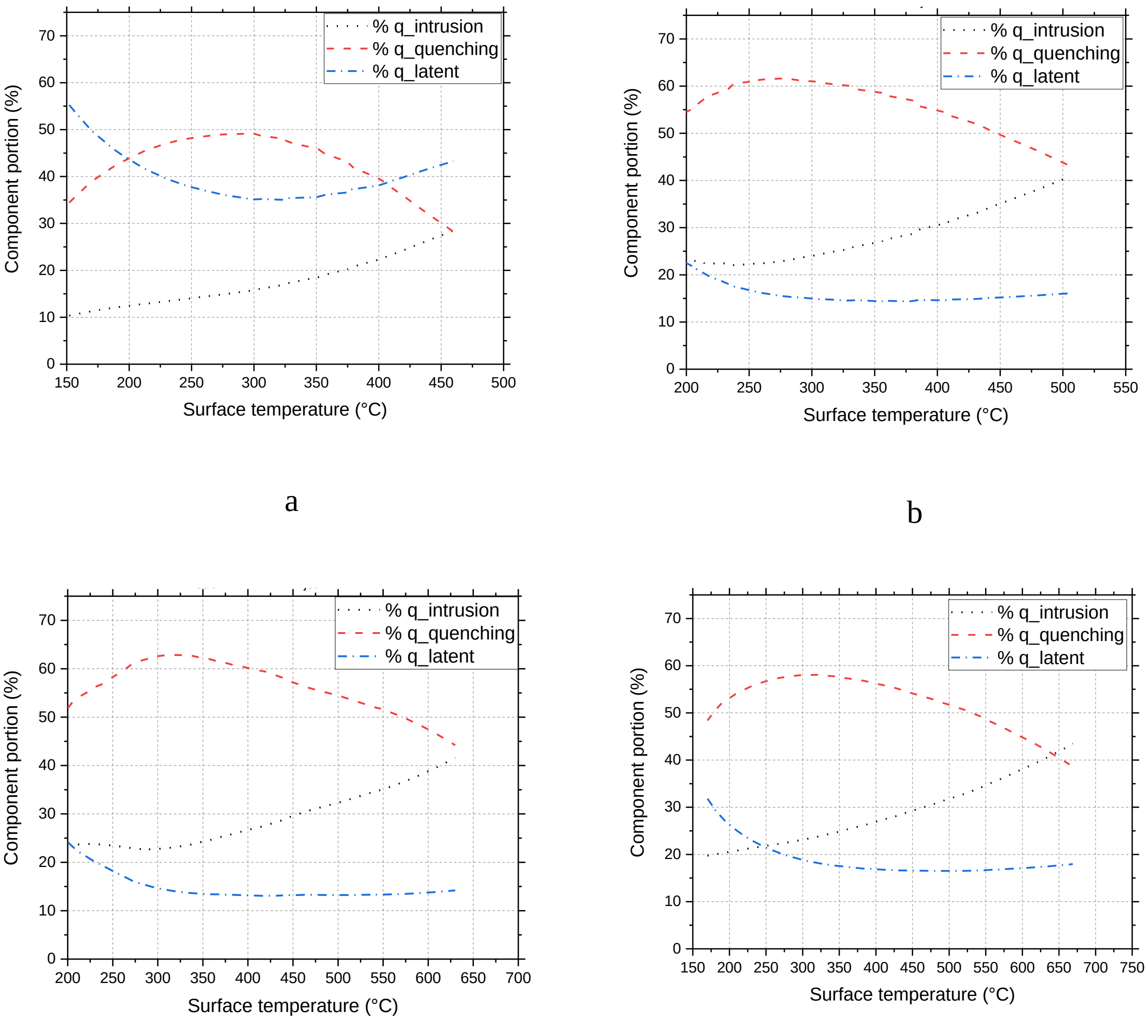

a

b

c

d

Figure 5.17: Contribution of various heat transfer mechanisms to the total surface heat flux at V_{jet}= 1 m/s and different degrees of subcooling, (a) $\Delta T_{sub} = 11$ °C, (b) $\Delta T_{sub} =$ 27 °C, (c) $\Delta T_{sub} = 41$ °C, and (d) $\Delta T_{sub} =$ 49 °C.

5.3.1. Mechanistic Model Sensitivity Analysis

This section presents the results of a sensitivity analysis that has been carried out to assess the impact of some of the input parameters and empirical constants used on the mechanistic model output. Table 5.1 summarizes the chosen parameters for model sensitivity analysis. The model sensitivity is defined as expressed in equation (5.12).

$$\text{Sensitivity \%} = \frac{q''_{predicted} - q''_{ref}}{q''_{ref}} \text{x} 100 \qquad (5.12)$$

q''_{ref} is calculated heat flux using the proposed model in section 5.1 and $q''_{predicted}$ is the predicted heat flux with changing the values of tested parameters shown in Table 5.1.

Table 5.1: Parameters are chosen for sensitivity analysis.

Parameter	Appears in
n	$A = \left(\frac{\Delta T_{sup}}{\Delta T_{min}}\right)^n$, recommended n=0.4
c	$A_{eff} = cA_h$, recommended c=0.4 , equation (5.4)
f : vapor layer frequency	equation (5.3)
δ_v : vapor layer thickness	equation (5.8)

The results of sensitivity analysis are shown in Figure 5.18. The empirical coefficients n,c, and measured breakup frequency did not influence the predicted heat flux significantly. The predicted heat flux changed by about 3.2 %, 2.4 %, and 2.5 % when the aforementioned parameters changed by about 20%, respectively. Furthermore, the vapor layer thickness (δ_v) seemed to have a significant effect on the model results. The predicted heat flux changed by about 41.2 % when the vapor layer thickness changed by 20%.

The vapor layer thickness, δ_v, was not measured during this study, however, it was calculated using the correlation proposed by Berenson[65], equation (5.8), which was developed for pool boiling. The original model, equation (5.8), used an empirical constant $\mathrm{C}_{min} = 2.35$ that was used in the current model as well. As mentioned before, the model was found to be very sensitive to the estimated vapor layer thickness, however, the sensitivity decayed at values lower than the recommended, as shown in Figure 5.19. The sensitivity analysis has been performed at a ΔT_{sub}=11 °C, V_{jet}= 1 m/s, ΔT_{sup}=130.6 °C, and q_s''= 3.73 MW/m^2 at which the model gave an accurate prediction of the total heat flux with a relative error of about 0%. Because the vapor layer thickness in the case of jet impingement is expected to be lower than that in pool boiling, it might be reasonable to consider the value of C_{min} of 2.35 suitable for use in the proposed mechanistic model since the model sensitivity decays below that value.

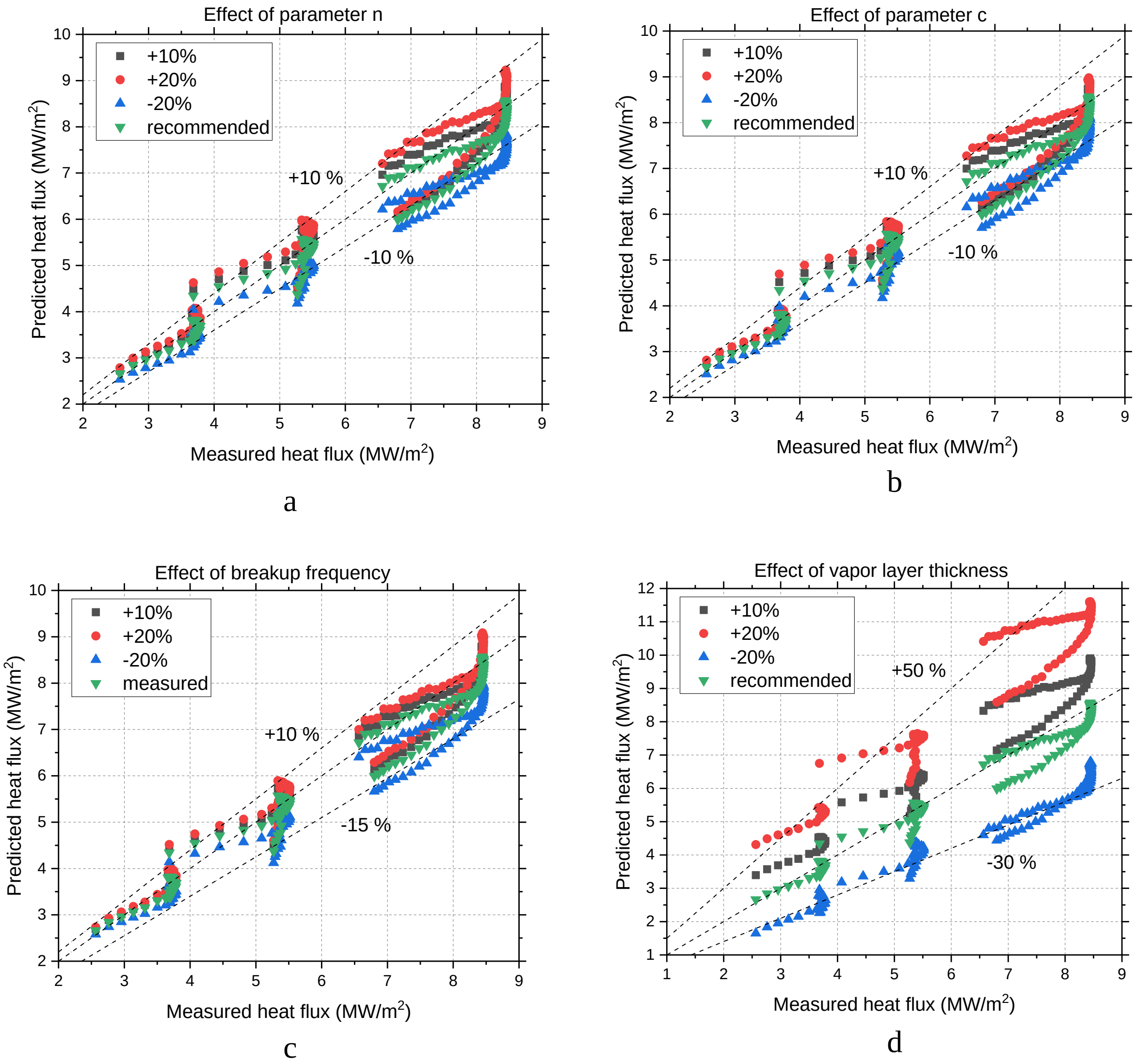

a

b

c

d

Figure 5.18: Sensitivity analysis of the parameters shown in Table 5.1.

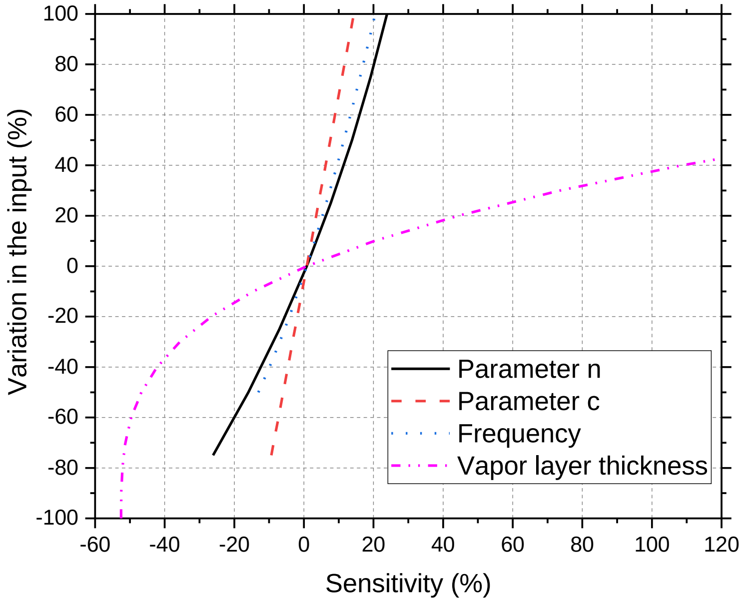

Figure 5.19: Sensitivity analysis of the parameters shown in Table 5.1 at ΔT_{sub}=11 °C, V_j= 1 m/s, ΔT_{sup}=130.6 °C, and q_s''= 3.73 MW/m^2 .

5.4. Vapor-Liquid Interface Visualization

This section presents the results of high-speed imaging of the formation/breakup of large vapor bubbles in the stagnation zone during the transition regime. Figure 5.20 shows two cycles of vapor formation followed by breakup at JIB of $V_j = 1$ m/s , $\Delta T_{sub} = 41$ °C, and $\Delta T_{sup} = 321$ °C. These images were captured with a frame rate of 3000 fps. The two cycles occurred during 58 frames. Not all frames are presented here. However, only frames that showed the stages of bubble nucleation, growth, and collapse are shown.

The first frame is considered to be at time t = 0, where the surface is almost completely wetted with the liquid and no bubbles were observed. At t =1 ms, small bubbles were observed. At t = 5 ms, the bubbles grew and started to coalesce and form a large volume bubble that isolated the surface. This is the time at which the Rayleigh-Taylor (RT) interfacial instability was observed. The RT instability caused the first bubble to collapse at t = 8 ms and the liquid rewetted the surface. Heat was transferred by transient conduction to heat the liquid till the saturation temperature. A second bubble formation was observed at t=11.3 ms. The bubble grew at t=13.3 ms, at which time the interfacial instability was observed. At t = 19.3 ms, the breakup of the second bubble took place until it finally disappeared due to condensation. It is worth noting here that cycles of bubble formation and breakup have been observed in [54]. The duration of these cycles was between 2 and 6 ms. The bubble breakup cycles that occurred during the current study were between 8 and 11 ms. The reason for the slight difference in cycle durations might be that the study [54] investigated the bubble cycles during high subcooling (i.e., 75 °C) on a sandblaster heated surface.

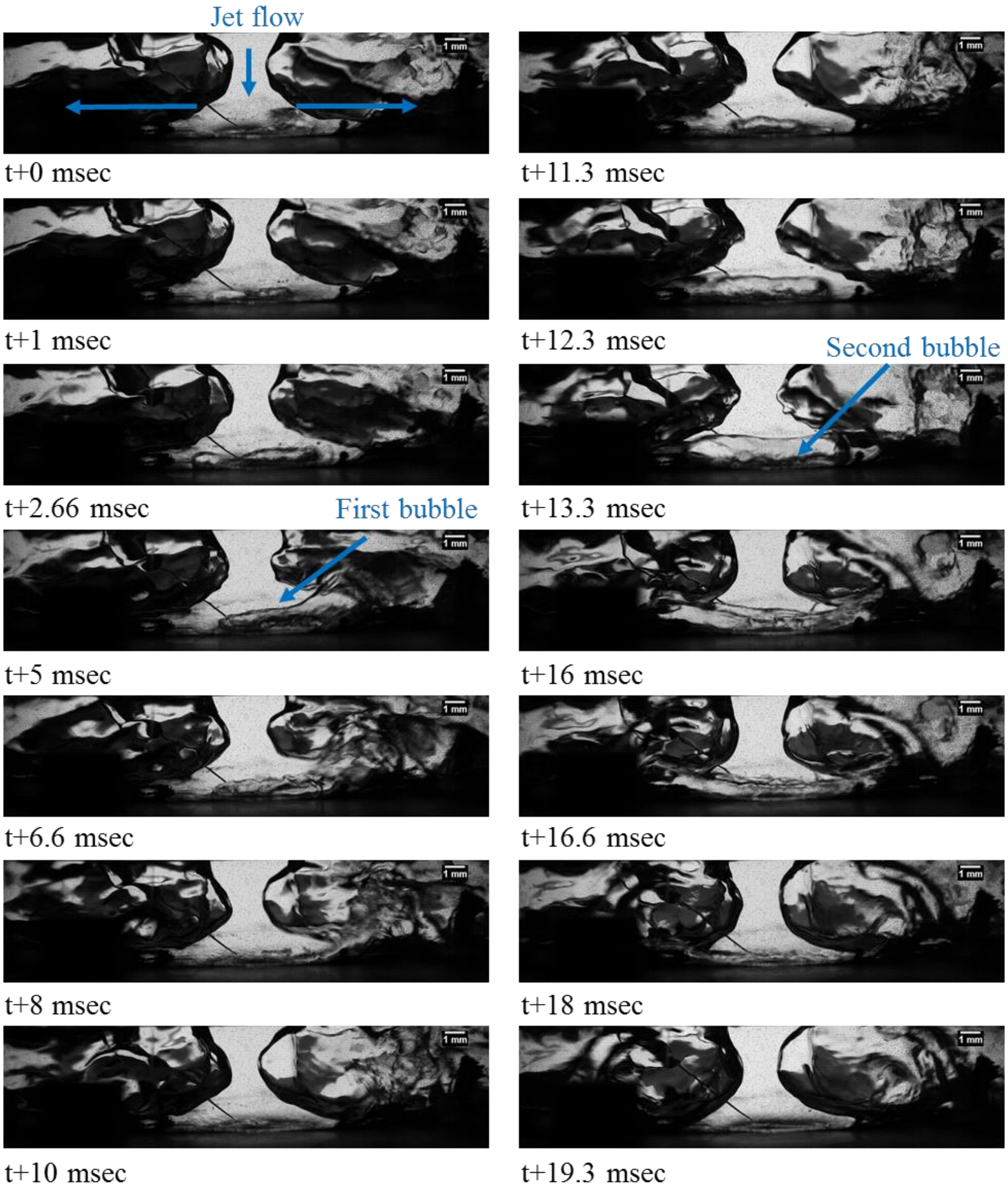

Figure 5.20:Bubbles formation and break-up at $V_{jet} = 1$ m/s , $\Delta T_{sub} = 41$ °C, $\Delta T_{sup} = 321$ °C.

6. Chapter 6: Conclusions and Future Work

6.1. Summary and Conclusions

Jet impingement boiling heat transfer has different characteristics other than those encountered in pool boiling and flow boiling. The JIB curve has similar heat transfer modes as in the pool and flow boiling. However, the transition regime in the case of JIB is characterized by a plateau in the heat flux, which is referred to as the shoulder heat flux region. The transition boiling regime in JIB is characterized by high instability that makes investigating and understanding the heat transfer mechanisms within this regime very challenging.

The first objective of the current study was to design a suitable heater block and experimental setup that enable one to investigate the entire JIB curve. The effects of jet velocity and degree of subcooling on the JIB curve have been investigated. The JIB curves have been obtained at jet velocities as high as 3.8 m/s and a degree of subcooling as high as 49 °C under steady-state conditions.

The second objective was to carry out experimental and mechanistic modeling of bubble dynamics within the nucleate boiling regime. The effects of the surface superheat, heat flux, jet velocity, and water subcooling on the bubble departure diameter (BDD) within the stagnation zone have been investigated. The scope of the current mechanistic models of bubble growth and bubble departure available in the literature for pool and flow boiling has been expanded to include jet impingement boiling. The following conclusions can be derived based on the work that has been carried out in this study.

- The BDD increased with the increase in the surface temperature and heat flux regardless of the degree of subcooling or jet velocity. Increasing the degree of subcooling resulted in a slight decrease in the BDD and an increase in the onset of nucleation temperature. The effect of jet velocity on the BDD was noticeable only at high degrees of subcooling.
- An empirical model has been developed to estimate the BDD within the stagnation region. The proposed model showed satisfactory accuracy with the experimental results with a relative deviation of about 12 %.
- A mechanistic model of bubble dynamics was developed based on the model developed by [45]. The value of the empirical constant was modified to C = 2.5. The model predicted the BDD with a relative deviation of about 18 % and gave a good agreement with the measured bubble growth rate. The mechanistic model results indicated that the most significant contribution to bubble growth under JIB conditions is microlayer evaporation.

The third objective was to study vapor layer instability within the transition region of the JIB curve. A fiber optic probe was used to measure the vapor layer breakup frequency in addition to high-speed imaging to capture the interfacial Rayleigh-Taylor instability. The following conclusions can be derived from this part of the present study.

- A shoulder region has been observed within the current transition JIB curves. The heat flux plateau increased with the increase in the degree of subcooling. The vapor breakup frequency measurements performed at different degrees of subcooling showed strong fluctuations. However, the average frequency increased with the degree of subcooling, which is consistent with the general trend reported in the literature.
- A mechanistic model has been developed to predict the wall heat flux within the transition boiling regime. The present model considered three heat transfer mechanisms: quenching, intrusion, and latent heat transfer. The present mechanistic model predicted the current experimental data with a maximum relative deviation within ± 20 % and the experimental data reported in the literature within ± 30 %. The model results showed that the assumption of ignoring the contribution of heat due to evaporation employed in previous studies is valid only at high degrees of subcooling (higher than 11 °C). However, heat due to evaporation must be considered at low degrees of subcooling (lower than 11°C).

The high-speed images taken during this part of the current study confirmed the existence of the Rayleigh-Taylor instability during the transition regime, as reported in the literature. Repetitive cycles of surface rewetting and dryness with high frequency were observed.

6.2. Future Work

The current research has contributed to the mechanistic modeling of JIB heat transfer within the nucleate and transition boiling regimes. The following are suggested directions to improve the quality of the current mechanistic model and further our understanding of the complex boiling phenomena within the nucleate and transition boiling regimes.

6.2.1. Nucleate Boiling Regime

- Carry out investigations of the bubble dynamics for higher degrees of subcooling and jet velocities.
- Develop submodels to predict the bubble release frequency and the active nucleation sites which are needed to develop mechanistic models of the total wall heat flux.
- In industrial applications, multiple jets are usually used. Studying the effect of the interaction of multiple jets on bubble dynamics is very important.
- Schlieren imaging could be used to investigate the thermal gradient around the growing bubbles at different degrees of superheat, degrees of subcooling, and jet velocities. This will help us to accurately describe the different forces acting on the growing bubbles and examine the possibility of the existence of other effects such as Marangoni convection at the interface of the growing bubbles.

6.2.2. Transition Boiling Regime

- The current study investigated the frequency of the vapor-liquid interface at different degrees of subcooling. Future work could be to extend the study to higher jet velocities.

- Investigate the cause of the first minimum that was observed in previous studies. The heating power intensity and response time of the heating system are believed to significantly affect the first minimum. Further research is needed in this direction.

- It is highly recommended to use high-speed X-ray imaging to measure the dynamics of the vapor layer thickness in the transition regime.

- Investigate the underlying physics of the heat transfer mechanism on a moving boiling surface. Since in industrial applications like metal thermal processing, the boiling surface is sometimes moving while cooled with the jet. Adding a moving boundary to the problem will increase its complexity, in addition to the technical challenges to design such a setup to carry out steady-state experiments.

7. References

[1] D.H. Wolf, F.P. Incropera, R. Viskanta, Jet impingement boiling, Advances in Heat Transfer 23 (1993): 1-132.

[2] L. Qiu, S. Dubey, F.H. Choo, F. Duan, Recent developments of jet impingement nucleate boiling, International Journal of Heat and Mass Transfer 89 (2015): 42-58.

[3] C. Agrawal, Surface Quenching by Jet Impingement− A Review Agrawal, C., 2019. Surface Quenching by Jet Impingement− A Review. Steel Research International 90 (2019): 1800285.

[4] Y. Miyasaka, S. Inada, Y. Owase, Critical heat flux and subcooled nucleate boiling in transient region between a two-dimensional water jet and a heated surface, Journal of Chemical Engineering of Japan 13 (1980): 22-28.

[5] K. Torikai, K. Suzuki, A. Suzuki, T. Watanabe, Micro-bubbles emission in subcooled transition boiling by use of multi-water-jet, Proceedings of 3rd international symposium on multiphase flow and heat transfer, Xi'an, China. 1994.

[6] H. Robidou, H. Auracher, P. Gardin, M. Lebouché, Controlled cooling of a hot plate with a water jet, Experimental Thermal and Fluid Science 26 (2002): 123-129.

[7] H. Robidou, H. Auracher, P. Gardin, M. Lebouche, L. Bogdanić, Local heat transfer from a hot plate to a water jet, Heat and Mass Transfer 39 (2003): 861-867.

[8] L. Bogdanic, H. Auracher, F. Ziegler, Two-phase structure above hot surfaces in jet impingement boiling, Heat and Mass transfer 45 (2009): 1019-1028.

[9] A.B. Ahmed, M.S. Hamed, Modeling of transition boiling under an impinging water jet, International Journal of Heat and Mass Transfer 91 (2015): 1273-1282.

[10] K. Suzuki, K. Torikai, H. Satoh, J. Ishimaru, Y. Tanaka, Boiling heat transfer of subcooled water in a horizontal rectangular channel: observation of MEB and MEB generation, Heat Transfer—Asian Research: Co-sponsored by the Society of Chemical Engineers of Japan and the Heat Transfer Division of ASME 30.5 (2001): 426-438.

[11] J. Ando, K. Horiuchi, T. Saiki, T. Kaneko, I. Ueno, Transition process leading to microbubble emission boiling on horizontal circular heated surface in subcooled pool, International Journal of Heat and Mass Transfer 101 (2016): 240-250.

[12] J. Tang, Z. Mo, L. Sun, C. Yan, An experimental study on Microbubble Emission Boiling in a subcooled pool: Heat transfer characteristics and visualized presentation, Experimental Thermal and Fluid Science 80 (2017): 40-52.

[13] K. Kawakami, S. Sakamoto, H. Tanigawa, T. Tsuruta, A study on transition process to MEB by limiting boiling space, Journal of Thermal Science and Technology 16 (2021)

[14] K. Suzuki, H. Saitoh, K. Matsumoto, High heat flux cooling by microbubble emission boiling, Annals of the New York Academy of Sciences 974 (2002): 364-377.

[15] K. Suzuki, R. Inagaki, A fundamental study on high heat flux cooling using subcooled flow boiling with microbubble emission, Proceedings of 5th International

Conference on Enhanced, Compact and Ultra-Compact Heat Exchangers: Science, Engineering and Technology, NJ, USA, 2005.

[16] J. Nakamura, T. Tsuruta, H. Tanigawa, A study on mechanism of microbubble emission boiling, Transactions of the JSME 84 (2018) 17-00405-.

[17] K. Suzuki, T. Kokubu, M. Nakano, H. Kawamura, I. Ueno, H. Shida, O. Ogawa, Enhancement of heat transfer in subcooled flow boiling with microbubble emission, Experimental Thermal and Fluid Science 29 (2005): 827-832.

.[18] K. Suzuki, T. Nomura, C. Hong, K. Yuki, Subcooled Flow Boiling With Microbubble Emission in a Microchannel, International Conference on Micro/Nanoscale Heat Transfer. Vol. 43901, 2009.

[19] L. Bogdanic, Two-phase structure Underneath a water jet impinging on a hot surface, Ph.D. thesis, Technical University of Berlin, , 2012.

[20] V. Rudnev, D. Loveless, R.L. Cook, Handbook of induction heating, CRC press, 2017.

[21] C.A. Hernández-Bocanegra, J.I. Minchaca-Mojica, F.A. Acosta-González, X. Zhou, B.G. Thomas, Measurement of heat flux in dense air-mist cooling: Part II–The influence of mist characteristics on steady-state heat transfer, Experimental Thermal and Fluid Science 44 (2013): 161-173.

[22] C.A. Hernández-Bocanegra, F.A. Acosta-González, X. Zhou, B.G. Thomas, Measurement of heat flux in dense air-mist cooling: Part I–A novel steady-state technique, Experimental Thermal and Fluid Science 44 (2013): 147-160.

[23] S. Hua, R. Huang, Z. Li, P. Zhou, Experimental study on the heat transfer characteristics of subcooled flow boiling with cast iron heating surface, Applied Thermal Engineering 77 (2015): 180-191.

[24] N. Kurul, M.Z. Podowski, Multidimensional effects in forced convection subcooled boiling, International Heat Transfer Conference Digital Library. Begel House Inc., 1990.

[25] S.C.P. Cheung, S. Vahaji, G.H. Yeoh, J.Y. Tu, Modeling subcooled flow boiling in vertical channels at low pressures – Part 1: Assessment of empirical correlations, International Journal of Heat and Mass Transfer 75 (2014): 736-753.

[26] R.L. Mohanty, M.K. Das, A critical review on bubble dynamics parameters influencing boiling heat transfer, Renewable and Sustainable Energy Reviews 78 (2017): 466-494.

[27] H.C. Ünal, Maximum bubble diameter, maximum bubble-growth time and bubble-growth rate during the subcooled nucleate flow boiling of water up to 17.7 MN/m2, International Journal of Heat and Mass Transfer 19 (1976): 643-649.

[28] V. Prodanovic, D. Fraser, M. Salcudean, Bubble behavior in subcooled flow boiling of water at low pressures and low flow rates, International Journal of Multiphase Flow 28 (2002): 1-19.

[29] N. Basu, G.R. Warrier, V.K. Dhir, Wall heat flux partitioning during subcooled flow boiling: Part 1—model development, ASME. Journal of Heat Transfer 127 (2005): 131-140.

[30] R. Sugrue, J. Buongiorno, T. McKrell, An experimental study of bubble departure diameter in subcooled flow boiling including the effects of orientation angle, subcooling, mass flux, heat flux, and pressure, Nuclear Engineering and Design 279 (2014): 182-188.

[31] C.S. Brooks, T. Hibiki, Wall nucleation modeling in subcooled boiling flow, International Journal of Heat and Mass Transfer 86 (2015): 183-196.

[32] J. Du, C. Zhao, H. Bo, Investigation of bubble departure diameter in horizontal and vertical subcooled flow boiling, International Journal of Heat and Mass Transfer 127 (2018): 796-805.

[33] T. Ren, Z. Zhu, M. Yan, J. Shi, C. Yan, Experimental study on bubble nucleation and departure for subcooled flow boiling in a narrow rectangular channel, International Journal of Heat and Mass Transfer 144 (2019): 118670.

[34] A.A. Levin, P. V Khan, Experimental observation of the maximum bubble diameter in non-stationary temperature field of subcooled boiling water flow, International Journal of Heat and Mass Transfer 124 (2018): 876-883.

[35] P. Zhou, R. Huang, S. Huang, Y. Zhang, X. Rao, Experimental investigation on bubble contact diameter and bubble departure diameter in horizontal subcooled flow boiling, International Journal of Heat and Mass Transfer 149 (2020): 119105.

[36] A.M.T. Omar, Experimental Study and Modeling of Nucleate Boiling During Free Planar Liquid Jet Impingement, Ph.D. thesis, McMaster University, 2010.

[37] A.B. Ahmed, Mechanistic Modeling of Jet Impingement Boiling, Ph.D. thesis, McMaster University, 2016.

[38] J.F. Klausner, R. Mei, D.M. Bernhard, L.Z. Zeng, Vapor bubble departure in forced convection boiling, International Journal of Heat and Mass Transfer 36 (1993): 651-662.

[39] B.B. Mikic, W.M. Rohsenow, P. Griffith, On bubble growth rates, International Journal of Heat and Mass Transfer 13 (1970): 657-666.

[40] B.J. Yun, A. Splawski, S. Lo, C.-H. Song, Prediction of a subcooled boiling flow with advanced two-phase flow models, Nuclear Engineering and Design 253 (2012): 351-359.

[41] R. Sugrue, J. Buongiorno, A modified force-balance model for prediction of bubble departure diameter in subcooled flow boiling, Nuclear Engineering and Design 305 (2016): 717-722.

[42] N. Zuber, The dynamics of vapor bubbles in nonuniform temperature fields, International Journal of Heat and Mass Transfer 2 (1961): 83-98.

[43] M.G. Cooper, A.J.P. Lloyd, The microlayer in nucleate pool boiling, International Journal of Heat and Mass Transfer 12 (1969): 895-913.

[44] M. Colombo, M. Fairweather, Prediction of bubble departure in forced convection boiling: A mechanistic model, International Journal of Heat and Mass Transfer 85 (2015): 135-146.

[45] S. Raj, M. Pathak, M.K. Khan, An analytical model for predicting growth rate and departure diameter of a bubble in subcooled flow boiling, International Journal of Heat and Mass Transfer 109 (2017): 470-481.

[46] H. Setoodeh, W. Ding, D. Lucas, U. Hampel, Prediction of bubble departure in forced convection boiling with a mechanistic model that considers dynamic contact angle and base expansion, Energies 12 (2019): 1950.

[47] M.S. Plesset, S.A. Zwick, The growth of vapor bubbles in superheated liquids, Journal of Applied Physics 25 (1954): 493-500.

[48] A.M.T. Omar, M.S. Hamed, Modeling of bubble growth under an impinging free planar water jet, Heat Transfer Engineering 38.1 (2017): 63-74.

[49] S.J.D. Van Stralen, M.S. Sohal, R. Cole, W.M. Sluyter, Bubble growth rates in pure and binary systems: combined effect of relaxation and evaporation microlayers, International Journal of Heat and Mass Transfer 18 (1975): 453-467.

[50] N. Seiler-Marie, J.-M. Seiler, O. Simonin, Transition boiling at jet impingement, International journal of heat and mass transfer 47 (2004): 5059-5070.

[51] H. Robidou, Experimental study of two-phase cooling at high temperature by impinging water jet, Ph.D. thesis, University of Henri Poincare´, 2000.

[52] L. Bogdanic, H. Auracher, F. Ziegler, Investigation of the two-phase structure in subcooled jet impingement boiling with a miniaturized optical probe, 8th International Conference on Boiling and Condensation Heat Transfer, Switzerland, 2012.

[53] P.R. Jones, C.A. Chuang, T. Sun, T.Y. Zhao, K. Fezzaa, J.C. Takase, D. Singh, N.A. Patankar, High-speed X-ray imaging of the Leidenfrost collapse, Scientific Reports 9 (2019): 1-12.

[54] C.F. Gomez, C.W.M. van der Geld, J.G.M. Kuerten, R. Liew, M. Bsibsi, B.P.M. van Esch, The nature of boiling during rewetting of surfaces at temperatures exceeding the thermodynamic limit for water superheat, Journal of Fluid Mechanics 895 (2020).

[55] K.A. Estes, I. Mudawar, Comparison of two-phase electronic cooling using free jets and sprays, ASME. Journal of Electronic Packaging 117 (1995): 323–332.

[56] M. Monde, Y. Katto, Burnout in a high heat-flux boiling system with an impinging jet, International Journal of Heat and Mass Transfer 21 (1978): 295-305.

[57] T.Y. Lee, T.W. Simon, A. Bar-Cohen, An Investigation of Short Heating Length Effects on Flow Boiling Critical Heat Flux in a Subcooled Turbulent Flow, Cooling Technology for Electronic Equipment (1988): 435-450.

[58] B.A. Kader, Temperature and concentration profiles in fully turbulent boundary layers, International Journal of Heat and Mass Transfer 24 (1981): 1541-1544.

[59] R. Situ, T. Hibiki, M. Ishii, M. Mori, Bubble lift-off size in forced convective subcooled boiling flow, International Journal of Heat and Mass Transfer 48 (2005) 5536–5548.

[60] A.B. Ahmed, M.S. Hamed, Bubble Dynamics Under an Impinging Planar Water Jet, International Conference on Heat Transfer, Fluid Mechanics and Thermodynamics, Spain, 2016.

[61] N. Zuber, Hydrodynamic aspects of boiling heat transfer, Ph.D. thesis, University of California, 1959.

[62] G.I. Taylor, The instability of liquid surfaces when accelerated in a direction perpendicular to their planes, Proceedings of the Royal Society of London. Series A. Mathematical and Physical Sciences 201 (1950): 192-196.

[63] D.J. Lewis, The instability of liquid surfaces when accelerated in a direction perpendicular to their planes. II, Proceedings of the Royal Society of London. Series A. Mathematical and Physical Sciences 202 (1950): 81-96.

[64] D.-Y. Hsieh, Effects of heat and mass transfer on Rayleigh-Taylor instability, ASME. Journal of Basic Engineering, 94 (1972): 156-160.

[65] P.J. Berenson, Film-boiling heat transfer from a horizontal surface, ASME. Journal of Heat Transfer 83 (1961): 351–356.

Appendix A: Experimental Data of Bubble Dynamics

Table A.1: Experimental data of the bubble dynamics study.

Test #	Set #	V_{jet} m/s	ΔT_{sub} $°C$	ΔT_{sup} $°C$	q_w'' KW/m^2	BDD (mm)	± σ (mm)
1	1	0.2	16.5	14.8	708.57	0.366	0.134
2			16.2	16.3	844.22	0.384	0.146
3			15.9	17.4	1056.57	0.446	0.194
4			15.1	18.5	1507.13	0.506	0.208
5	2		23.3	18.2	958.94	0.316	0.116
6			25.7	19.2	1259.12	0.367	0.136
7			23.7	21.1	1819.37	0.435	0.16
8	3		37.6	29.5	1866.47	0.448	0.147
9			37.6	30.5	2339.24	0.524	0.168
10			37.6	31.2	2749.30	0.501	0.159
11			37.0	33.7	3448.49	0.510	0.135
12	4	0.4	13.4	12.6	621.18	0.429	0.122
13			13.7	13.9	770.68	0.446	0.156
14			13.7	15.0	926.52	0.527	0.207
15			13.9	15.3	1258.19	0.580	0.211
16	5		16.5	15.4	682.70	0.344	0.119
17			16.7	16.4	848.18	0.447	0.191
18			16.0	17.3	1064.27	0.480	0.19
19			16.0	17.8	1302.58	0.511	0.167
20	6		21.7	18.5	1013.80	0.318	0.123
21			21.2	19.8	1238.04	0.382	0.125
22			20.8	20.8	1532.23	0.420	0.135
23			22.0	21.6	1868.31	0.466	0.133
24	7		36.5	26.4	1773.28	0.384	0.121
25			36.5	27.8	2071.43	0.401	0.119
26			36.6	28.9	2470.71	0.389	0.099
27			36.6	29.5	2887.12	0.471	0.133
28	8	0.6	15.8	14.5	740.79	0.425	0.163
29			15.3	15.9	885.40	0.501	0.17
30			15.7	17.0	1066.67	0.513	0.178

Test #	Set #	V_{jet} m/s	ΔT_{sub} $°C$	ΔT_{sup} $°C$	q_w'' KW/m^2	BDD (mm)	± σ (mm)
31			15.5	17.7	1289.38	0.522	0.198
32	9		22.8	18.2	1031.98	0.342	0.155
33			22.3	20.1	1253.78	0.461	0.165
34			22.9	21.1	1514.34	0.551	0.183
35			24.0	21.7	1848.31	0.476	0.146
36	10		36.7	25.6	1836.74	0.282	0.079
37			36.7	27.3	2149.65	0.362	0.102
38			36.7	28.5	2449.05	0.368	0.093
39			36.8	29.2	2876.58	0.403	0.098
40	11	0.8	11.7	13.5	734.74	0.341	0.134
41			12.3	14.9	865.19	0.399	0.16
42			13.2	15.4	1158.44	0.453	0.181
43			13.3	15.9	1386.06	0.451	0.166
44			13.2	16.5	1626.48	0.425	0.168
45	12		16.3	16.4	836.21	0.307	0.111
46			16.3	17.2	1085.21	0.341	0.126
47			16.3	18.0	1305.92	0.394	0.157
48			16.2	18.7	1537.97	0.431	0.149
49	13		22.5	20.3	1262.15	0.297	0.103
50			22.9	21.1	1542.54	0.371	0.143
51			23.1	22.0	1835.67	0.447	0.129
52	14		36.3	24.9	1938.50	0.251	0.083
53			36.4	26.3	2247.76	0.261	0.103
54			36.1	27.4	2630.18	0.280	0.099
55			36.4	28.5	3023.84	0.411	0.13

Appendix B: Uncertainty Analysis

B.1. Heat Flux and Surface Temperature

The wall heat flux is calculated from the following equation

$$q_s''= k_{cu}\left.\frac{\partial T}{\partial y}\right|_{y=0} \qquad \text{(B.1)}$$

The temperature gradient at the boiling surface is calculated from the first derivative of the temperature profile equation (B.2) inside the copper block.

$$T(y) = c_0 y^2 + c_1 y + c_2 \qquad \text{(B.2)}$$

To calculate the surface temperature T_0, we need to get the solution of coefficients c_0, c_1, and c_2 as a function of the known parameters $(T_1, T_3, T_5, y_1, y_3, y_5)$ where $T_1, T_3, and\, T_5$ are temperature readings at locations $y_1, y_3, and\, y_5$ which are coordinates 1 mm,3 mm, and 5 mm, respectively below the boiling surface. The following equations are solved to get T_0.

$$\begin{cases} T(y_1) = c_0 y_1^2 + c_1 y_1 + c_2 = T_1 \\ T(y_3) = c_0 y_3^2 + c_1 y_3 + c_2 = T_3 \\ T(y_5) = c_0 y_5^2 + c_1 y_5 + c_2 = T_5 \\ T(y_0) = c_0 y_0^2 + c_1 y_0 + c_2 = T_0 \end{cases}$$

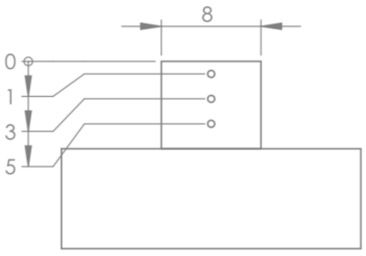

It is noticed that the Symbolic solution of equation (B.2) for c_0 and T_0

solution of $c_1 = f(T_1, T_3, T_5, y_1, y_3, y_5)$

solution of $T_0 = g(T_1, T_3, T_5, y_1, y_3, y_5)$

The uncertainty in the wall heat flux u_{qs} depends on two variables k_{cu} and $\left.\frac{\partial T}{\partial y}\right|_{y=0}$ as expressed in equation (B.3).

$$\frac{u_{qs}}{q_s^{"}} = \left[\left(\frac{u_k}{k_{cu}}\right)^2 + \left(\frac{u_{c1}}{c1}\right)^2\right]^{1/2} \tag{B.3}$$

The uncertainty in k_{cu} is assumed 3 %. The uncertainty of $\left.\frac{\partial T}{\partial y}\right|_{y=0}$ is the same as the uncertainty of coefficient c_1 which is calculated from equation (B.4).

$$u_{c1} = \left[\left(\frac{\partial f}{\partial T1} u_{T1}\right)^2 + \left(\frac{\partial f}{\partial T3} u_{T3}\right)^2 + \left(\frac{\partial f}{\partial T5} u_{T5}\right)^2 + \left(\frac{\partial f}{\partial y1} u_{y1}\right)^2 + \left(\frac{\partial f}{\partial y3} u_{y3}\right)^2 + \left(\frac{\partial f}{\partial y5} u_{y5}\right)^2\right]^{1/2} \tag{B.4}$$

The uncertainty in the surface temperature u_{T0} is calculated by equation (B.5)

$$u_{T0} = \left[\left(\frac{\partial g}{\partial T1} u_{T1}\right)^2 + \left(\frac{\partial g}{\partial T3} u_{T3}\right)^2 + \left(\frac{\partial g}{\partial T5} u_{T5}\right)^2 + \left(\frac{\partial g}{\partial y1} u_{y1}\right)^2 + \left(\frac{\partial g}{\partial y3} u_{y3}\right)^2 + \left(\frac{\partial g}{\partial y5} u_{y5}\right)^2\right]^{1/2} \tag{B.5}$$

Where $u_{y1} = u_{y3} = u_{y5}$ is the uncertainty in thermocouple locations which is 0.005 mm and $y_1 = 1\ mm, y_3 = 3\ mm, y_5 = 5\ mm$.

The uncertainties in interior temperatures $u_{T1}, u_{T3}, and\ u_{T5}$ are calculated as follows:

$$u = \sqrt{u_A^2 + u_B^2} \tag{B.6}$$

Where u_B : manufactured uncertainty, $u_B = \pm 0.25\ ℃$

u_A : measurement uncertainty (sampling), $u_A = \frac{\sigma}{\sqrt{N}} = \frac{standard\ deviation}{\sqrt{Sample}}$

Uncertainty calculation in Nucleate regime

	TC1 ℃	TC3 ℃	TC5 ℃
Measurement Avg.	117.76	124.38	131
σ (STD)	0.19	0.18	0.22
N (samples)	326	326	326
Max	118.08	124.69	131.55
Min	117.1	123.7	130.37
u_A	0.011	0.010	0.012
u_B	0.25	0.25	0.25
Uncertianty	0.250	0.250	0.250

The surface temperature in the nucleate regime is $T_0 = 114.5\ ℃ \pm 0.57\ ℃$ (0.5 %).

The corresponding heat flux is q''_s =1237.8 KW/m^2 ±181.8 KW/m^2 (14.7 %).

Uncertainty calculation in the Transition regime

	TC1 °C	TC3 °C	TC5 °C
Measurement Avg.	629.16	665.15	701.78
σ (STD)	0.36	0.24	0.24
N (samples)	358	358	358
Max	632.45	668.57	705.4
Min	630.68	667.12	704
u_A	0.019	0.013	0.013
u_B	0.25	0.25	0.25
u_T	0.251	0.250	0.250

The surface temperature in the nucleate regime is $\mathrm{T_0} = 611.42\ ℃\ \pm 0.61\ ℃\ (0.1\ \%)$.
The corresponding heat flux is $\mathrm{q_s^{"}}$ = 6716.493 KW/m2 ± 276.3 KW/m2 (4.1 %).

B.2. Bubble diameter

Images were captured with a resolution of 35 pixels/mm, the error of two neighbored pixels is 0.057 mm. In addition to sampling uncertainty 0.067 mm. Then, the total uncertainty in bubble diameter is

$$u_d = \sqrt{0.057^2 + 0.067^2} = 0.088\ mm$$